# Geodetic Methods of Mapping Earthquake-Induced Ground Deformation and Building Damage

by

Anna K. Diederichs
B.Sc., University of Victoria, 2018

A Thesis Submitted in Partial Fulfillment of the
Requirements for the Degree of

MASTER OF SCIENCE

in the School of Earth and Ocean Sciences

Geodetic Methods of Mapping Earthquake-Induced Ground Deformation and Building Damage

by

Anna K. Diederichs
B.Sc., University of Victoria, 2018

Supervisory Committee

Dr. Edwin Nissen, Supervisor
(School of Earth and Ocean Sciences)

Dr. Lucinda Leonard, Departmental Member
(School of Earth and Ocean Sciences)

Dr. Tuna Onur, Outside Member
(Department of Civil Engineering)

## ABSTRACT

I use temporal lidar and radar to reveal fault rupture kinematics and to test a method of mapping earthquake-induced structural damage. Using pre- and post-event data, these applications of remote technology offer unique perspectives of earthquake effects. Lidar point clouds can produce high resolution, three dimensional terrain maps, so subtle landscape shifts can be discerned through temporal analysis, providing detailed imagery of co-seismic ground displacement and faulting. All weather radar systems record back-scattered signal amplitude and phase. Pre- and post-event comparisons of phase can illuminate co-seismic structural damage using an oblique look angle, most sensitive to changes in building heights. Extracted information from these geodetic methods may be used to inform decisions on future earthquake modeling and emergency response.

In the first major section of this thesis, I calculate co-seismic 3D ground deformation produced by the Papatea fault using differential lidar. I demonstrate that this fault - a key element within the 2016 $M_w$ 7.8 Kaikōura earthquake - has a distinctly non-planar geometry, far exceeded typical co-seismic slip-to-length ratios, and defied Andersonian mechanics by slipping vertically at steep angles. Its surface deformation is poorly reproduced by elastic dislocation models, suggesting the Papatea fault did not release stored strain energy as typically assumed, perhaps explaining its seismic quiescence in back-projections. Instead, it slipped in response to neighboring fault movements, creating a localized space problem, accounting for its anelastic deformation field. Thus, modeling complex, multiple-fault earthquakes as slip on planar faults embedded in an elastic medium may not always be appropriate.

For the second major part of this thesis, I compare mean values of interferometric synthetic aperture radar (InSAR) coherence change across four case studies of earthquake-induced building damage. These include the 2016 Amatrice earthquake, the 2017 Puebla–Morelos earthquake, the 2017 Sarpol-e-Zahab earthquake, and the 2018 Anchorage earthquake. I examine the influences of environmental and urban characteristics on co-seismic coherence change using Sentinel-1 imagery and compare the outcomes of various damage levels. I do not find consistent values of mean coherence change to distinguish levels of damage across the case studies, indicating coherence change values vary with location, environment, and damage pattern. However, this method of damage mapping shows potential as a useful tool in earthquake emergency response, capable of quickly identifying localized areas of high damage in areas with low snow and vegetation cover. Given the large spatial coverage and relatively quick, low cost acquisition of SAR imagery, this method could provide damage estimates for unsafe or remote regions or for areas unable to self-report damage.

# Contents

# List of Tables

# List of Figures

# ACKNOWLEDGEMENTS

I would like to thank my supervisor, Edwin Nissen, for providing guidance and encouragement throughout my research and for securing and providing funding from the National Science and Engineering Research Council of Canada, the Canada Foundation for Innovation, the BC Knowledge Development Fund, and a Canada Research Chair. I also thank the KEGS Foundation (Canadian Exploration Geophysical Society) and the University of Victoria for partially funding this research.

I would also like to thank my committee members, Lucinda Leonard and Tuna Onur, for their advice and support. Thank you to Andrea Donnellan for her time and effort as my external examiner.

I thank the editors of Science Advances and the two anonymous reviewers for their suggestions and comments on the Papatea fault study. I thank William Ries for helping organize and navigate the large volume of lidar data and for comments on an early draft of the manuscript.

I would like to thank Robert Langridge, Ian Hamling, and Kate Clark of GNSS (NZ) for helpful discussions about the Kaikōura rupture and the role of the Papatea fault. I also would like to thank Lia Lajoie for sharing her profiling script with me and for her help with the script. Thank you to Sri Malireddi and Andrea Tagliasacchi for their contributions to the ICP code used for differential lidar of the Clarence Valley, NZ. I thank Land Information New Zealand, New Zealand Transport Agency, Environment Canterbury, Marlborough District Council, and AAM NZ Ltd. for funding, collecting, and distributing the lidar data used. I also thank the European Space Agency for their freely available Sentinel-1 and -2 data used in the coherence study.

Thank you to the members of the TEARS research group and the Pacific Geoscience Center (PGC), Geological Survey of Canada for their support, encouragement, and constructive comments and suggestions throughout my research. A special thank you to Élyse Gaudreau for sharing her GAMMA scripts with me.

Finally, I would like to thank my friends and family for their endless love and encouragement.

# Chapter 1

# Thesis Overview

Remote sensing is the science of acquiring information through observation of an object using an instrument at some distance away [2]. For geophysical applications, remote sensing is the observation of physical targets on Earth's surface using electromagnetic radiation. The remote sensing process begins with a sensor, usually space-borne (on board a satellite) or airborne (on board an airplane, helicopter, or unpiloted aerial vehicle). Physical targets are imaged by the sensor from recorded back-scattered electromagnetic radiation [3, 4]. This can occur either passively, where the sensor relies on sunlight for target illumination, or actively, where the sensor transmits and receives its own source of energy for illumination. The recorded data are processed and analyzed to interpret characteristics of imaged objects. Geodesy is the science of understanding and measuring the Earth's shape and orientation, often done using remote sensing and Global Navigation Satellite System (GNSS) data. Geodetic data may be combined with other geospatial data to address specific geophysical problems [3, 4].

Synthetic Aperture Radar (SAR) and lidar (light detection and ranging) are two active remote sensing methods used, among a wide variety of other applications, to map changes on Earth's surface caused by an earthquake. Chapter 2 provides an overview of SAR and lidar, including data acquisition, image formation, and processing. In Chapter 3, I introduce differential lidar and map 3D displacements along the Papatea Fault - one of over 20 surface ruptures from the 2016 $M_w$ 7.8 Kaikōura earthquake (New Zealand). I compare the observed displacement field to forward elastic models and reveal several unusual characteristics of this fault, which may have played a key role in the propagation of this complex earthquake. In Chapter 4, I use temporal InSAR coherence to map co-seismic building damage following four different earthquakes. I discuss the dominant influences on interferometric coherence using SAR imagery and surveyed damage data from Amatrice (Italy), Mexico City (Mexico),

Kermanshah (Iran), and Anchorage (Alaska) caused by damaging earthquakes in a variety of environmental settings. These case studies were chosen based on data availability as well as the variability of environmental, urban, and damage characteristics across the four areas. I compare the values of mean coherence change at different structural damage levels and consider where this method of damage mapping would be most useful as a tool for future emergency response following a destructive earthquake.

# Chapter 2

# Lidar and SAR Remote Sensing

## 2.1 Lidar

Lidar technology has been evolving for over 50 years, with some of the first applications used for measuring properties of the upper atmosphere (eg. [5, 6]). Geospatial applications of lidar progressed to focus on extracting altimetry information for digital elevation mapping [7]. Although lidar applications now range from virtual reality games to navigation of autonomous cars, lidar remote sensing is a valuable tool for accurate biological and geophysical measurements from high resolution 3D terrain mapping.

Lidar is an active form of remote sensing that uses rapidly transmitted narrow laser pulses, arranged in a specified spatial orientation with a given pulse frequency [7]. Lidar systems operate in the ultraviolet to near-infrared portion of the electromagnetic spectrum and, for terrestrial mapping, are usually airborne and nadir-looking (see Figure 2.1) [8, 9]. However, the NASA Ice, Cloud, and Land Elevations (ICESat, 2003 - 2010) and ICESat-2 (2018 - current) satellites are the only space-borne laser altimeters [10, 7]. For topographic mapping, discrete-return lidar systems are employed, where peak return signals are recorded. This differs from waveform lidar systems that record the full waveform of the return signals and is useful for detailed mapping of vertical structures, canopy characterization, and biomass studies [10].

The return signals of discrete lidar systems are recorded by the sensor to determine the elevation of the imaged target. Elevation is resolved from the distance from sensor to target, calculated from the time difference between the transmitted and return signals, given that the laser travels at the speed of light. Using the distance information with the lidar system's GPS and IMU (inertial navigation measurement unit of the aircraft's orientation), the x, y,

and z (elevation) positions of point returns are determined, resulting in a 3D point cloud of the landscape [10]. These point clouds can be classified based on position and discrete return intensity and can be resampled to produce high resolution elevation rasters [10].

The spatial resolution of the point cloud depends on the sampling density, flight speed and height, scanning pattern, pulse rate and duration, and foot print area [7, 11]. The area imaged is dependent on the footprint diameter which is directly influenced by the scanning angle of the transmitted beam (see Figure 2.1) [11]. Typically, pulse frequencies range from 10 - 150 kHz and the higher the pulse rate, the greater the sampling density. The point density also depends on the footprint spacing, which is the distance between lines of pulses in the scanning pattern. The scanning pattern is the spatial orientation of the transmitted pulses. A seesaw pattern, as shown in Figure 2.1, is most common [11]. Further, the duration of the pulse influences the intensity of the transmitted and received signals. Optimization of these parameters yields a dense, detailed point cloud.

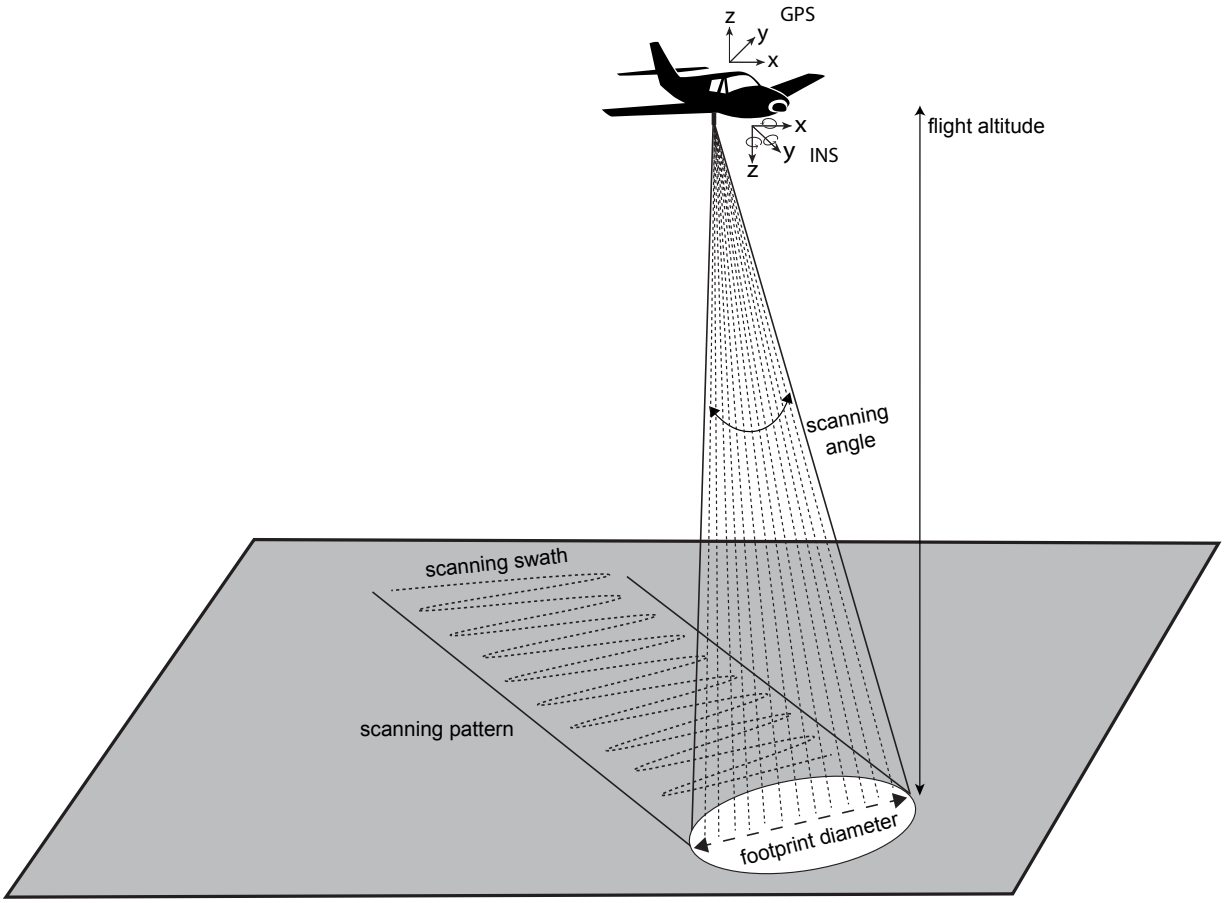


Figure 2.1: Schematic diagram of imaging using airborne lidar.

## 2.2 Differential Lidar

Differential lidar compares post-event to pre-event data to map, analyze and quantify ground changes from natural disasters with centimeter accuracy [12, 13]. Some applications of this technique include landslide detection and monitoring, fault identification and co-seismic ground displacement (eg. refs. [14, 15, 13, 16]). Differential lidar can also be used to understand near-fault co-seismic ground deformation, unlike SAR interferometry, that fails to map areas of rapid ground displacement due to the high amount of surface disruption [13]. Two methods of differencing lidar are differenced digital elevation models [14, 17] derived from laser scans, which is most sensitive to vertical displacements, or by iteratively differencing raw lidar point clouds, which allows for the extraction of 3D displacement fields [18, 13].

### 2.2.1 DEM of difference

Digital elevation models (DEMS) are representations of topography using raster grids or triangulated irregular networks (TINs) interpolated from lidar point clouds [15]. A DEM of difference (DoD) can be calculated from a simple difference to reveal vertical topographic changes. This method has been used in many fields of earth science, including biomass, mass wasting, and tectonic studies to map temporal elevation changes. However, this method cannot resolve horizontal displacements, indicating that, in tectonic studies, calculated temporal vertical differences may not represent true vertical co-seismic shifts because topography and lateral offsets influence temporal elevation changes [14, 17]. Thus, DEMs may be masked to isolate only very flat regions so that the elevation difference closely approximates co-seismic vertical displacements [17]. Additionally, optical or digital image correlation methods, used to calculate pixel offsets to resolve horizontal motion, may be paired with DoD studies to calculate displacements in three directions (eg. refs. [19, 20, 21]). Creating a DoD may be favorable when studying large study areas because this requires minimal computation time, unlike iterative alignment methods, that are more effective for smaller data sets. Additionally, a DoD can be produced using a wide range of GIS softwares, making it an accessible option.

### 2.2.2 Iterative Closest Point

Another method of studying temporal lidar surveys is by implementing an iterative closest point (ICP) algorithm, where pre- and post-event point clouds are iteratively aligned to

calculate x, y, and z differences between clouds. This method can work on irregular point clouds because the algorithm works to iteratively find the nearest points [22, 23], meaning point cloud densities do not need to match. However, this method relies on the assumption that the two point clouds are of approximately the same area (coarse alignment). Additionally, the point clouds must share a common reference frame [22, 23]. In each iteration, the algorithm searches locally to find the optimal pairwise alignment and calculates the rigid body transformation. This means that the translations and rotations about Cartesian axes are calculated and the mean square error is minimized between aligned data points [22, 18]. This process is iterated until local closest point distances are minimized, determined when the error is smaller than a defined threshold [22, 18]. By summing the total transformations, the 3D difference between point data sets is captured, which can then be separated into x, y, and z displacement fields. Nonetheless, this method has some limitations in very smooth areas and regions with dense vegetation. For example, very smooth, flat surfaces are difficult to align because point returns from a flat surface appear very similar. Thus, there may be several optimal pairwise alignments between very flat surfaces. Therefore, the ICP algorithm works best on flat surfaces that are somewhat textured. Additionally, point returns from vegetation may hinder the alignment process where vegetation growth and weather influences may cause these areas to appear too different to align between data sets. Therefore, for most successful outcomes, points classified as vegetation should be removed, leaving a bare earth surface to perform the alignment on.

Similar methods of three dimensional differencing have been used by the medical community to align patient body scans (eg. [24]) and in computer graphics to align object geometries (eg. [22, 25]). For earth sciences, point cloud alignment has provided detailed 3D information about landsliding [16, 26], tectonic motion, and earthquake-induced structural damage [27, 28, 29]. However, this method relies on the availability of pre-event surveys. For tectonic studies, these pre-event data sets rarely include entire rupture extents. Full pre-event lidar coverage was available for the 2010 El-Mayor Cucapah earthquake in Baja California, Mexico, where the ICP algorithm was implemented [30]. Other studies have used this method to study rupture segments within large earthquakes, including the 2008 Iwate–Miyagi, 2011 Fukushima–Hamadori, and 2016 Kumamoto earthquakes [13, 19, 31]. However, open-source portals, like Open Topography, publish global lidar data, increasing the potential availability of pre-event data.

## 2.3 Synthetic Aperture Radar

### 2.3.1 Imaging

Since the launch of NASA's SeaSat mission in 1978, SAR systems have been used to actively image and observe Earth's surface [32]. SAR systems use back-scattered microwave energy to map physical features on the ground [33]. These systems provide their own source of microwave illumination, allowing them to image during day or night [34, 33]. Further, the use of long wavelength radiation results in minimal atmospheric scattering, allowing the microwave signal to penetrate through nearly all weather conditions [34, 33]. For earth observation, the most common frequency bands employed by SAR systems are X- (2.4–3.8 cm), C- (3.8–7.5 cm), or L-band (15–30 cm) [4, 35]. SAR systems are capable of observing and recording a wide range of geophysical data used for debris flow mapping, ground deformation assessment, fire scar delineation, and building damage mapping (eg. refs. [36, 37, 38]).

SAR systems are most commonly airborne or space-borne and are made up of four main components: 1) the signal transmitter, 2) the signal receiver, 3) the antenna, and 4) the electronic processing system [4, 33]. The transmitter emits short bursts of microwave energy to the ground, focused into a beam by the antenna. Energy is transmitted at the speed of light in the along-track (direction of the flight path) and across-track (direction perpendicular to the flight path) directions, simultaneously [33]. The energy is transmitted at a specific frequency band and pulse duration. The receiver detects back-scattered microwave energy from objects on the ground. Finally, the processing system forms the radar image from the return signals [33, 34].

The spatial resolution of a radar image is composed of the range (cross-track) and the azimuth (along-track) resolutions (see Figure 2.2). The former is dependent on the pulse length (the distance from sensor to ground and back), where the longer the length, the lower the spatial resolution [4]. From the time delay between the transmitted pulse and received back-scatter signal from a target on Earth's surface, the distance from the radar to the target can be computed [36, 39]. SAR systems operate at an off-nadir viewing geometry (side-looking) which optimizes ground coverage and mapping capabilities over nadir-looking systems [33, 36]. This side-looking angle allows the radar system to resolve pixel location information in the range direction from return signal times. For example, two points on the ground acquired from a nadir-looking system would be indistinguishable because the signal would reach each point at the same time, making their signal return times identical.

The azimuth resolution depends on the antenna beam width, whose length is electroni-

cally synthesized by the flying SAR system. SAR systems use aperture synthesis to create the effect of a longer antenna in space, which directs the transmitted pulses towards the ground [39, 34]. The longer the antenna, the narrower the beam width, resulting in a finer azimuth resolution. A long antenna length is synthesized by combining back-scatter echoes from multiple pulses from different geometries while the satellite flies [33, 36, 39]. This technique is used because it increases the image resolution without launching a large antenna into space, which is not very practical or feasible. To orient ground targets in the azimuth direction, the Doppler information of multiple echos are used. As the radar flies, there is an apparent shift in frequency of the recorded return signals of a given ground target. When flying toward a target, the frequency shift is positive (blue shifted) because the radar-to-target distance is decreasing. When the sensor is flying away from a given target, the Doppler shift of the return signals is negative (red shifted) [40]. This frequency information is then sorted by the radar to determine the location of the ground target within the radar image, along with the time delay of the return signal. [33, 36, 39].

### 2.3.2 Sentinel-1 Mission

The European Space Agency (ESA) launched the Sentinel-1A satellite in 2014, followed by the launch of Sentinel-1B in 2016. Individually, these two right-looking satellites have a 12 day revisit time, are equipped with a C-band (5.4 GHz, 5.6 cm wavelength) SAR sensors, and a 12.3 m $\times$ 0.821 m (length $\times$ width) antenna. Combined, Sentinel-1A and -1B have a global revisit time of 6 days since the satellites have nearly identical sensor characteristics and fly along the same orbital plane [41]. The Sentinel-1 satellites have four main image acquisition modes and two single-pass orientations. The acquisition modes include Stripmap, Interferometric Wide swath (IW), Extra-Wide swath (EW), and Wave mode. Stripmap mode is mainly used for applications where fine detail is required. IW mode is most commonly used interferometry, while the EW and Wave modes are often used for ocean and coastal monitoring [42, 41]. IW mode has a swath width of 250 km and uses a technique called TOPSAR (Terrain Observation with Progressive Scans SAR), where each acquisition is collected by scanning across three sub-swaths, made up of several bursts [42]. In IW mode, incidence angles (see Figure 2.2) range from $\sim 30^\circ$ - $46^\circ$ depending on the sub-swath and produce radar images with a spatial resolution of 5 m $\times$ 20 m (range $\times$ azimuth). The two single-pass orientations are either descending (flying south) or ascending (flying north) [41].

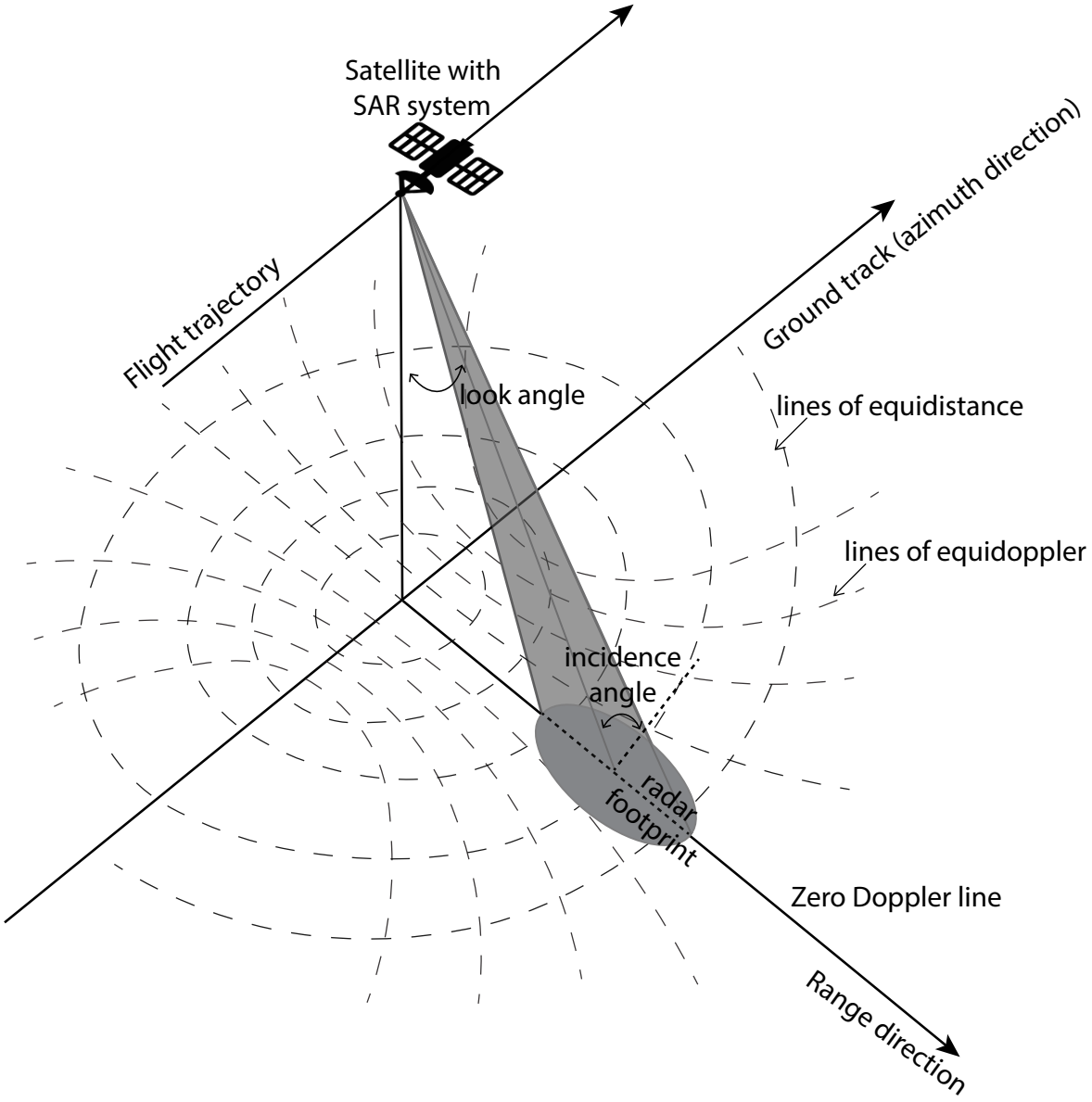


Figure 2.2: SAR imaging geometry adapted from [39]. The distance and Doppler information recorded by the radar are used to orient ground targets correctly within radar images in the range and azimuth directions. The incidence and look angles define the angle of the transmitted microwave energy.

### 2.3.3 Phase and Amplitude

Recorded back-scattered energy contains both amplitude and phase information. The radar phase (in radians) is the number of oscillations of the signal between the sensor, ground, and back again [39]. The wavelength of the microwave energy used in SAR imaging is shorter than the spatial resolution of the radar images. This means that the signal of a single pixel within the radar image (a resolution cell) is the sum of the return signals of many individual objects within that pixel. Therefore, the phase signal of each pixel is random, rendering the phase of a single SAR image useless [39]. The phase difference between two SAR acquisitions has utility and is often used for change detection studies. The amplitude (in decibels) of the recorded back-scatter signal represents the return signal strength. This value determines the brightness of pixels within a radar image and is the amount of energy that is reflected off of a target back to the receiver per unit area [39]. Both phase and amplitude of the return signal are influenced by ground target and radar system parameters [39, 43].

The recorded return signal is dominated by the moisture content and structure of a ground target. Moisture content directly influences the ground object's dielectric constant; a parameter that depends on an object's conductivity and ability to store electrical energy. The dielectric constant also influences the object's ability to absorb microwave energy which impacts the amount of energy back-scattered to the sensor [4]. Overall, object reflectivity increases with moisture content, while wave penetration decreases [4, 44]. Additionally, the various ways energy can be reflected (scattering mechanism) off a ground target affects the strength and consistency of the back-scattered signal [39]. The scattering mechanism depends on the object's surface roughness, structure, and interaction with microwave energy. The four main mechanisms of scattering are specular reflection off of a smooth surface, double bounce reflection from surfaces at right angles to each other, diffuse scattering from a rough surface, and volumetric scattering, often from vegetation, as summarized in Figure 2.3 [4, 45].

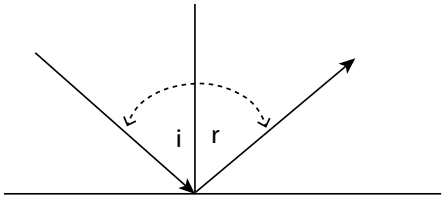


**Specular reflector:** the incidence angle, i, is equal to the angle of reflection, r.

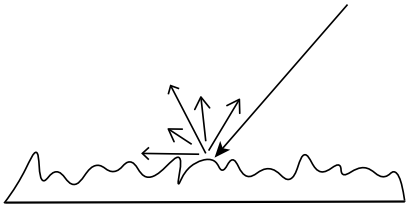

**Diffuse reflector:** scattering in many directions off of a rough surface.

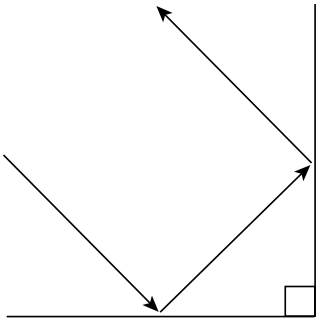

**Double bounce (corner reflector):** reflection off of two smooth surfaces at ~90º to each other.

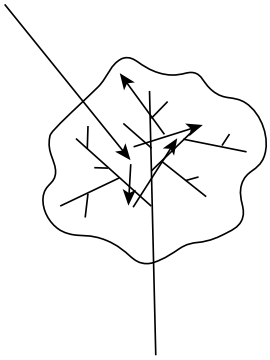

**Volumetric scattering:** scattering in many directions due to inhomogeneity in the structure of a ground target, like vegetation.

Figure 2.3: Four main mechanisms of scattering microwave energy depending on wavelength, surface roughness, and structure. Adapted from [4].

Several radar system parameters also play a significant role in the characteristics of the return signal. The wavelength of microwave energy used by the radar system influences the energy interaction with ground objects and the appearance of objects in radar images. Longer wavelengths penetrate materials like dry soil, snow, and forest canopy deeper than shorter wavelengths [4, 46]. For instance, L-band SAR signals penetrate vegetation deeper than shorter wavelength C- or X-band signals. Therefore, the longer wavelength system is capable of imaging underlying targets, like wetlands below vegetation. Thus, different wavelengths are used for different imaging applications. The appearance of surface roughness in SAR images also depends on wavelength, where objects appear smoother when imaging with a longer wavelength. Therefore, the same terrain may appear different depending on the frequency band of the radar [4].

Additionally, the polarization of the SAR sensor is an important system parameter to consider. Unpolarized electromagnetic energy vibrates in all directions perpendicular to the direction of propagation. Radar systems often filter the signal to isolate one vibrational direction, perpendicular to the direction of travel. This filtering is referred to as wave polarization and is independent on wavelength [4]. Radar systems transmit and receive polarized energy in a combination of horizontal and vertical orientations. For example, one polarization of Sentinel-1 data is cross-polarized with a VH orientation, meaning the transmitted energy is vertically polarized (V-), while the received signal is horizontally polarized (-H). Signal polarization is implemented by applying a filter to the antenna and is useful because different polarizations are sensitive to different physical properties and structures of ground targets [4, 47]. For example, vertically polarized energy is more sensitive to vertically oriented structures. The amount of reflected energy in different polarizations depends on how the energy interacts with the structure of the ground target, which allows different land cover types to be further distinguished [4].

The incidence angle of the SAR sensor also directly influences the returning back-scattered signal. This parameter is the angle between the direction of the incoming radar beam and the direction normal to earth's surface [4]. If the incidence angle is small, the sensor is closer to a nadir-look direction, resulting in a greater amount of back-scattered energy directed towards the sensor. For larger incidence angles, the look angle of the sensor is highly oblique, resulting in less energy reflected back to the sensor and more energy reflected away, which may weaken the strength of the return signal. In addition to the amplitude, the incidence angle affects the imaged footprint area and time delay between return signal in the near and far range [39, 4].

### 2.3.4 Image Formation

Radar image products are formed after the back-scattered signals are processed. Ground Range Detected (GRD) and Single-look Complex (SLC) data are two radar products commonly used for land observation. Pixels within a GRD image have been projected to ground range geometry using a chosen ellipsoid model. Only amplitude information is preserved in GRD products. Alternatively, SLC data are oriented in slant-range geometry with pixels corresponding to the side-looking nature of SAR systems and sensor-to-target distances are measured in the line-of-sight (LOS) direction [4]. SLC products are useful for change detection studies because they contain both amplitude and phase data.

SLC data are complex-valued, meaning the signals have both real and imaginary parts, also known as in-phase (I) and quadrature (Q) components. Complex signals (I/Q data) are a way of recording and preserving the three dimensional nature of electromagnetic energy. In order to capture the entire signal, SLC products store data using complex values [35]. I/Q data representation allows for more precise measurements than singular component representation [48]. For example, Figure 2.4a shows an example of how a typical waveform is pictured. However, this view is a 2D representation (side view, real component only) of the wave. Figure 2.4b shows the same wave, viewed from the top (imaginary component only), again displaying a 2D representation of the wave. Figure 2.4c shows a 3D representation of the wave (looking down the time axis), that includes both the real and imaginary components of the signal. Two dimensional representation of a wave results in the loss of signal information, which decreases the precision and accuracy of measurements made from the signals. Therefore, the use of I/Q data results in less ambiguity and uncertainty of the signal because the true signal is captured in all three dimensions [48].

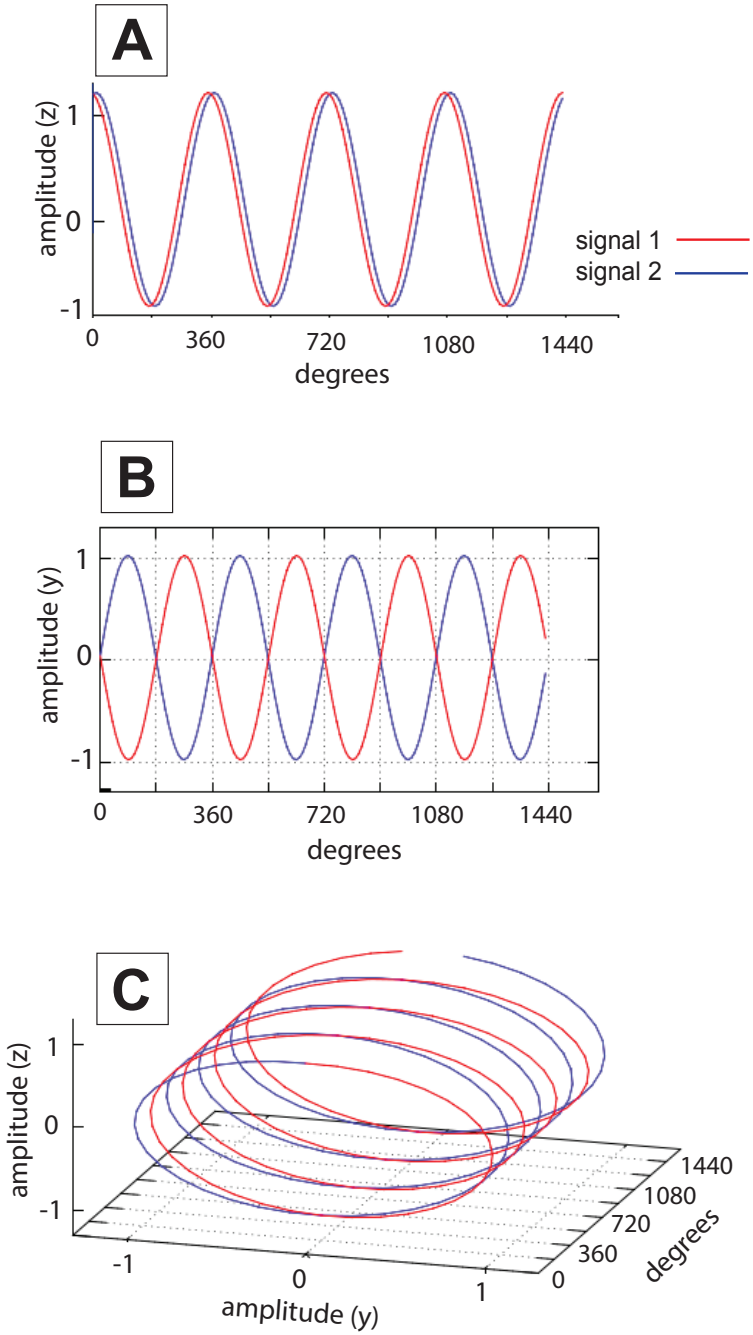


Figure 2.4: Representation of two signals (red and blue lines) using real (A), imaginary (B), and complex (C) data. (A) and (B) demonstrate two dimensional data representations, while (C) demonstrates three dimensional data representation. The shift between the two signals is not as apparent in (A) as it is in (B). Therefore, including both real and imaginary components, shown three dimensionally in (C), captures more information about the entire, true signals. Adapted from [49].

### 2.3.5 Introduction to InSAR

SAR satellites orbit the Earth and collect data about earth's surface. The analysis of temporal SAR data is an extremely useful method of evaluating, monitoring, and mapping changes caused by natural disasters. Interferometric synthetic aperture radar (InSAR) is a method of change detection and deformation mapping using SAR imagery. This method uses interferometry, where interference patterns are created from superimposed waves with the same wavelength, where constructive and destructive interference create a pattern of fringes [40, 50]. However, research of this phenomena began decades ago and was famously demonstrated by Thomas Young in his two-slit experiment [51, 52]. In radar interferometry, an interferogram is created from the phase difference of two radar SLCs, which results in a pattern of fringes or wave cycles (Figure 2.5) [39, 40]. InSAR is used to calculate information about the relative changes between radar acquisitions. The phase information for SAR interferometry can be sourced from two different images of the same area, taken at different times (repeat-pass interferometry) or from two images taken at the same time, from two different antennas (single-pass interferometry). Single-pass interferometry is typically used for topographic mapping, while repeat-pass, is often used for analysis of ground deformation over time [40].

To measure earthquake-induced ground displacement, one SLC before (primary image) and one after (secondary image) the event are used to map the interference pattern caused from co-seismic phase changes (see Figure 2.5) [34]. For successful repeat-pass interferometry, the two SLCs must be acquired from a similar location in space and image an overlapping area on the ground. The two SAR systems must have identical sensor parameters and imaging wavelength. The primary and secondary images must also be co-registered to each other. This is an essential step in InSAR processing because it aligns the SAR images, allowing the two acquisitions to be compared on a pixel-by-pixel basis. The chosen secondary image is co-registered to the primary image [29]. After processing, the fringes of a radar interferogram can be used to calculate the amount of ground displacement in the LOS direction, depending on the wavelength of the sensor [34, 40]. The interferogram can capture the co-seismic phase shift of the ground over several kilometers. Each individual fringe of the interferogram represents one half of a wavelength of displacement in the LOS direction. The total displacement in the LOS direction can be calculated by summing the displacement corresponding to individual fringes, which is called unwrapping [40].

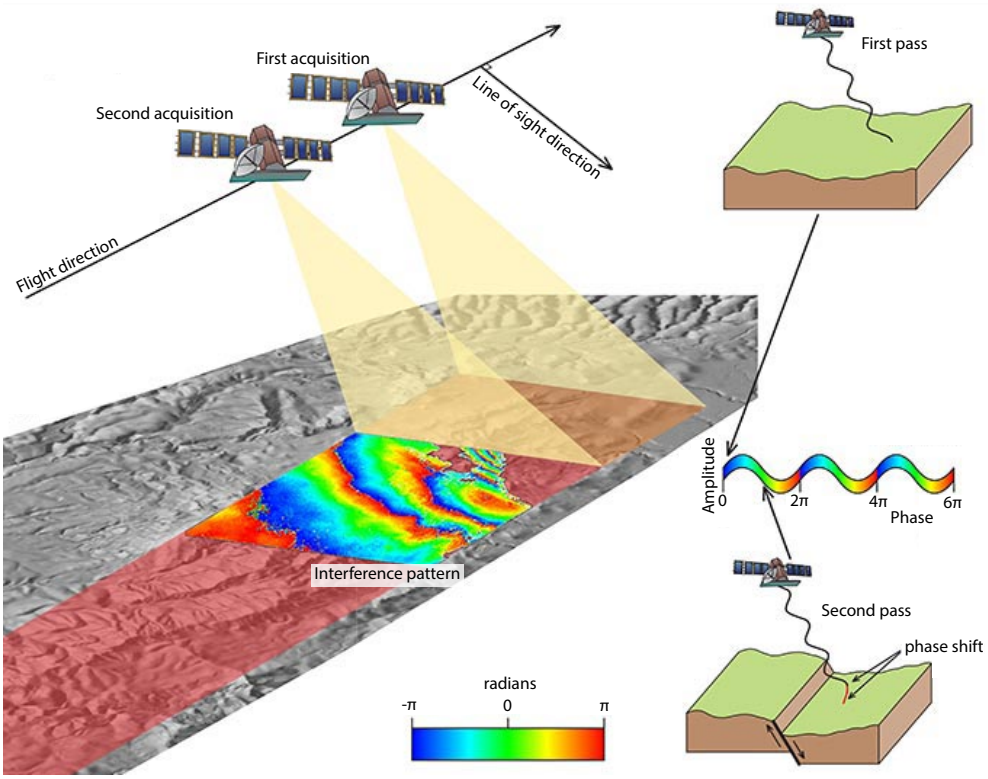


Figure 2.5: Repeat-pass interferometry. Two SAR acquisitions of the same area are collected at different times. Surface changes that occur between acquisition dates, like a fault rupture, cause an apparent phase shift between acquisitions. The phase shifts create an interferogram of fringes or wave cycles from -$\pi$ to $\pi$. Adapted from [53].

# Chapter 3

# Unusual Kinematics of the Papatea Fault (2016 Kaikōura Earthquake) Suggest Anelastic Rupture

*Reprinted from Diederichs, A., Nissen, E.K., Lajoie, L.J., Langridge, R.M., Malireddi, S.R., Clark, K.J., Hamling, I.J. and Tagliasacchi, A., 2019. Unusual kinematics of the Papatea fault (2016 Kaikōura earthquake) suggest anelastic rupture. Science Advances, 5(10), eaax5703*


*Author contributions: A.D. performed the differential lidar analysis using the sparse ICP algorithm (developed by S.R.M., A.T., and E.K.N.) and profiling codes (adapted from L.J.L.) A.D. wrote the manuscript with help from E.K.N. and with edits and insights from R.M.L., K.J.C., and I.J.H.*

## 3.1 Introduction

Complex multiple-fault earthquakes offer vital insights into the physics of rupture propagation and arrest, which are important for seismic hazard analysis and rupture forecasting [54, 55, 56, 57, 58]. However, characterizing such events can be challenging due to complex seismic and geodetic signals that result in parameter trade-offs between neighboring

fault segments in rupture models. These problems are well illustrated by the 2016 $M_w$ 7.8 Kaikōura earthquake, which cascaded across a network of dextral, sinistral, oblique, and reverse faults in the northeastern South Island, New Zealand (Figure 3.1). Published source models based on a combination of seismic, satellite geodetic, and field data exhibit a wide variety of fault geometries and complexities, with as few as 2 [59, 60] to over 20 [61] discrete rupture segments. Consequently, there are disagreements over fundamental characteristics of the earthquake, such as the dimensions between rupture segments separating the major crustal faults, and the degree to which the underlying Hikurangi subduction interface slipped co-seismically.

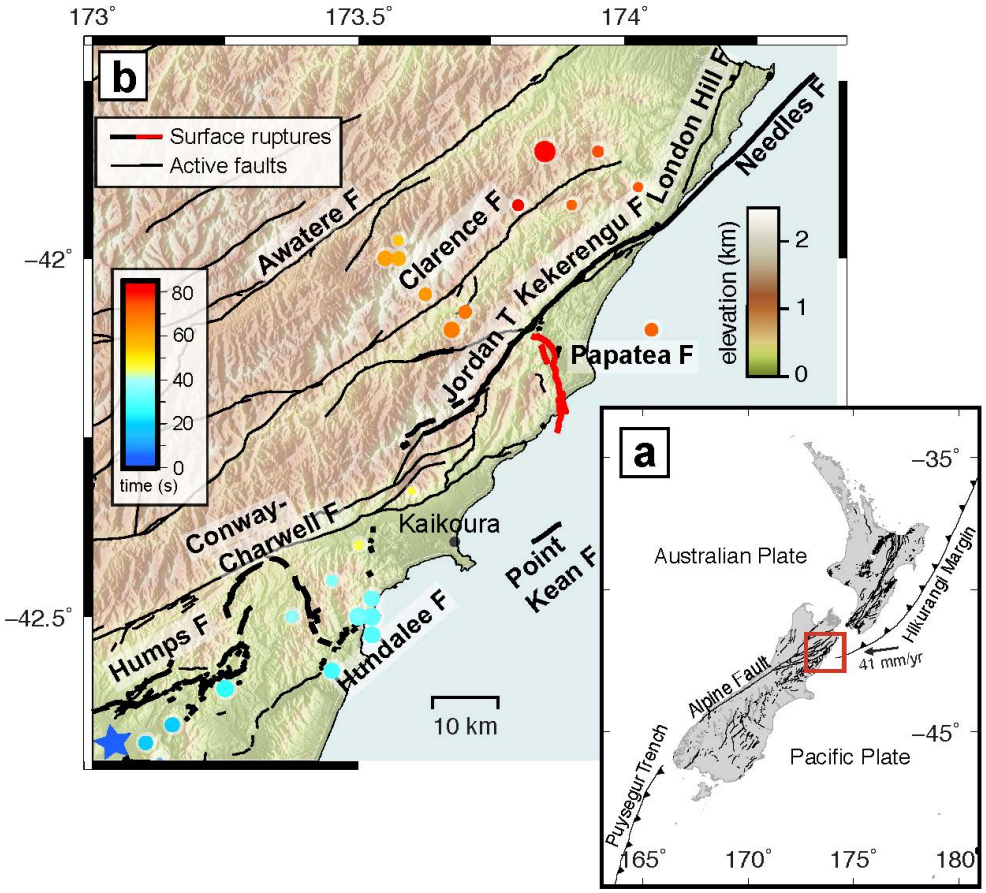


Figure 3.1: Map of the 2016 Kaikōura earthquake and surrounding area. (A) Transpressional tectonic setting of the northeastern South Island of New Zealand. (B) Map of surface ruptures from the 2016 $M_w$ 7.8 Kaikōura earthquake, shown in bold black lines with the Papatea fault in red [61, 62]. Dots represent scaled relative energy release from back-projection results [63] and are colored by time since rupture onset. Mapped active faults that did not rupture during the Kaikōura event are indicated by thin black lines [62].

The kinematics of the 19-km-long, south-striking Papatea fault (see Figure 3.1B) and its role in the Kaikōura rupture are especially enigmatic. Field surveys documented reverse-sinistral offsets of up to ∼10 m on the Papatea fault, far exceeding historical slip-to-length ratios of large earthquakes [64]. Coarse resolution three-dimensional (3D) surface displacements resolved from InSAR and SAR pixel offsets (Figure 3.2A) indicate multimeter uplift and counterclockwise vertical-axis rotation of a ∼15 km × 100 $km$ "Papatea block" in the hanging wall of the Papatea fault (Figure 3.11). Relative motion of this block, with respect to neighboring areas, was poorly fit by initial elastic models [57]. Slip on the Papatea fault is poorly resolved seismically (e.g. [54, 60]) and is associated with a notable scarcity of aftershocks [65], leaving its subsurface geometry largely unknown. Consequently, published models of the Kaikōura earthquake implement a wide variety of assumed geometries or simply exclude it altogether.

To investigate further, we used a rarely available pair of pre- and post-earthquake airborne lidar surveys and a new implementation of the iterative closest point (ICP) algorithm [25, 22, 23] to map the 3D surface displacement field along the onshore Papatea fault. By profiling this displacement field [30], we resolve the slip vector, fault dip, and rake at discrete locations along four Papatea fault ruptures. In doing so, we reveal the Papatea fault as a twisting, mostly high-angle reverse-sinistral fault, where fault dip and dip direction vary along strike. The resulting surface deformation field cannot be reproduced using conventional elastic models [57]. We conclude this fault rupture occurred in rapid response to shortening caused by neighboring elastic ruptures, rather than due to the release of accumulated interseismic strain along the Papatea fault itself, as is conventionally assumed. This may explain why the fault appears seismically quiescent in many back-projection models (e.g. refs. [60, 63, 66]). These unusual patterns in fault kinematics and anelastic surface deformation call into question assumptions about fault elasticity in complex multifault earthquakes.

### 3.1.1 The 2016 Kaikōura Earthquake

The Kaikōura earthquake occurred on 14 November 2016 at 12:03 a.m. local time (11:03 on 13 November UT) in the North Canterbury domain and Marlborough Fault System of the South Island of New Zealand (Figure 3.1A) [61, 67]. This region of transpressional tectonics marks the transition between the Hikurangi margin, where Pacific oceanic lithosphere subducts westward at ∼48 mm/year beneath the Australian plate, forming an oblique collision zone between continental portions of the same plates [68, 69]. The North Canterbury domain is characterized by relatively slow-slipping reverse faults, whereas the Marlborough

Fault System contains an anastomosing array of faster-slipping, (up to ∼2 mm/year) dextral strike-slip and thrust faults. This earthquake was the largest ever recorded in this region, with the previous strongest (the 1848 Blenheim earthquake) estimated at $M_w$ 7.5 [70].

The 2016 earthquake ruptured at least 20 faults, 13 of them with multimeter slip, making this among the most complex earthquakes ever recorded globally [57, 61]. It nucleated at ∼15 km depth on the Humps fault, as an oblique thrust fault in the North Canterbury domain, before rupturing eastward onto the neighboring Leader and Hundalee faults (Figure 3.1B). Subsequent rupture of an offshore fault or faults may be responsible for a local tsunami with up to ∼5 m run-up [17, 71]. It then propagated or jumped northward onto the Marlborough Fault System, where most of the seismic moment was released and where the largest surface slip was documented on the Jordan, Papatea, and Kekerengu faults [57, 61, 72, 73]. The earthquake terminated after ∼80 to 100 s on the Needles fault within the Cook Strait, ∼180 km northeast of the epicenter (e.g. refs. [60, 63, 71, 72, 74, 75, 76]].

The arcuate, ∼19-km-long Papatea fault (Figure 3.1B and Figure 3.2A) strikes ∼south-southeast overall between the coast and George Stream, where it converges with the ∼SW-NE–striking Jordan and Kekerengu faults, and offshore Waipapa Bay, where it may converge with other off-shore faults [61, 62]. The longer onshore section approximately follows the trace of the lower Clarence River, with steep hills in its western hanging wall and more subdued terrain in its eastern footwall. Although mapped geologically, the Papatea fault was not considered to be active prior to the 2016 Kaikōura earthquake [77].

Langridge et al. [62] mapped 2016 surface ruptures along ∼16 km of the main Papatea fault strand, a short coastal fault east of the main strand, called the Edgecombe trace, and a discontinuous western strand made up (from north to south) of the Wharekiri, Back-basin, Wainui, and offshore Okiwi ruptures (Fig. 4). They found maximum and average throw across the main strand to be 9.5 ± 0.5 and 4.5 ± 0.5 m, respectively, with maximum sinistral offsets of 6.1 ± 0.5 m. At the coast, Clark et al. [17] measured ∼4 m vertical offsets on the Wainui trace and main strand from differenced lidar DEMs, with the narrow block in between uplifted by ∼6.6 m from sea level. From satellite optical imaging of horizontal deformation across the Papatea fault damage zone, Klinger et al. [78] observed strain asymmetry consistent with northward rupture directivity, suggesting that the fault provided a linkage between southern off-shore faults and the northern Jordan and Kekerengu faults [78, 79]. One field measurement of the fault dip has been collected along the main strand at a clear cross-sectional exposure across the Clarence River, indicating a dip of 51° W [62]. Coastal field measurements along the Wainui trace indicate a near vertically dipping western strand [62]. 3D surface displacements from satellite photogrammetry now cover the entirety

of the 2016 surface rupture, but a detailed analysis of these results has been focused on other faults [73].

With such poor constraints on its subsurface dip, most early attempts at modeling the Kaikōura earthquake excluded the Papatea fault altogether [17, 57, 59, 60, 71, 74, 75]. Subsequent modeling studies have implemented the Papatea fault in a wide range of configurations from listric structures that grade into shallow (17°) angles at depth [79] to moderately dipping (47° to 70°) planar geometries [63, 66, 72, 73, 77, 78, 80, 81]. In addition to this, many studies do not clearly explain how modeled fault dips were chosen or whether they were fixed during inversion. If the Papatea fault is misrepresented in Kaikōura earthquake models, then its seismic and surface deformation signals may be misinterpreted as sourced from other nearby faults. This is emphasized by the fact that some models place maximum subduction interface slip beneath the Papatea block [72, 71].

## 3.2 Materials and Methods

### 3.2.1 3D Surface Displacements From Differential Lidar and ICP

We analyzed deformation within the Papatea fault zone using 3D differential lidar surface displacement fields sourced from pre- and post- event airborne lidar surveys collected in July 2012 and November 2016 to January 2017 (see Clark et al. [17] for further details of these datasets). The double coverage captures most of the onshore Papatea fault, with only a short middle section and the northernmost intersection with the Jordan and Kekerengu faults missing. With no other major earthquakes occurring within this time frame in this area, differencing the pre- and post-event lidar data captured the co-seismic deformation of the 2016 Kaikōura earthquake. This repeat lidar dataset was previously analyzed by Langridge et al. [62], and the coastal part by Clark et al. [17], using differenced DEMs. The resulting elevation change maps provide a high spatial resolution measure of vertical deformation but are subject to biases from the unconstrained horizontal components of the displacement field, which are likely to be substantial in this area.

To overcome this problem, we used the ICP algorithm to align square subsets ("cells") of the pre-event lidar point cloud to equivalent subsets of the post-event point cloud [65]. This retrieved the 3D rigid body transformation (translations and rotations around Cartesian axes) that minimized average closest point distances between each pair of cells. Using the provided point classifications, we first stripped each point cloud of all vegetation, building, and water returns, leaving only the bare earth surface. For the ICP alignment, we

implemented a "sparse ICP" approach [22] with point-to-plane alignment within a MATLAB source code. This approach uses sparsity-inducing norms that unify various criteria for down weighting outliers, data gaps, and geometric boundaries [23] under a single parameter p. This parameter is the exponent of the sparse norm with a value between 0 and 1. This technique allowed for automatic classification of outliers and inliers, where the latter were given greater prominence in the next iterative step, unlike traditional ICP methods that do not distinguish between outliers and inliers. Overall, this approach yielded a robust algorithm that reduced the impact of outliers and data gaps, which would otherwise lead iterative registration toward erroneous local, rather than global, minima [22]. After experimentation, we used a 50 m cell size with an additional 10 m border around the post-event cells to capture any lateral shift of topography in the earthquake [18]. We used a sliding window to enhance the spatial resolution further, for a final displacement grid resolution of 25 m.

The resulting Cartesian x, y, and z axis transformations represent local surface displacements in the east-west, north-south, and up-down directions, respectively (Figure 3.2B). Deformation is coherent along many of the Papatea fault surface ruptures, which are clearly expressed as sharp displacement discontinuities in the displacement fields. However, the Back-basin and Corner Hill faults [62] did not show clear discontinuities and are not included in our analysis. Coherence is lost in a few areas, most notably where land sliding or reorganization of the Clarence River have wholly altered the shape of the topographic cells, rendering the scattered ICP alignments meaningless. Vertical displacements are smoother (less noisy) than horizontal displacements, in common with other earthquake surface displacement fields mapped using ICP (14), reflecting the fact that topographic ground returns are most closely spaced in the z dimension. In comparison, Hamling et al.'s [57] 3D displacement field derived from SAR interferometry and pixel offset measurements is an order of magnitude coarser ($\sim$330 m $\times$ 450 m) and appears highly pixelated (see Figure 3.2A and B). Co-located SAR- and lidar-derived displacements show multimeter-level scatter but no systematic offset in either of the x, y, or z displacement components (Figure 3.3). Visually, the lidar displacements appear in reasonable agreement with those derived from differential photogrammetry [73], although we are unable to make a statistical comparison between the two.

The fine detail evident in the lidar data proved crucial in being able to profile the displacement field, measure fault offsets, and, thus, resolve fault dip. This was especially the case along the coastal section of the Papatea fault, where we observe all three displacement components changing over short, sub-kilometer distances on three closely spaced fault

strands.

### 3.2.2 Fault Slip Vector, Dip, and Rake Measurements

For our detailed analysis of the Papatea fault geometry and kinematics, we adopted and modified an approach developed by Lajoie et al. [30] in their analysis of the 2010 El Mayor-Cucapah (Mexico) earthquake. The first step was to map rupture traces directly from the clear discontinuities in surface displacements. Next, fault-perpendicular swath profiles were extracted through each of the x, y, and z displacement fields at regular intervals along each rupture trace (examples are given in Figure 3.2C to H). Co-seismic fault offsets were measured from each profile by calculating least squares linear fits through displacement data points on each side of the fault damage zone, extrapolating these trends to the fault, and differencing them. This procedure offers three key advantages over geological methods of measuring fault offsets from single post-earthquake surveys: (i) There is no assumption that the data trends on either side of the fault represent surfaces of the same age; (ii) there is no need to assume initial surface or landform geometries; and (iii) offset measurements are no longer prone to biases arising from landform geometry. Offset uncertainties were estimated by extrapolation and differencing of the 50% confidence bounds. After testing, we used swath profiles with lengths of 900 m and widths of 100 m to ensure that coherent ground displacements were captured on either side of the fault, given the presence of noise (e.g. landslides, Clarence River) and distributed deformation within the fault damage zone. In practice, only a subset of profiles could be used in subsequent measurements due to the variable quality of the deformation field.

At each measurement point, the x, y, and z offsets together describe the Cartesian fault slip vector, which by definition must lie in the plane of the fault. Paired with the local fault strike measured at the start of the procedure, this slip vector thus defines a unique fault dip and rake (an exception would arise where the slip vector is horizontal and parallel to the fault trace, as for a pure strike-slip fault — see Lajoie et al. [30] for a discussion — but for the oblique Papatea fault, this is never the case). In an advance on the procedure outlined by Lajoie et al. [30], we also propagated estimated uncertainties in the x, y, and z offsets into uncertainties in fault dip. We did so using a Monte Carlo simulation, calculating dip 100 times using random draws from Gaussian distributions in the x, y, and z offsets, and determining standard deviation values of the resulting dip distribution. In this way, and where the lidar coverage and quality permit it, we were able to determine the vertical, lateral, and fault normal components of slip, the net slip, the fault dip, the rake, and the

statistical uncertainties in these parameters at closely spaced intervals along each of the four strands of the Papatea fault.

## 3.3 Results

We used pre- and post-earthquake airborne lidar to map 3D surface displacements along the Papatea fault and profiled the deformation field (Figure 3.2) to map slip vector and dip distributions [25, 22, 23, 30]. Figure 3.4 shows net slip (red) and fault dip (blue), as well as the lateral and vertical components of the slip (black) as a function of distance along the strike, for all profiled fault traces. All results are tabulated in Table A.1.

### 3.3.1 Fault Geometry of the Main Strand

We collected 34 slip, dip, and rake measurements along the main strand of the Papatea fault, using a simplified trace (Figure 3.5) to approximate the fault. The main strand is characterized by multimeter vertical (west side up; Figure 3.4E) and left-lateral offsets (Figure 3.4D), but we found that the fault geometry changes substantially along the strike. At its northern end (∼0 to 1 km distances on Figure 3.4A), it accommodates a net slip of ∼7 to 8 m, with vertical and left-lateral components of ∼6 to 7 and ∼2.5 to 4.5 m, respectively. This section of the fault is sub-vertical, as indicated by large vertical displacements with horizontal slip vectors that closely parallel the fault (Figure 3.5). Moving southward, slip increases on a progressively shallowing, W-dipping fault plane, culminating at ∼3.5 km along the strike with peak slip of ∼11.5 m, coeval with a local minimum in fault dip of ∼56° W. This measurement point is close to the exposure across the Clarence River, with a measured dip of ∼51° W [62]. Further south, the fault steepens to ∼70° to 80° at ∼5-km distance while retaining a high slip of 9 to 11 m and attaining a peak throw of ∼9.5 m. South of ∼6 km along the strike, lidar coherence or coverage is lost for a distance of ∼4 km. Accounting for changes in dip direction at its northern tip, the northern ∼5 km of the main strand has average and standard deviation values in net slip of 9.0 ± 1.3 m, throw 7.8 ± 1.1 m, left-lateral slip 3.9 ± 0.9 m, dip 81° W ± 12°, and rake 64° ± 6°. The rather narrow parameter ranges are despite a pronounced curvature of up to 73° in fault strike.

Near the middle of the main strand fault trace, ∼6 km from its northern end, there is a ∼4-km gap in double lidar coverage. South of this gap, the double lidar coverage along the coast captures a ∼1-km-long fault section (see dashed polygon in Figure 3.5). Here, we obtained very similar horizontal slip vectors to the northern fault section, but much smaller

vertical offsets (averaging 2.8 ± 1.0 m) and consequently shallower dip values (58° W ± 17°). We also determined average and standard deviation values in net slip of 5.4 ± 1.1 m, left-lateral slip of 4.1 ± 0.6 m, and rake of 40° ± 7°. Along-strike gradients in slip, dip, and rake greatly exceed those of the northern main strand section, likely reflecting that the coastal section is part of a step-over zone in which slip is transferred westward onto the Wainui and offshore Okiwi traces.

### 3.3.2 Fault Geometries of the Wharekiri, Wainui, and Edgecombe Traces

We collected 15 slip, dip, and rake measurements along the north- northwest (NNW) striking, eastward-dipping (Figure 3.4B) Wharekiri trace in the hanging wall of the main strand. The Wharekiri rupture is characterized by clear vertical (east side up, Figure 3.4G) and sinistral offsets (Figure 3.4F) over a distance of ∼3 km, but offsets in the east-west (E-W) displacement field are much harder to discern (Figure 3.2B). Peak net slip of ∼2.1 m, throw of ∼1.7 m, and left-lateral slip of ∼1.2 m are observed ∼2 km along the measured section. Slip vectors point consistently toward the NNW, sub-parallel to the rupture trace (Figure 3.5). We calculated average and standard deviation values of 1.5 ± 0.3 m in net slip, 1.2 ± 0.4 m in throw, 0.9 ± 0.3 m in left-lateral slip, 81° E ± 12° in dip, and 52° ± 12° in rake.

We analyzed ∼1-km sections of the westward-dipping Wainui and Edgecombe traces, on either side of the coastal section of the main strand. The Wainui trace is most evident in the vertical displacement field (Figure 3.2B), with east side up sense; we determined up to ∼4.4 m of predominantly normal slip on a steep (68° to 90°) west-dipping fault (Figure 3.4C, H, and I). The Edgecombe trace shows less scatter in the horizontal components. We estimated up to ∼3.5 m sinistral-thrust motion on a low-angle westward-dipping fault (Figure 3.4C, H, and I).

## 3.4 Discussion

### 3.4.1 Comparison to Field Measurements

In general, our offset measurements are in reasonable agreement with those measured in the field or from lidar elevation change maps from Langridge et al. [62]. One exception is along the eastward-dipping Wharekiri trace, where we found consistent left-lateral offsets of 0.4 to 1.4 m and maximum throw of ∼1.7 m, but Langridge et al. [62] reported no field evidence

for lateral displacement and an isolated peak of ∼3.0 m in throw. A second exception is along the Wainui trace, where we observed large (∼4 m) throw and small (∼0.5 m) dextral motion, but Langridge et al. [62] reported smaller (< 3 m) throw and small (∼0.5 m) sinistral motion. Along all faults, our measured offsets vary more smoothly along strike with lower scatter than those of Langridge et al. [62]. This is especially true of the lateral components. These were measured in the field by extrapolating piercing lines (mostly cultural features like fences and roads) within ∼100 m of the primary rupture trace, close to or perhaps even within the fault damage zone [62]. In contrast, by using swath profile displacements over an aperture of 900 m and extrapolating only the "far-field" linear data trends, we captured the cumulative offset across the fault damage zone. Simple elastic forward models suggest that our profiles are most sensitive to slip in the upper ∼2 km. Nevertheless, our measurements are not consistently larger than those of Langridge et al. [62], implying that any shallow slip deficit is small. Mackenzie and Elliot [82] pointed out that along oblique faults, unrecognized fault-perpendicular slip components (heave) can influence the apparent lateral offset of piercing lines, leading to measurement biases that scale with the obliquity of the piercing line to the fault. Since heave is often the most difficult slip component to survey in the field—particularly when it is reverse sense — we suspect that this bias may have influenced some of Langridge et al.'s [62] more scattered measurements. In contrast, our own lateral offsets are extracted from the displacement field, rather than from piercing lines, and are not prone to such biases. Langridge et al.'s [62] vertical offsets are generally smoother and closer to our own, which reflects that they differenced the same paired differential lidar data as the main procedure to determine throw.

### 3.4.2 "Twisted" Fault Geometry

Our measurements of fault dip are of mixed consistency with values reported by Langridge et al. [62]. Our average dip for the Wharekiri trace of 81° E confirms Langridge et al.'s [62] suspicion that this fault is steeply dipping, and our average dip for the Wainui trace of 77° W is close to their average field measurement of 84° W. On the main strand, Langridge et al. [62] estimated a 55° W ± 10° fault dip. The closest lidar profile-derived dip measurement is within a few degrees of this single- field data point, at 56° W. However, this point represents a local minimum in dip along strike, and we found a much steeper average dip of 81° W within the northern Clarence Valley section as a whole. At the coast, the main strand alone dips 58° W, but far-field displacements suggest that the three coastal faults converge or merge at depth into a more gently dipping structure, with estimated dip ∼25 to 48° W (Figure 3.6).

Near the coast, the main strand is straddled to the west by the Wainui trace - which may merge offshore with the Okiwi trace - and to the east by the shorter Edgecombe trace (Figure 3.6A). All three faults are W-dipping, with progressively steeper dips from east (Edgecombe) to west (Wainui), such that the faults likely converge or merge at depth. To estimate the dip of the underlying master structure, we determined cumulative fault zone offsets along 100 m interval profiles by extrapolating far-field displacements from outside of the fault zone to the central fault (Figure 3.6D - E). Resulting dip values of ∼25-48° W are considerably gentler than those of the northern Papatea fault zone, ∼5 km to the north. Schematic cross sections along two profiles imply significant complexity in fault geometry and kinematics, likely reflecting the step-over and transferal of strain between the western (offshore Okiwi strand) and the main strand (Figure 3.6B - C).

Collectively, our results indicate substantial variations in fault dip along strike. If the Wharekiri and Wainui traces belong to the same fault, as Langridge et al. [62] suggest, then this structure twists from steeply E-dipping in the north to steeply W-dipping at the coast, with consistent relative uplift of the eastern side of the fault. The Papatea fault shows even greater variability, dipping subvertically at the northern end of the profile, ∼60° W at ∼3 to 4 km, and 70° to 80° W at ∼5 km along strike. At the coast, the bulk fault zone dips just 25° to 48° W. Thus, the Papatea fault cannot be characterized as a single planar structure, as it is represented in the majority of the published Kaikōura earthquake rupture models. To capture accurately these geometrical changes, we suggest that future modeling studies explore parameterising the Papatea fault as multiple fault planes that "twist" from sub-vertical dips in the north to much gentler dips at the coast. Despite these dip variations, as well as coincident changes in fault strike, we note that the horizontal slip vector shows remarkable consistency in azimuth and length along all of the main strand, suggesting coherent southeastward motion (as well as uplift) of the Papatea block relative to the eastern footwall (Figure 3.5).

Our results also demonstrate consistencies with those of Zinke et al. [73], who derived 3D surface deformation fields for the Kaikōura earthquake using optical image correlation and estimated fault geometries of a number of rupture strands, including the Papatea and Wharekiri faults. Their calculated median dip of 65° W ± 20.4°, peak net slip of 11.0 m, and a maximum fault dip of 89.1° W along the main strand are in reasonable agreement with our results. Their average net slip of ∼1.8 m along the Wharekiri trace also agrees well with our results, although their average dip of 56° ± 23.6° is shallower. We do note that our own lidar-derived estimates of fault dip demonstrate lower scatter with greater sample density from finer-resolution displacement maps, although, of course, Zinke et al.'s [73] displacement

fields capture the entire rupture zone.

### 3.4.3 Unusual Kinematics

With peak throw of ∼9.5 m and maximum fault dip near vertical, rupture of the ∼19-km-long Papatea fault in the 2016 Kaikōura earthquake violates two important norms in co-seismic fault behavior. First, peak net slip of ∼11.5 m and mean net slip of ∼8.3 m on the main strand far exceed values expected from empirical slip-to-length relationships [64]. As discussed by Langridge et al. [62], this observation alone has important repercussions for interpretations of paleoseismic data and for seismic hazard studies, particularly within regions of diffuse faulting like the Marlborough Fault System, where multifault ruptures may be common. Second, vertical offsets of ∼6 to 9.5 m along the northern Papatea fault, where average dip exceeds 70°, contradict the theory of Andersonian mechanics, which supposes reverse faults usually occur with shallow dips of ∼30° [83].

### 3.4.4 Anelastic Surface Deformation

Hamling et al. [57] used rectangular dislocations within an elastic half-space to invert InSAR data for co-seismic slip in the Kaikōura earthquake but could not fit surface displacements surrounding the Papatea fault with this model. We re-examined this using simple forward models of the Papatea fault by simplifying its curvilinear surface trace with nine connected rectangular dislocations, each extended to 10-km depth within an elastic half-space [83] and imposing representative values of fault slip, dip, and rake on each segment. Like Hamling et al. [57], we find that the simple elastic model fits the lidar data very poorly, especially in the vertical displacement direction, where the model predicts much smaller hanging wall uplift but much larger footwall subsidence than the data indicate (Figure 3.7). We also tested the influence of forward modeling slip along (i) a low-angle extension of the steep surface Papatea fault (for an overall listric geometry; Figure 3.8), (ii) the Jordan and Kekerengu faults (Figure 3.9), and (iii) the underlying subduction interface (Figure 3.10). We based the geometries and slip values of these additional, neighboring faults on published Kaikōura earthquake rupture models [57, 59, 60, 71, 72, 73, 74, 75, 80]. However, the discrepancies between the observed and forward modeled surface deformation fields still could not be reconciled.

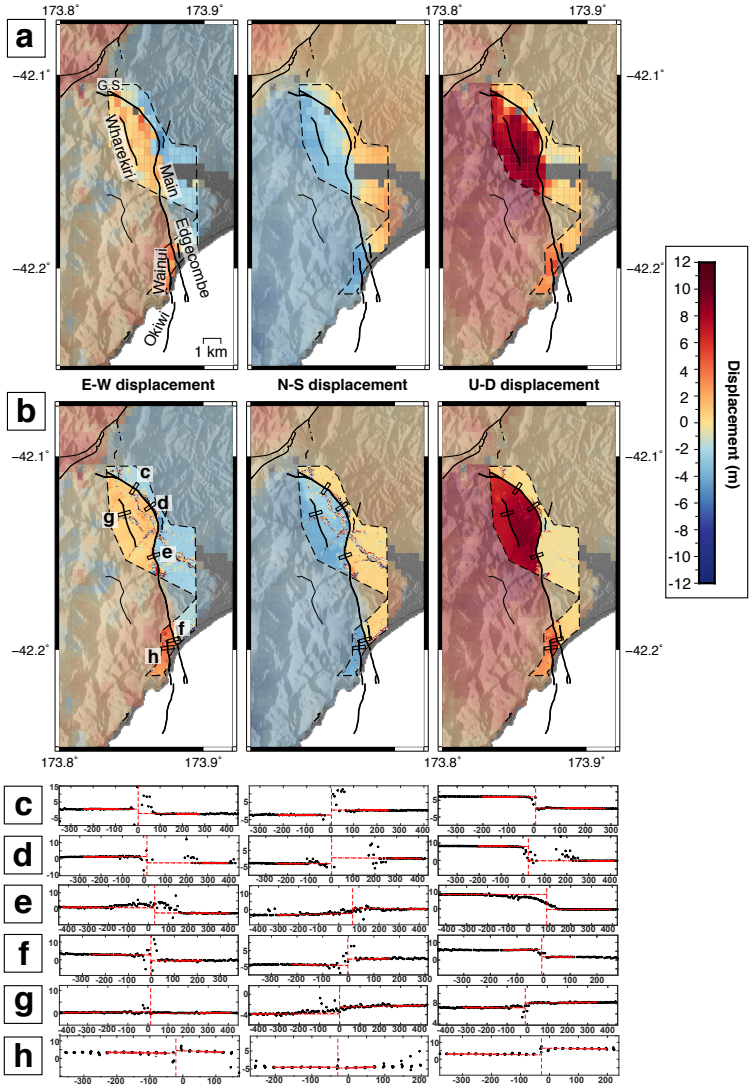


Figure 3.2: 3D displacement fields around the Papatea fault with sample fault-perpendicular profiles. (Left) E–W, (middle) N–S, and (right) up–down surface displacement fields around the Papatea fault from (A) SAR measurements [∼330 m × ∼450 m pixel resolution, from Hamling et al. [57]] and (B) D-lidar calculations (25 m) within the dashed line polygon. Positive displacement directions are east, north, and up. Coarser resolution displacement pixels outside the polygon of double lidar coverage are SAR measurements [57]. G.S. labels the location of the George Stream. Thick black lines are Papatea surface ruptures. (C to H) Example 100 m × 900 m fault-perpendicular profiles [black rectangles in (B)] through the x (left), y (middle), and z (right) lidar surface displacement fields. The vertical axis is displacement, and the horizontal axis is distance, both in units of meters. Each black dot is a single-cell displacement, vertical dashed red lines show the fault scarp, and horizontal red lines show extrapolated linear fits of chosen data points with 50% confidence bounds (dashed).

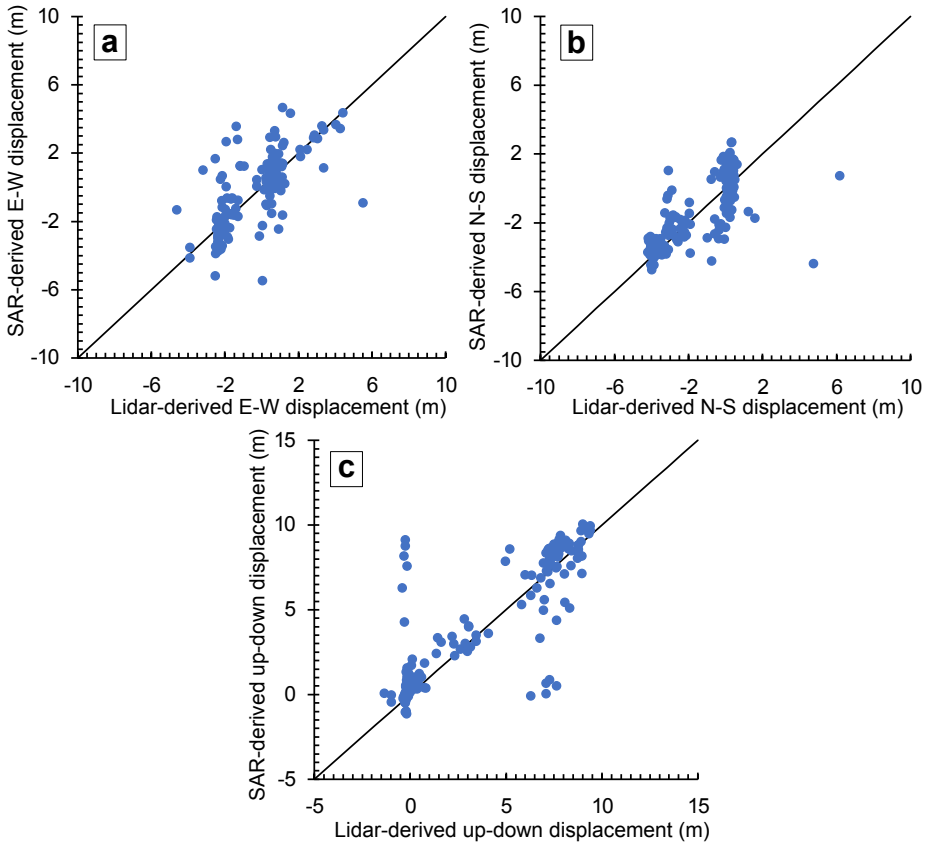


Figure 3.3: Scatter plots of SAR-derived displacements from Hamling et al. [57] (vertical axes) and block median differential lidar displacements (horizontal axes), in the (A) E–W, (B) N–S, and (C) vertical axis directions. The differential lidar block median values were calculated at the pixel resolution of the SAR-derived displacement field.

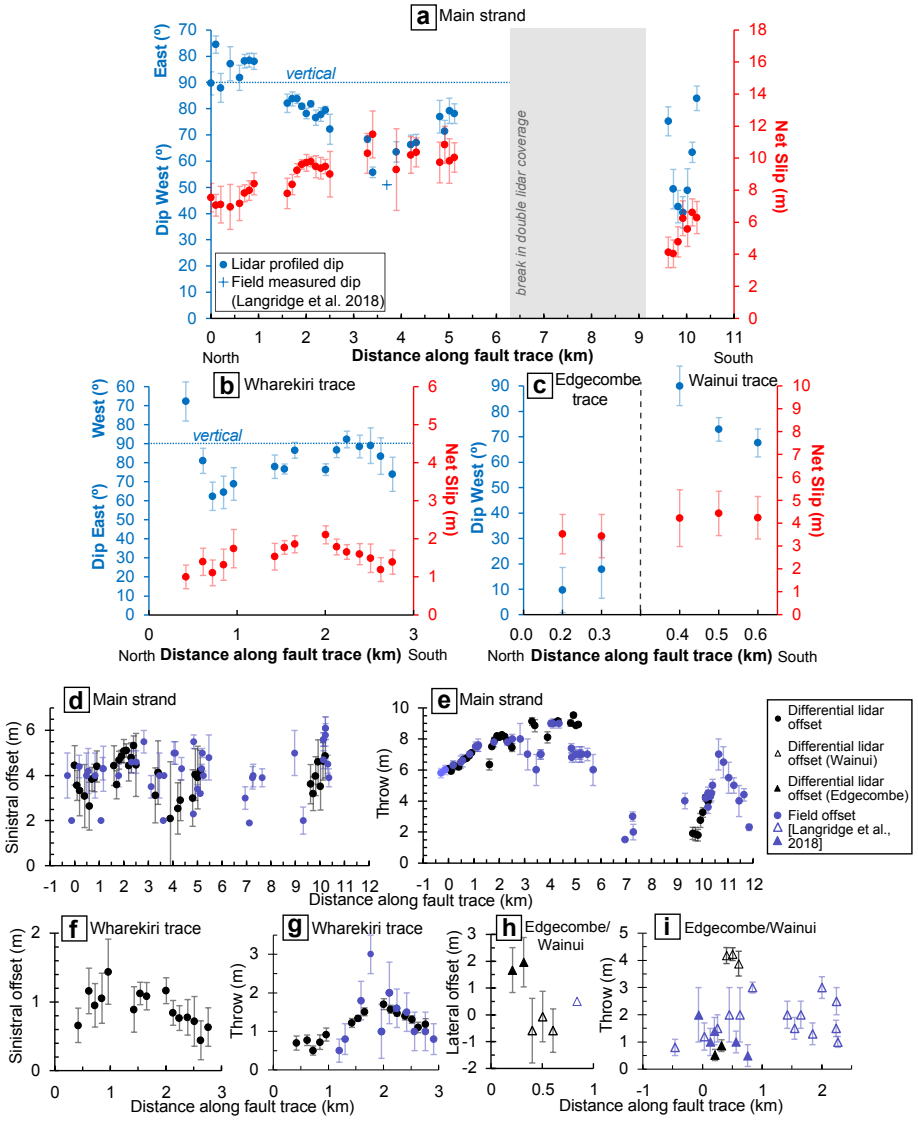


Figure 3.4: Fault kinematics from rupture profiling. Lidar-derived net slip (red) and fault dip (blue) measurements for the (A) main strand, (B) Wharekiri trace, and (C) Edgecombe and Wainui traces of the Papatea rupture. Uncertainties in slip (pink bars) are calculated from 50% limits in displacement drawn from each swath profile. Uncertainties in fault dip (light blue bars) are $\pm$ 1 $\sigma$ values of a distribution of dips yielded from a Monte Carlo simulation. Lateral and vertical slip components along strike of the Papatea fault strands (black datapoints, with $\pm$ 2 $\sigma$ uncertainties) and from field and lidar elevation change measurements [62] (purple datapoints with uncertainties where available) for the (D and E) main strand, (F and G) Wharekiri trace, and (H and I) Edgecombe (sinistral, solid triangles) and Wainui (dextral, open triangles) traces. Distances along the horizontal axes are from north to south of each fault trace and correspond to the 1-km markers (gray dots) in Figure 3.5.

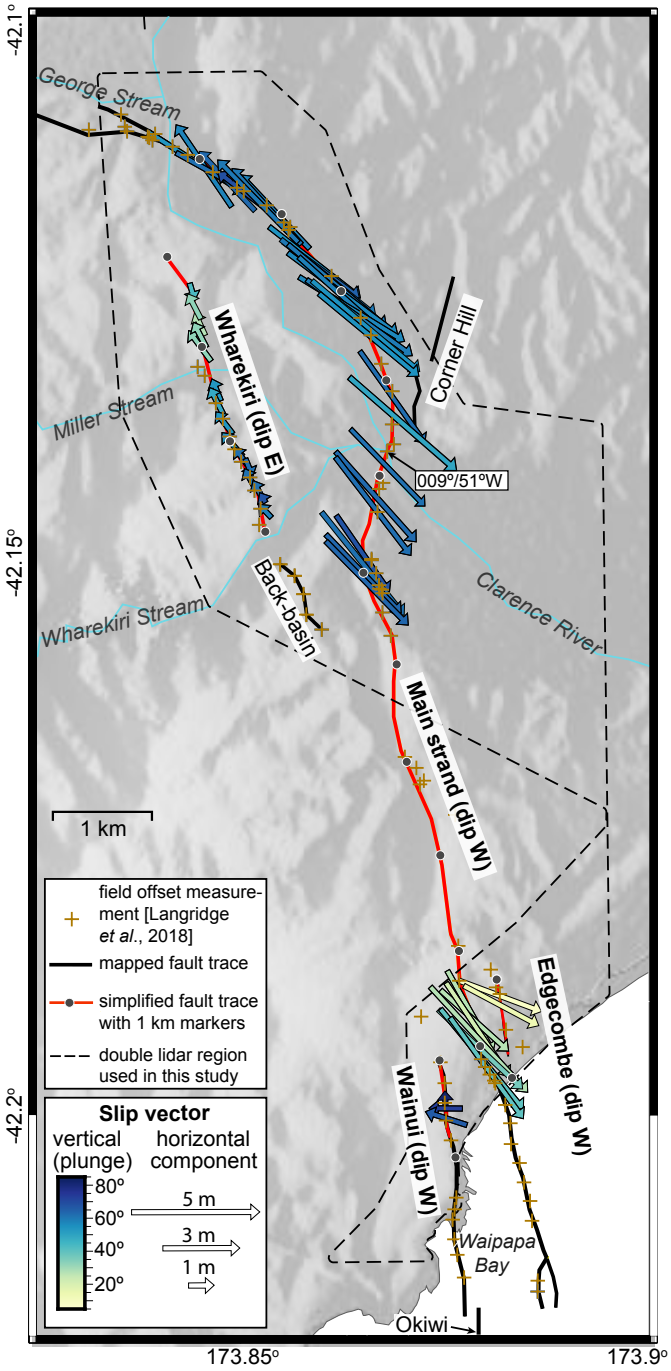


Figure 3.5: Map of the Papatea fault zone. Lidar-derived fault slip vectors (arrows) colored by plunge, showing hanging wall motion relative to footwall (note vectors flip with changing dip direction). Slip vectors were measured from swath profiles taken perpendicular to the simplified fault traces in red, which closely approximate the published, mapped fault traces shown in black [62]. Gray dots along the red line mark 1-km distance increments along each fault strand (starting from 0 km at each northern end) and correspond to the horizontal axes in Figure 3.4. The black dashed line polygon shows the region of double lidar coverage considered in this study. Field measurement localities [62] are indicated by brown plus signs.

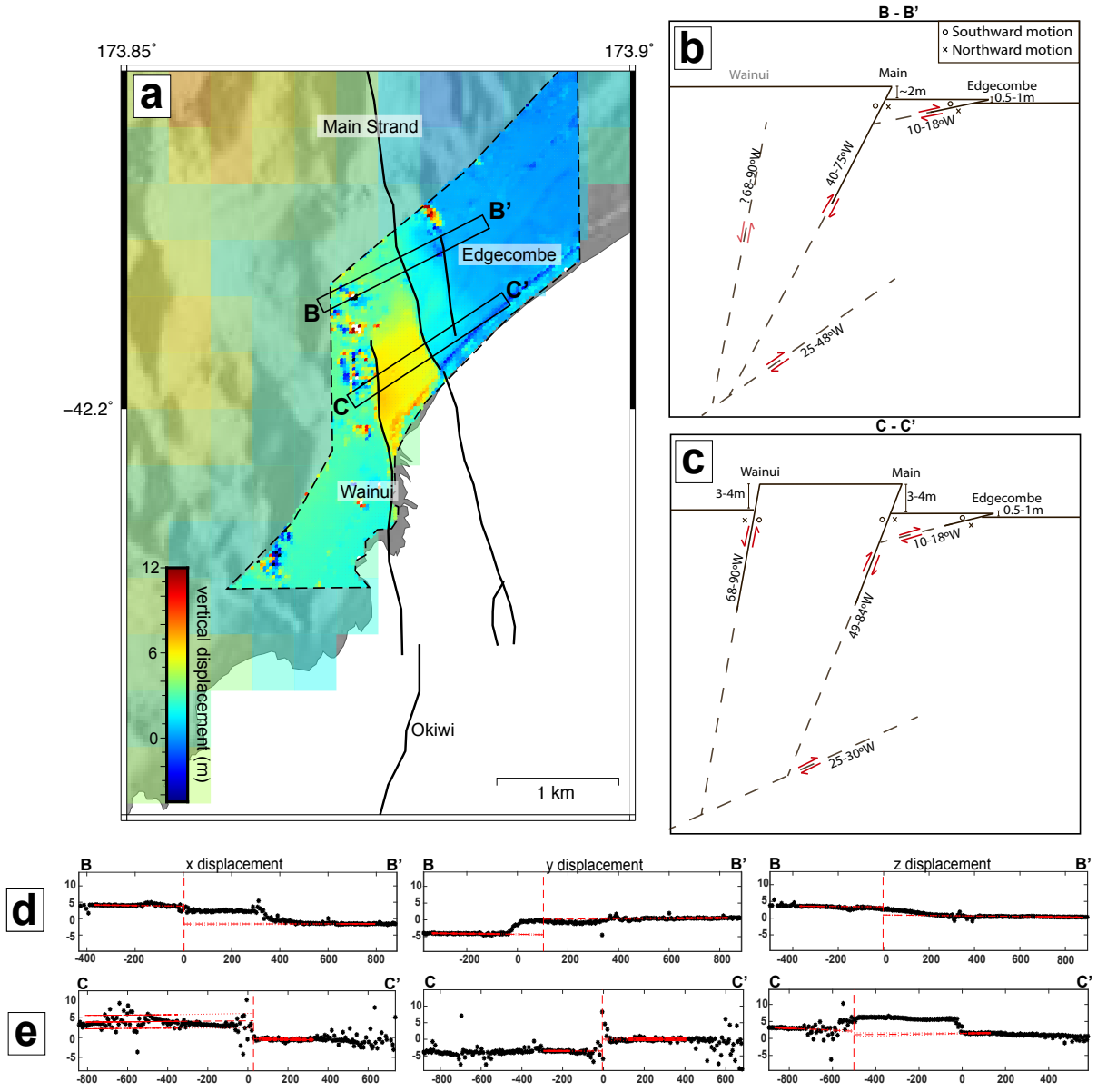


Figure 3.6: Kinematics of the coastal Papatea fault zone. (A) Differential lidar vertical displacements in the coastal section of the Papatea fault zone. Outside the lidar double coverage area, marked by the dashed black polygon, vertical displacements are from Hamling et al. [57]. Fault-perpendicular swath profiles used to derive dips in panels (B) and (C) are shown by black rectangles B-B' and C-C'. (B) Schematic cross section B-B' portraying both the shallow dip of individual strands and deeper fault dip, estimated from far-field offset extrapolated to the main strand. Strike-slip components are represented by open circles (southward motion) and crosses (northward motion). (C) Schematic cross section C-C', estimated as in (B). (D - E) Sample profile swaths through the x (left), y (middle) and z (right) lidar surface displacement fields that correspond to B-B' (D) and C-C' (E).

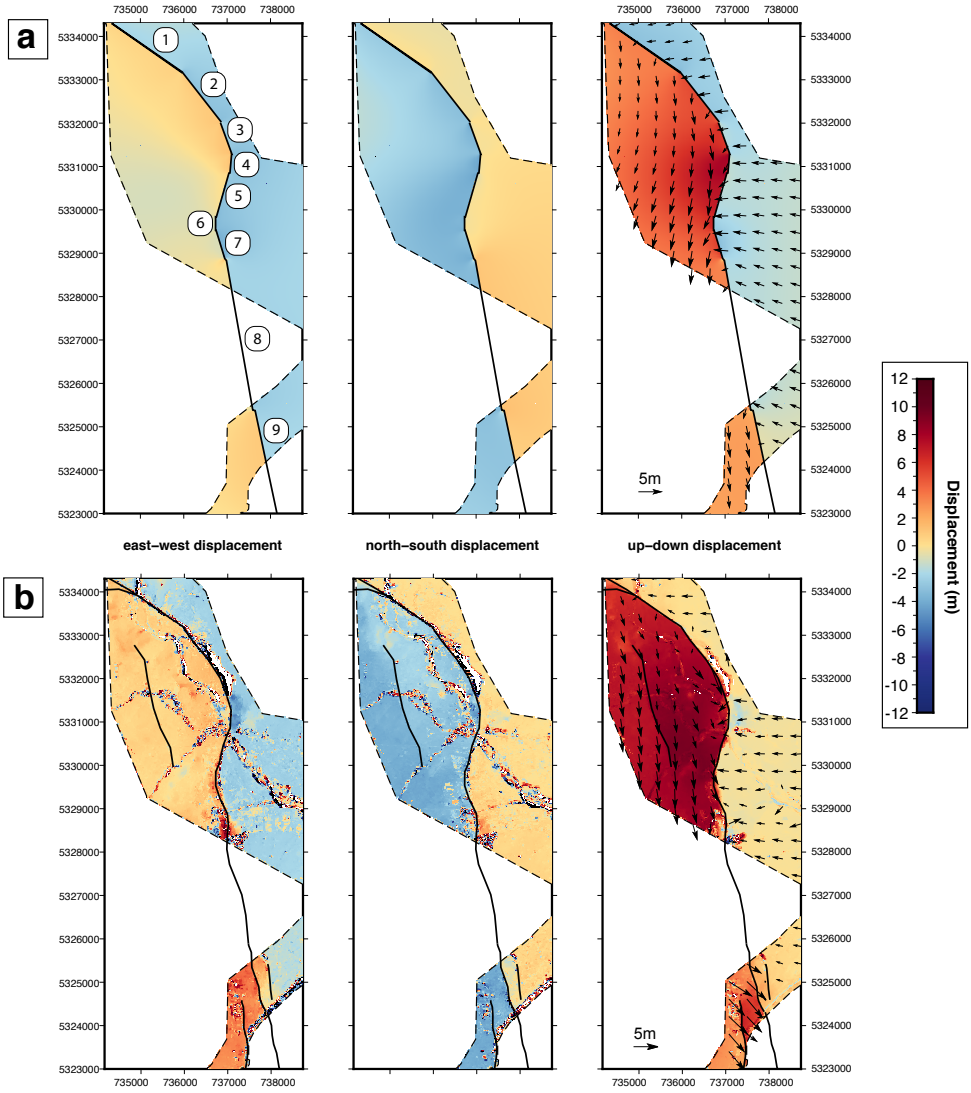


Figure 3.7: Comparison of lidar-derived 3D displacement field to elastic-modeled surface deformation around the Papatea fault. (Left) E-W, (middle) N-S, and (right) up-down (A) elastic model and (B) observed surface displacement fields around the Papatea fault. In (A), we use nine rectangular dislocations (numbered in white circles) embedded in an elastic half-space [83] to a depth of 10 km, imposing values of dip, rake, and slip that are representative of our lidar profiling measurements (see Table A.2 for model inputs). The black lines show the model fault trace, and dashed black lines show the extent of the double lidar coverage. The black lines in (B) show the mapped fault traces. Black vectors overlying the up-down displacement fields indicate horizontal displacements calculated using a block mean of dimension 400 m $\times$ 400 m.

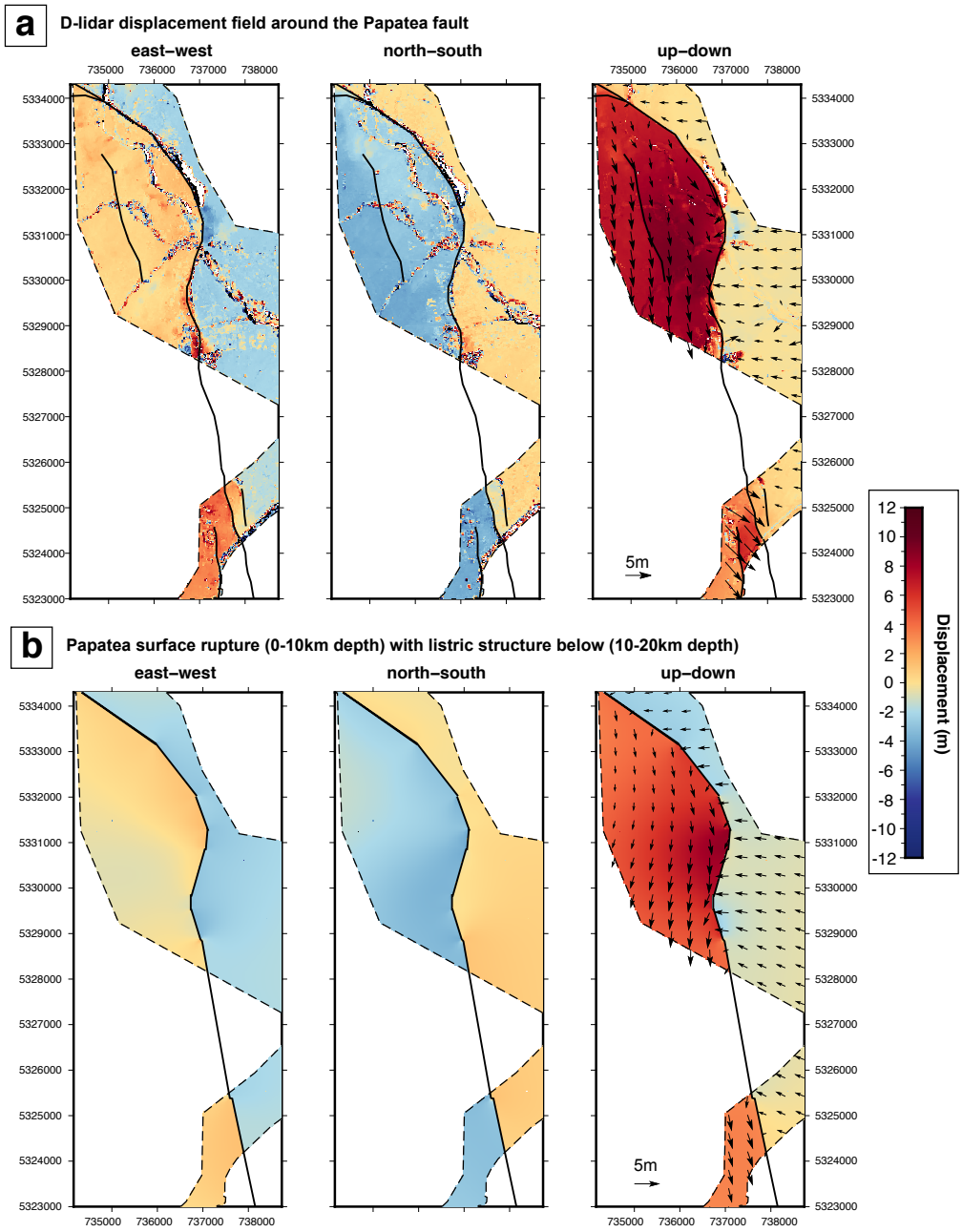


Figure 3.8: Comparison of lidar-derived 3D displacement field to elastic modeled surface deformation around the main strand surface rupture with listric structure below. (Left) E-W, (middle) N-S, and (right) up-down surface displacement fields observed from (A) differential lidar and (B) an elastic forward model of the main strand rupture together with a gently-dipping rupture below it, at 10–20 km depth. Dashed black lines showing the extent of the double lidar coverage and black vectors overlying the up- down displacement fields indicate horizontal displacements calculated using a block mean of dimension 400 m× 400 m. Black lines in (A) are mapped fault traces. Model parameters for (B) are tabulated in Table A.2.

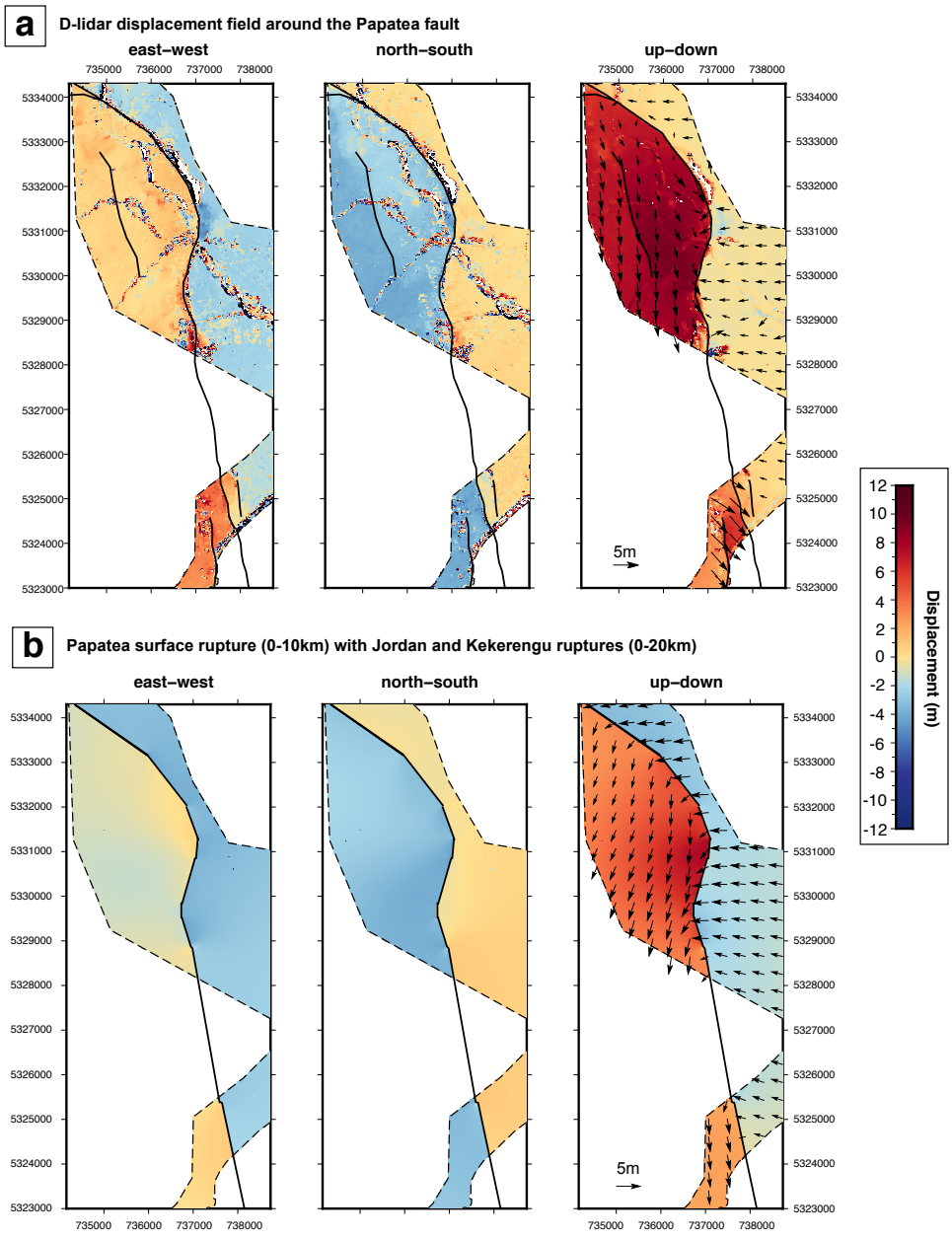


Figure 3.9: Comparison of lidar-derived 3D displacement field to elastic modeled surface deformation around the main strand surface rupture with Jordan and Kekerengu ruptures. (Left) E-W, (middle) N-S, and (right) up-down surface displacement fields observed from (A) differential lidar and (B) an elastic forward model of the main strand rupture together with the Jordan and Kekerengu fault ruptures. Dashed black lines showing the extent of the double lidar coverage and black vectors overlying the up- down displacement fields indicate horizontal displacements calculated using a block mean of dimension 400 m$\times$ 400 m. Black lines in (A) are mapped fault traces. Model parameters for (B) are tabulated in Table A.2.

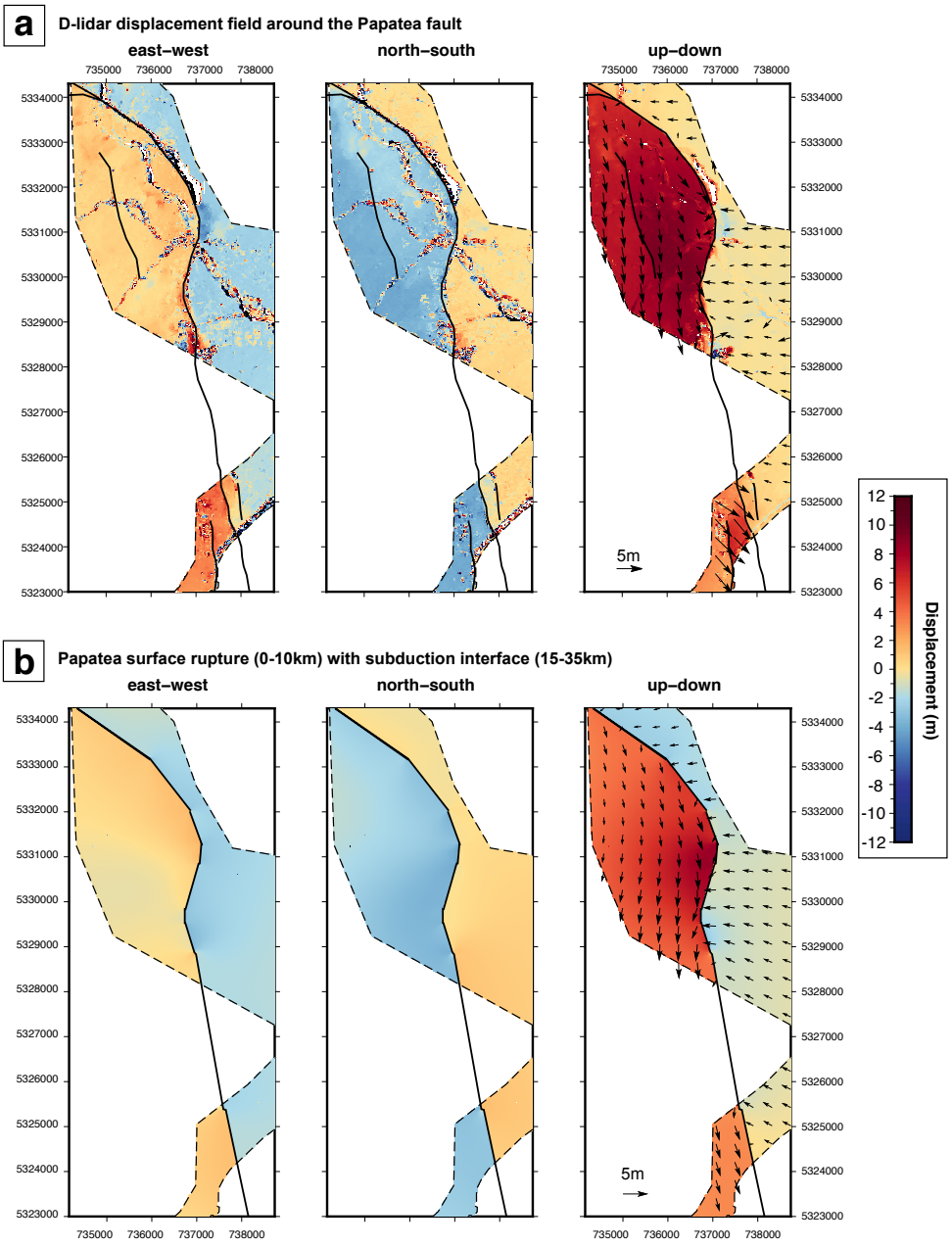


Figure 3.10: Comparison of lidar-derived 3D displacement field to elastic modeled surface deformation around the main strand surface rupture with plate interface below. (Left) E-W, (middle) N-S, and (right) up-down surface displacement fields observed from (A) differential lidar and (B) an elastic forward model of the main strand rupture together with 2 m of slip on the subduction interface below. Dashed black lines showing the extent of the double lidar coverage and black vectors overlying the up-down displacement fields indicate horizontal displacements calculated using a block mean of dimension 400 m× 400 m. Black lines in (A) are mapped fault traces. Model parameters for (B) are tabulated in Table A.2.

We conclude that the Papatea fault ruptured anelastically, by which we mean that the highly asymmetric displacements on either side of the fault cannot be fit by elastic dislocation models. We do not consider this the result of a pronounced material contrast across the fault, for which there is no geological evidence [62]. We suggest that the Papatea fault did not release built-up interseismic strain energy as is conventionally assumed. Instead, the exceedingly large uplift of the Papatea block was forced by neighboring, elastic fault ruptures, introducing a space problem within the major step-over in the Kaikōura earthquake (Figure 3.11).

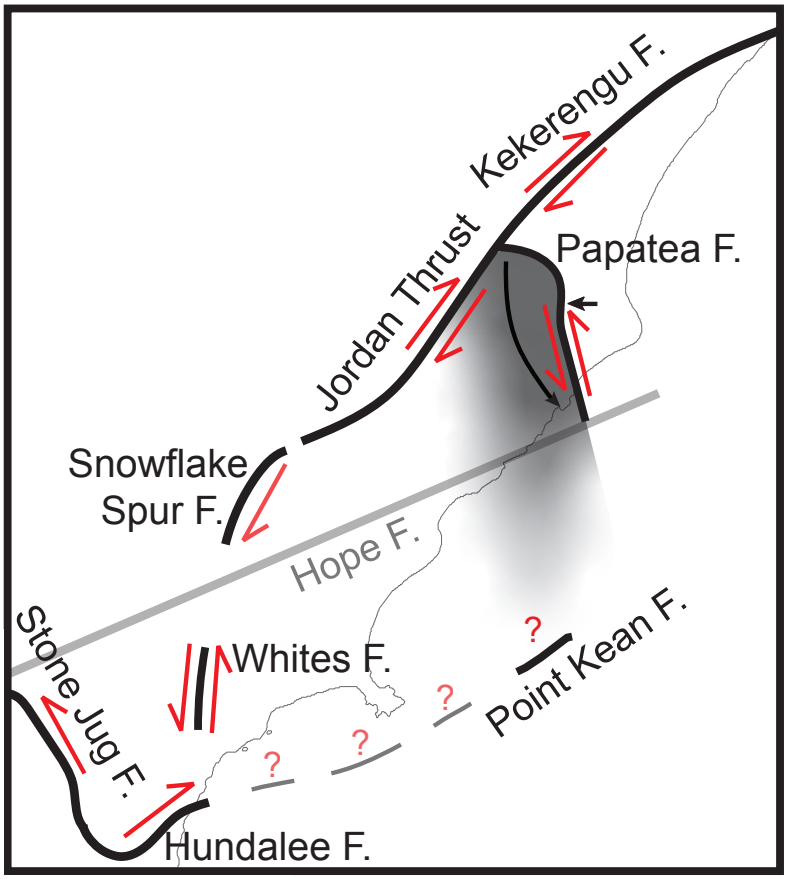


Figure 3.11: Schematic diagram of the Papatea block and neighboring ruptures within the large step-over of the Kaikōura earthquake. Solid black lines indicate approximate mapped faults [61, 62, 73]. Dashed gray lines indicate possible fault rupture locations [17]. The black arrows near the Papatea fault demonstrate the observed horizontal displacement directions. The gray shaded region represents the area of large vertical uplift that was forced to "pop up" during the earthquake due to a localized space problem caused by neighboring ruptures.

A broader implication is that in certain circumstances, dynamic earthquakes can activate faults without apparent accumulated strain energy. This supports inferences that creeping fault segments, which like the Papatea fault lack stored strain, may sometimes rupture co- seismically, under the influence of an approaching high-energy earthquake [84]. Ruptures such as these may also explain why some faults exhibit low geodetic strain accumulation rates but much larger geological slip rates [85]. Therefore, we cannot rely on strain accumulation rates alone as an indicator for rupture potential. This has important implications for seismic hazard because these types of activated ruptures may produce multimeter slip, as the Papatea rupture demonstrates.

## 3.5 Conclusions

We reveal that (i) the Papatea fault twists from moderate dip angles in the south to subvertical in the north, where multimeter vertical slip defies Andersonian fault mechanics, and (ii) its deformation field cannot be fit using elastic models. We suggest that the Papatea fault did not release stored elastic energy in the manner normally assumed, perhaps explaining why the fault appears quiescent in many back-projection models [e.g. [60, 63, 66]]. Instead, these highly unusual kinematics indicate a reactivated structure that slipped anelastically to accommodate strain release from surrounding elastic ruptures during the cascading 2016 Kaikōura earthquake. These results suggest that the common practice of modeling earthquakes as slip on planar faults embedded in an elastic half-space may not always be appropriate. Furthermore, the Papatea rupture demonstrates that faults without stored strain energy still have the potential to generate multimeter slip in large earthquakes.

# Chapter 4

# Mapping Co-seismic Building Damage Using InSAR Coherence in Various Environments

## 4.1 Introduction

InSAR is a widely used method of change detection for tectonic and mass wasting studies [86, 87, 88]. Radar data offers large swath coverage, all weather imaging capability, and low cost satellite acquisitions, such as Sentinel-1, offering revisit times as short as six days. The analysis of temporal interferometric coherence is an emerging tool in emergency response, showing promise as a valuable method of detecting structural damage caused by an earthquake [88]. This method maps areas of small scale phase decorrelation from damaged structures within radar images. When compared to a pre-seismic coherence image, these regions of co-seismic decorrelation emphasize damaged buildings. This method does not require full building collapse and may be able to detect lower levels of structural damage, unlike methods that use radar amplitude correlation, which can be used, often in combination with interferometric phase, to map regions of collapse from temporal changes in building back-scatter strength (eg. refs. [89, 90, 91]).

Processing methods of coherence change mapping and the sensitivity of this method to different levels of damage vary widely. Additionally, few papers compare earthquake-induced coherence change maps to other case study earthquakes and are unclear about how their methodologies would perform in different regions. This study compares four earthquake-damaged case studies using the same InSAR processing methodology with C-band Sentinel-

1 radar imagery to examine the influences of environmental and urban characteristics on coherence mapping. Additionally, I test for consistencies in coherence change values among damage levels in various environments to determine if there are thresholds or ranges of coherence change that can be used to distinguish levels of damage.

## 4.2 InSAR Coherence

This study focuses on interferometric correlation measurements, which measure the coherence of the synthetic aperture radar return signals. The phase information from the two radar acquisitions is used to determine the differences in sensor to target distances between acquisitions. The return echos contain the number of phase cycle oscillations from the distance from sensor to ground plus the phase from scattering within the resolution cell [40]. Two signals will be coherent if their interactions with a target are very similar [92]. The coherence between acquisitions is dependent on the degree of similarity of signals, also known as the magnitude of the cross correlation of two co-registered complex-valued SLCs. Interferometric coherence ($\gamma$) is calculated by:

$$\gamma = \frac{E\left(S_p S_s^*\right)}{\sqrt{E\left(S_p S_p^*\right) E\left(S_s S_s^*\right)}} \tag{1}$$

where $S_p$ and $S_s$ are the co-registered primary and secondary images, the star (*) denotes the complex conjugate, and the E is the expected value [40, 93]. Given that a single pixel signal is the combination of many individual echos from many scatterers within a resolution cell, the phase from a single pixel is a stochastic variable [40, 94]. Equation (1) can be calculated for each individual pixel in the image, where the expected value is the sum of all possible values from a random variable. Ideally, the expected value would be calculated from multiple observations of each pixel over time [9, 40]. However, only one observation from each acquisition is obtained, so the expected value is simulated using a spatial average from a small window of pixels in the image [9, 94]. In practice, Equation (1) becomes:

$$\gamma = \frac{\left\langle S_p S_S^* \right\rangle}{\sqrt{\left\langle S_p S_p^* \right\rangle \left\langle S_s S_s^* \right\rangle}} \tag{2}$$

The pointy brackets denote that coherence is calculated locally over a small window of

samples (pixels) [93]. This window moves through the image to estimate coherence of the entire radar product. Here, the larger the window size, the better the coherence estimation. However, there is a trade off between spatial resolution and coherence window size, where the larger the window size, the lower the spatial resolution [9]. Equation (2) uses a maximum likelihood estimator to find the most probable estimation of coherence from the pixels within the defined window. This method is used because it is able to estimate coherence from a set of individual stochastic samples [93].

Interferometric coherence is calculated using a correlation function, so the terms "correlation" and "coherence" are considered synonymous, although there are slight differences in detail between the two. Thus, the term "decorrelation" is used to describe reduced coherence. Estimating InSAR coherence is a way to assess the quality of the interferogram. An interferogram with high coherence will result in successful interferogram formation and will have fewer unwrapping errors when summing individual fringes to calculate total LOS displacement. Decorrelation can be caused by several factors and results in noise in an interferogram, making interpretation difficult [40, 93].

### 4.2.1 Sources of Decorrelation

For repeat-pass interferometry, the two radar acquisitions would ideally be from the exact same position in space. However, the antenna positions never line up perfectly, which introduces decorrelation due to slightly different imaging geometries. The distance between the two antenna positions in space is known as the spatial baseline, which has a horizontal and vertical component (see Figure 4.1). The decorrelation from large parallel baselines (the vertical component of the spatial baseline, parallel to the look direction of the sensor) is negligible compared to the perpendicular baseline (the horizontal component, perpendicular to the look direction of the sensor) [40]. When choosing images for radar interferometry, the perpendicular baseline should be minimized to reduce the phase changes caused by slightly different viewing positions in space (spatial decorrelation) [86, 95, 92].

Several other sources of decorrelation can be addressed through careful image choice and processing. Chosen radar images should be acquired by sensors with the same system parameters to reduce phase changes induced by different viewing geometries (geometric decorrelation) [92]. For example, very different incidence angles from different types of sensor would cause decorrelation. Further, decorrelation may be caused by image processing errors, like mis-registration of primary and secondary images or from thermal noise within the sensor itself [86, 97]. Additionally, a steep phase gradient can introduce decorrelation.

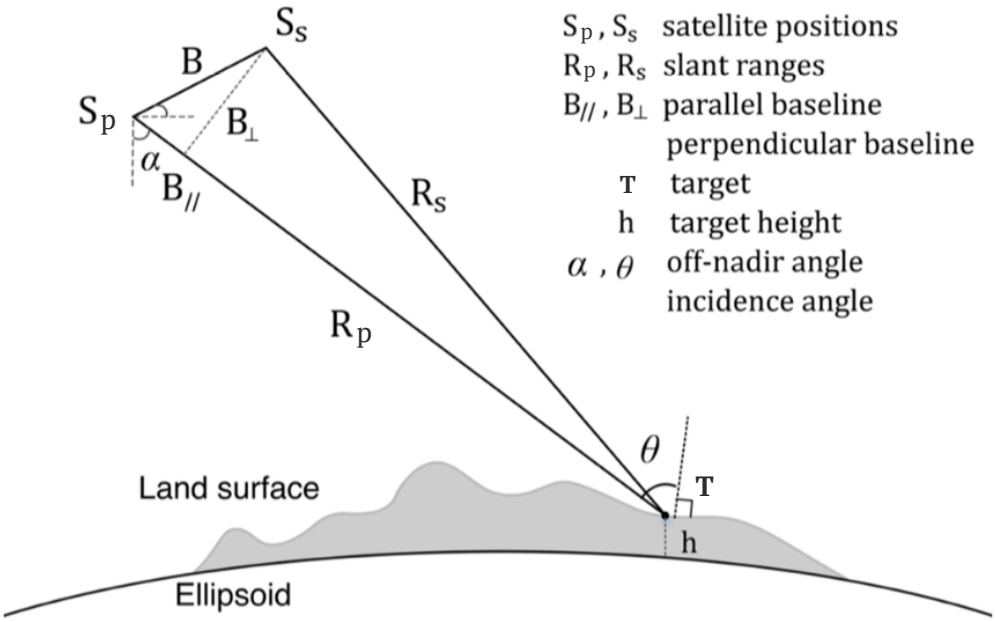


Figure 4.1: Schematic diagram of the viewing geometry of repeat-pass SAR interferometry. $S_p$ and $S_s$ are the primary and secondary acquisitions, respectively. B represents the total spatial baseline, with perpendicular ($B_\perp$) and parallel ($B_{//}$) components. $R_p$ and $R_s$ are the slant-range distances from the sensors (at some height, h, above the ellipsoid) to ground target (T) for the primary and secondary acquisitions. The look direction of the sensors can be determined by the off-nadir angle ($\alpha$) or the incidence angle ($\theta$) [96].

The wavelength of the radar system controls the amount of displacement corresponding to each fringe. When the fringe frequency exceeds the spatial resolution of the image, individual fringes cannot be discerned, causing coherence loss in an interferogram. For example, the amount of ground deformation is usually greatest near a surface rupture, which causes a steep phase gradient that can exceed the imaging capabilities of the radar near the rupture [40]. Additionally, areas of steep topography can cause reduced coherence, with the effects of foreshortening and layover [86, 98].

Reduced signal coherence between the time of radar acquisitions caused by physical disruptions are known as temporal decorrelation [40, 92]. Temporal changes, like seasonal changes, are directly related to the amount of time between acquisition dates (the temporal baseline). When using InSAR to map co-seismic ground displacement, the temporal baseline should be small to minimize the decorrelation from natural temporal changes [40].

Volumetric decorrelation is a type of temporal decorrelation caused by volumetric scattering from vegetation. This is from phase changes due to vegetation growth over time and

from vegetation shape change from influences like wind. To isolate the co-seismic phase shift, sources of volumetric decorrelation may be masked out of the interferogram. This is addressed differently depending on the application of the interferogram [87, 99]. For example, classification of pixels within the interferogram containing vegetation may done using optical imagery and excluded from analysis [100] or 'noisy' fringes caused by low coherence that could not be unwrapped may be removed entirely using a coherence threshold [99, 101].

### 4.2.2 Coherence Mapping for Building Damage

Efficient identification of damaged structures following an earthquake is essential for life safety. Using remote sensing, damage assessments and monitoring over large areas and in high risk regions can be conducted where field surveys may not be possible or feasible. Reliable, automatically acquired satellite data can assess damage in remote regions and in areas where there are damaged lines of communication to governments agencies. In cases where initial damage estimations are based on reported damage, affected areas unable to communicate the severity of damage may not be included in damage estimations until ground surveys are conducted. This can lead to delayed declarations of emergency and requests for external help.

Organizations like Copernicus Emergency Management Services [102], the United Nations Institute for Training and Research (UNITAR) Operational Satellite Applications Programme (UNOSAT) [103], and the International Charter of Space and Major Disasters [104] aim to rapidly publish hazard and damage maps online and rely heavily on optical satellite imagery. These organizations automatically acquire and download data when activated by government authorities and manually analyze structural damage. However, optical satellites cannot image through smog, ash, or clouds because they are passive, shorter wavelength systems that rely on sunlight for illumination [105]. Moreover, optical satellites are often nadir-looking, which fails to image structural damage to sides of buildings. When using these nadir-looking sensors, collapsed buildings with intact roofs may also be difficult to identify due to the lack of acquired height information, resulting in possible mis-classification of damage [86, 106].

Active SAR satellites use a slant-range viewing geometry to capture co-seismic phase shifts caused by damaged structures. Many studies that use phase coherence to map building damage calculate the coherence change between a pre-seismic and co-seismic coherence map, to emphasize the regions of decorrelation caused by the earthquake. For example, in a pre-seismic coherence map, vegetated areas will appear decorrelated while built areas will return

a coherent signal from the lack of disturbance to the structures. A co-seismic coherence map captures the decorrelation from vegetation as well as from damaged structures. At the same time, undamaged buildings will still return a strong, coherent signal. Thus, to differentiate between naturally decorrelated targets and co-seismically damaged structures, the coherence change is often calculated [86]. Other sources of decorrelation must be minimized when choosing radar imagery and during processing for both the pre- and co-seismic image pairs for optimal, accurate results.

The ARIA (Advance Rapid Imaging and Analysis) project is a joint collaboration between Caltech and NASA's Jet Propulsion Laboratory (JPL) that produces products from radar imagery to assist in understanding and assessing natural hazards, including earthquakes [88]. Damage proxy maps (DPM) are one ARIA product, in which InSAR coherence change maps are used to produce maps of areas of probable damage resulting from a significant earthquake, which are often validated using pre- and post-event optical and aerial image surveys [88]. The ARIA group uses X-, C-, and L-band radar imagery to compare pre- and co-seismic intensities and coherence. Their processing workflow includes automatically downloaded radar imagery followed by manually processed interferograms and coherence maps, where image co-registration is performed using a method called rubber sheeting [107]. Here, the secondary image is distorted to match the distortions in the primary image by registering the secondary image using pixel offsets calculated from the cross correlation of the amplitude images. Then, outliers from calculated relative offsets are removed and interpolated. This method, improves coherence between image acquisitions and smooths the resulting coherence map [88, 107]. Additionally, pixel statistics between the pre- and co-seismic coherence maps are matched after co-registration. The final coherence change map is calculated using a simple difference [88].

Coherence change damage maps have been published for many damaging earthquakes and most of these studies use coherence change thresholds to separate damaged from non-damaged structures. However, the steps to selecting and the value of this threshold vary widely. A study of the 2016 Kumamoto earthquake used GIS and optical imagery, along with coherence mapping to determine coherence change thresholds of 0.2–0.4 for slightly damaged buildings, 0.4–0.6 for higher damaged buildings, and 0.6–1 for heavily damaged or destroyed structures [100]. Another study of the Kumamoto earthquake found a coherence decrease of greater than 0.3 corresponded to high levels of damage [108]. A study of the damage from the 1999 Kocaeli, Turkey earthquake used a coherence difference threshold of 0.35 to distinguish non-damaged buildings from damaged structures [109]. A normalized difference coherence change range of 0.1-0.3 was sufficient to detect damage from the 2015 Gorkha earthquake

[110]. Following the 2016 Amatrice earthquake, a normalized difference coherence change minimum value of 0.2 was used to define collapsed buildings [111] while another study found a mean of 0.33 corresponded to collapsed buildings [112]. A study of Sarpol-e-Zahab, Iran following the 2017 earthquake found an average coherence loss in urban areas of $\geq 0.1$ [113]. Therefore, although this method has not yet become standard practice for rapid emergency response, it is evident that coherence change mapping can be a useful, effective tool for mapping structural damage. However, there is not one global coherence change threshold or methodology that is applied to map earthquake-induced structural damage [114, 108].

There are few coherence damage mapping studies that compare coherence change maps across multiple earthquakes, with many published values and processes highly specific to certain areas. Our study explores the variability of coherence change values that correspond to levels of building damage from four case study regions, each with different environmental and urban characteristics. Using the same processing methods, I compare the coherence change outcomes across damage levels of four different damaged regions. I test for coherence change values that can be applied to distinguish damage.

## 4.3 Case Study Background

The following case studies were chosen based on a number of factors, including the availability of both Sentinel-1 and damage surveyed data, environmental and urban characteristics, and damage pattern. It should be noted that the method of collection and type of the surveyed data varied among the four cases (see Section 4.4). Additionally, the timing of the coverage of Sentinel-1 data for each case study (see Table 4.1) would not be ideal if the goal of this study was to identify highly damaged areas for life safety. For example, the post-seismic radar acquisition should be within zero to five days of the earthquake to use this method of damage mapping for rescue of individuals trapped in debris or a damaged building. However, this exploratory study aimed to improve future implementation of this method and radar data were chosen based on factors other than life safety.

### 4.3.1 2016 Amatrice Earthquake

On August 24, 2016 at 1:36 (UTC), the first earthquake of the Central Italy earthquake series struck ∼10 km SE of Norcia at ∼8 km depth [115], causing significant damage to Amatrice and the surrounding region. This $M_w$ 6.0 rupture was caused by normal faulting in the Mt. Vettore–Mt. Bove and Laga Mtns. fault systems in the Central Apennine mountain

range [116, 117, 118]. This region is characterized by extensional NNW-SSE trending normal faults (mainly dipping west) [119, 120]. Slip models of the Amatrice earthquake suggest the rupture occurred within a step-over between the two fault systems (eg. refs. [118, 117, 116]). Two months after this event, two more normal-faulting mainshocks occurred on October 26 ($M_w$ 5.9) and October 30 ($M_w$ 6.5) within this same tectonic setting. Each event caused significant damage to several towns in Central Italy, however this study focuses on the damage to Amatrice caused by the first earthquake of this series, due to the town's larger size and unique damage pattern. Although Amatrice was further damaged in the following events of the Central Italy sequence, only damage from the August event was used in this study to avoid the effects of compound damage in the coherence maps.

Amatrice experienced peak ground accelerations of 0.66 g during the August mainshock and a total of 234 fatalities. This was the highest recorded ground motion for villages and towns in the Central Italy region. Ground motion in Amatrice during the October events were weaker at 0.08 g and 0.50 g. Extensive damage occurred to structures in the western historical region of Amatrice due to their construction material (mainly unreinforced masonry) and age, with some structures as old as the 16th–18th century [121]. The eastern residential region of Amatrice had newer buildings, constructed with reinforced concrete, and overall sustained less damage [121, 118]. Field studies revealed mainly non-structural damage to concrete buildings and severe structural damage to masonry style buildings and an overall lack of site amplification effects [121, 118].

### 4.3.2 2017 Puebla–Morelos Earthquake

A $M_w$ 7.1 earthquake struck near the border of Puebla and Morelos (Mexico) on September 19, 2017 at 18:14 (UTC). Although the epicenter was ∼120 km SE of Mexico City, this was the most intense earthquake felt by the city since the $M_w$ 8.1 Michoacán earthquake that occurred on the same day, 32 years earlier [122, 123]. The 2017 event was caused by normal faulting at an intermediate depth of ∼50 km within the Cocos plate, which is being subducted below the North American plate at ∼76 mm/yr [124]. This earthquake was preceded by another intraplate, intermediate depth (∼58 km) event that hit offshore Chiapas, Mexico (∼650 km SE of Puebla). However, this earlier $M_w$ 8.1 earthquake likely did not directly cause the event on September 19. Instead, these events are believed to be part of a pattern of normal faulting, intraplate earthquakes that have been repeating over the past several decades, with pairings of earthquakes occurring within months to decades of each other [125, 126]. Although both September earthquakes were damaging, only the

Puebla–Morelos event caused damage to Mexico City, which is the focus of this case study.

Central Mexico City is built on soft, lacustrine sediments from the drained and extracted Texcoco and Xochimilco-Chalco Lakes, which caused soil amplification of seismic waves, increasing ground motion. Structures with periods of 0.8-1.5 seconds (five to eight stories high) were damaged and fell within sediment zones with natural periods of 0.8-1.5 seconds [127]. This effect was caused by resonance, which occurs when the natural period of vibration of the soil and the structure are the same. As a result, over 40 structures fully collapsed, with adobe and unreinforced masonry buildings performing the worst. Additionally, 350 casualties across Mexico City, Puebla and Morelos were recorded as a result of this event [127].

### 4.3.3 2017 Sarpol-e-Zahab Earthquake

A $M_w$ 7.3 earthquake struck near the Iran-Iraq border on November 12, 2017 at 18:18 (UTC) at ∼19 km depth. The epicenter was located ∼5 km north of Ezgeleh (Kermanshah Province, Iran) within the Zagros Mountains [128, 129]. Here, the Arabian and Eurasian plates converge at a rate of ∼20-30 mm/yr, causing folding and faulting within the collision zone [128, 130]. Within this tectonic setting, the earthquake was caused by mid-crustal oblique-reverse faulting. Shaking was felt south of the epicenter, in the Iranian provinces of Kermansha, Kudistan, Ilam and West Azarbaijan, causing landsliding, liquefaction, rock falls and structural damage to several counties and villages [131, 132]. However, no damage was reported in towns north of the epicenter, congruent with the southward rupture directivity. Reinforced concrete, confined masonry, steel, stone, and adobe (mainly used in villages) structures sustained damage. As a result, over 600 fatalities were reported, thousands were injured, and ∼15,000 people were left homeless [131, 133]. Koeeke Hasan, Koeeke Aziz, Koeeke Mahmod, and Koeeke Majid, villages within Kermanshah Province, Iran, suffered extensive damage to mainly adobe and stone structures [131, 134]. This study focused on damage to these villages, although other damage mapping coherence studies have been conducted for Sarpol-e-Zahab; a larger city ∼50 km south of the epicenter (eg. refs. [111, 113]).

### 4.3.4 2018 Anchorage Earthquake

On November 30, 2018, a $M_w$ 7.1 earthquake occurred at ∼47 km depth, 14 km NW of Anchorage at 17:29 (UTC) [135]. 150 km SE of this location, the Pacific plate subducts below the North American plate (∼57 mm/yr) within the Alaska–Aleutian subduction zone.

This earthquake occurred due to normal faulting within the subducting Pacific plate. Given the close proximity to the largest city in Alaska, shaking was felt by over half the state's population. This earthquake had the greatest societal impact in this area since the 1964 $M_w$ 9.2 Great Alaska earthquake [136]. Peak ground acceleration was highest in midtown Anchorage at 0.474 g [137]. There were over 200 reports of structural damage, mostly to residential buildings, as well as significant infrastructure damage to roads, the Port of Alaska, and railways. Reported damage was from the city of Anchorage and several neighbouring cities including Palmer, Big Lake, and Wasilla. However, implementation of modern building codes in Alaska held up well against structural collapse, with a total of only three structures reported as fully destroyed and no fatalities [137].

## 4.4 Methodology, Processing, and Data

To map co-seismic building damage using InSAR coherence, pre- and co-seismic coherence maps are first created from a pre- and co-seismic interferogram. These two interferograms are made from three radar images; two before the earthquake and one after [86]. Then, the pre-seismic and co-seismic coherence maps (each with coherence values from 0 to 1) are differenced to create a coherence change map (with values from -1 to 1). In the pre- and co-seismic coherence images, pixels with values close to 0 indicate areas of low coherence, while values close to 1 indicate areas of high coherence between acquisitions. A coherence change map captures the co-seismic damage where pixels of high co-seismic decorrelation have a value close to 1, while pixels that became more coherent during an earthquake will have values close to -1. The coherence change map is calculated from a normalized difference ($\mathrm{ND}_\gamma$):

$$ND_\gamma = \frac{\gamma_{pre} - \gamma_{co}}{\gamma_{pre} + \gamma_{co}} \tag{3}$$

where $\gamma_{pre}$ is the pre-seismic coherence map and $\gamma_{co}$ is the co-seismic coherence map [86]. This method of calculating coherence change is widely accepted because it is more sensitive to small changes in coherence and physical changes on Earth's surface than a simple difference (eg. refs. [100, 138, 90, 86]) (see Figure A.1C and D).

For each case study, three C-band SLCs along with a 30 m DEM (SRTM and ALOS-2) [139, 140] covering the study area were collected. Sentinel-1 SAR data [141] were used because it is freely available with a revisit time as short as 6 days. Temporal baselines were kept to 12 days or shorter, with 6 day interferograms used where available. Sentinel-1A

and -1B fly along the same orbital plane and have identical imaging systems, minimizing the effect of geometric decorrelation. Additionally, perpendicular baselines of each pair were kept under 100 m to reduce the effect of spatial decorrelation [86]. For each case study, the three VV polarized SLCs were co-registered to a common primary image (the second pre-seismic acquisition) to ensure pixels of the pre- and co-seismic coherence maps were registered in the same way, making the pixels in both coherence maps comparable. VV polarization was chosen because it has been found to be more sensitive to physical disturbances to buildings than cross polarized images and is considered optimal for coherence change analysis [112]. Table 4.1 summarizes the acquisition and baseline information for each earthquake, with incidence angles calculated from center points of overlapping portions of primary and secondary images.

Table 4.1: Viewing geometry, perpendicular baselines, and time intervals of InSAR data. All VV polarized SAR SLCs were acquired by the C-band, right-looking, Sentinel-1 constellation, where S1A and S1B are the -1A and -1B satellites [141].

| Pair | Primary-Secondary | Perp. Baseline (m) | Incidence Angle | Track | Time (days) |
|---|---|---|---|---|---|
| *Amatrice Earthquake (2016/08/24)* | | | | | |
| pre-seismic | 2016/08/21 (S1A) - 2016/08/09 (S1A) | -83.385 | 41.551° | Desc. | 12 |
| co-seismic | 2016/08/21 (S1A) - 2016/09/02 (S1A) | -51.592 | | | 12 |
| *Puebla-Morelos Earthquake (2017/09/19)* | | | | | |
| pre-seismic | 2017/09/17 (S1A) - 2017/09/11 (S1B) | -39.814 | 43.967° | Desc. | 6 |
| co-seismic | 2017/09/17 (S1A) - 2017/09/23 (S1B) | 8.664 | | | 6 |
| *Sarpol-e-Zahab Earthquake (2017/11/12)* | | | | | |
| pre-seismic | 2017/11/11 (S1A) - 2017/10/30 (S1A) | -39.936 | 41.598° | Asc. | 12 |
| co-seismic | 2017/11/11 (S1A) - 2017/11/23 (S1A) | -32.655 | | | 12 |
| *Anchorage Earthquake (2018/11/30)* | | | | | |
| pre-seismic | 2018/11/22 (S1A) - 2018/11/10 (S1A) | 3.190 | 36.614° | Desc. | 12 |
| co-seismic | 2018/11/22 (S1A) - 2018/12/04 (S1A) | 11.660 | | | 12 |

The radar data were processed using GAMMA [142] and were multi-looked to 4:1 (range: azimuth) to reduce the phase noise and to make square ∼20×20 m pixels. A coherence estimation window of $3 \times 3$ pixels was used, resulting in a resolution of ∼60×60 m. Typically, coherence mapping studies for damage assessment use a coherence change window of either $5 \times 5$ or $3 \times 3$ (eg. refs. [87, 88, 91, 108]). After testing, a $3 \times 3$ pixel window was more sensitive to coherence changes between pixels (see Figure A.2) and preserved spatial resolution. Testing of triangular, linear, and Gaussian weighting functions in the coherence estimation was also performed. A triangular weighting function was found to be the most favorable [87], although there was little difference across the three weighting functions. For the triangular

weighting function, the center window pixel is given highest weight in Equation (2) and the weights of surrounding pixels linearly decrease outward (see Figure 4.2).

| | | |
|---|---|---|
| 0.293 | 0.5 | 0.293 |
| 0.5 | **1** | 0.5 |
| 0.293 | 0.5 | 0.293 |

Figure 4.2: Pixel weights used to calculate coherence as shown in Equation (2) with a 3×3 coherence estimation window. The bold, center pixel had the highest weight (1). Surrounding pixel weights decrease linearly outward from the center pixel.

In the slanted viewing geometry of SAR imagery, one geometric distortion that occurs is the compression of near range targets closer to the sensor relative to targets farther away [4]. The true horizontal ground distances are not represented by pixels in slant-range geometry. In ground-range geometry, ground targets in the radar image are in their proper geometric shapes with correct planimetric (x, y) positions. The process of geocoding converts pixels from slant-range geometry to ground-range geometry [4]. All pre- and co-seismic coherence maps were geocoded to convert pixels from slant-range to ground-range geometry before calculating the normalized difference. During this step, slant-range coherence pixels were interpolated using cubic spline interpolation to match the resolution of the DEM used for processing. The input DEMs used in processing had a resolution similar to the radar resolution to accurately simulate and remove the topographic phase. To check this, the effect of the DEM resolution on the geocoded coherence map was tested using 90 m, 45 m, 30 m, and 15 m DEMs. The coherence maps created with 30 m and 15 m DEMs looked nearly identical. The coherence maps created from DEMs with resolution lower than 30 m had patches of no data, indicating the topographic phase was not simulated correctly. Thus, final geocoded coherence pixels had a resolution of $\sim 30\times30$ m to match the input DEMs.

Surveyed damage data were used to compare coherence change values to surveyed damage levels after each earthquake. For the Amatrice earthquake, the surveyed damage data were sourced from analysis of pre- (2014) and post-event (August 25, 2016) aerial imagery (50 cm resolution [102]) by Copernicus Emergency Mapping Services (CEMS) (see Figure 4.3). These data were classified into four damage levels: none to slight, moderate, heavy,

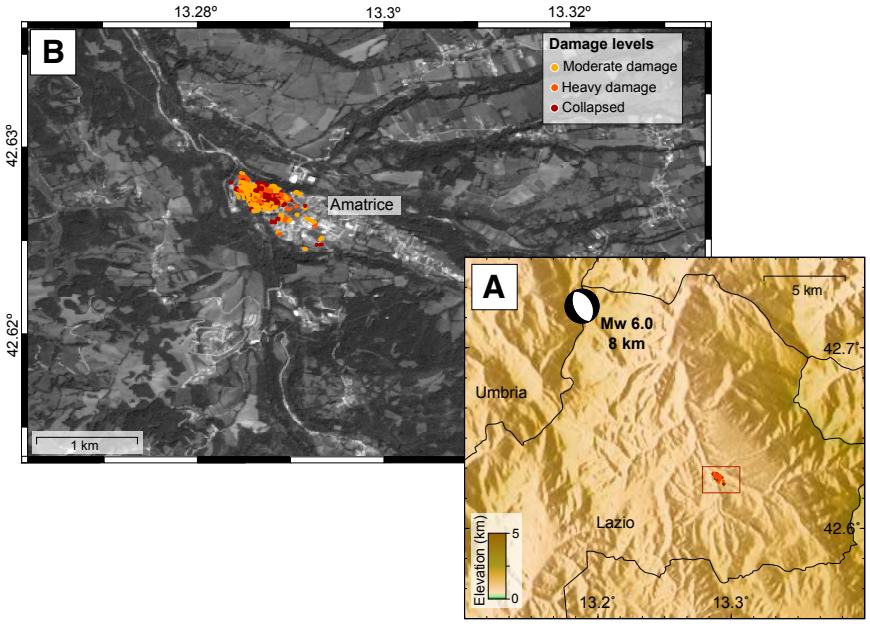


Figure 4.3: Map of building damage in Amatrice, Italy, following the 2016 Amatrice earthquake. (A) Regional map of Central Italy, with moment tensor solution plotted at the epicentral location [115]. (B) Surveyed building damage in Amatrice by Copernicus Emergency Mapping Services from analysis of 50 cm pre- and post-event aerial imagery [102].

and collapsed. Although field surveys were conducted [118, 121, 143], they were largely restricted to lower damaged areas due to unsafe conditions from unstable highly damaged buildings in the western, historical region of Amatrice. Therefore, published field surveys did not include the full extent of damage. However, discrepancies between field and aerial surveyed building damage were found [121, 144]. Low damage levels categorized by CEMS (none to slight category) had inconsistencies with field surveys, where the damage level was usually higher than assigned by CEMS. Higher damage levels assigned by CEMS were more consistent with field surveyed damage levels [121, 144]. Damage level discrepancies were due to the nadir-viewing geometry of the aerial imagery, causing mis-classification. This was especially the case where a highly damaged structure's roof remained intact, where significant damage occurred on the sides of the building, where there was extensive cracking, or where significant damage occurred inside the building [86, 121, 145]. Due to these discrepancies, the none to slight damage category (a total of 23 records) in the CEMS damage data set was excluded from analysis.

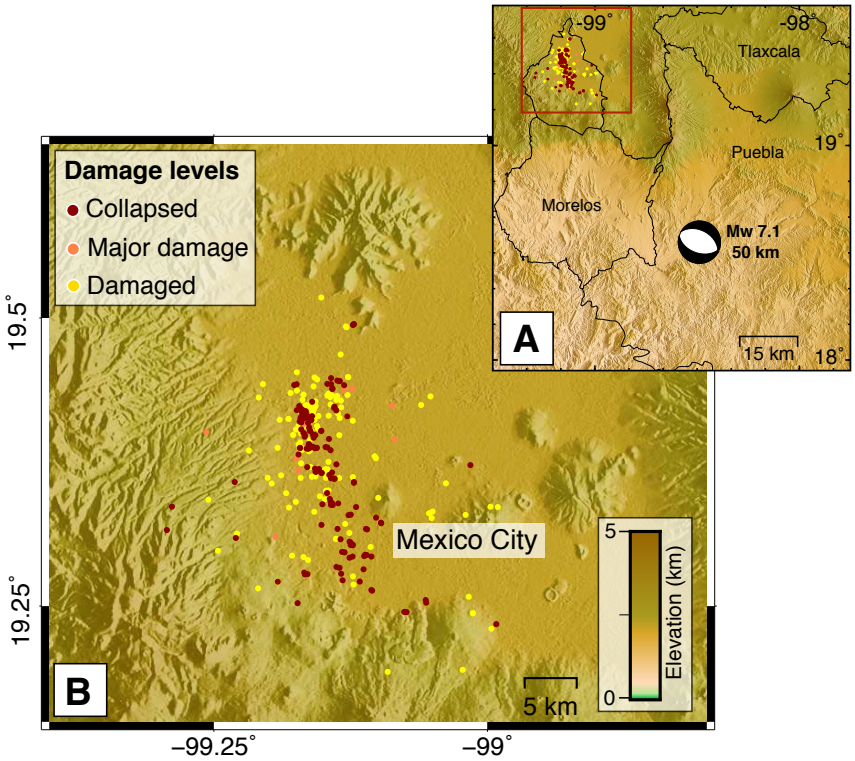


Figure 4.4: Map of building damage in Mexico City following the 2017 Puebla–Morelos earthquake. (A) Regional map of southern Mexico, with moment tensor solution plotted at the epicentral location [124]. (B) Surveyed building damage in Mexico City conducted by the Geotechnical Extreme Events Reconnaissance [127] Association and Universidad Nacional Autónoma de México [146].

The surveyed damage data for Mexico City following the Puebla–Morelos earthquake were sourced from field surveys conducted by the Geotechnical Extreme Events Reconnaissance (GEER) [127] Association and Universidad Nacional Autónoma de México (UNAM) [146] (see Figure 4.4). This data was collected by foot and aerial imagery and is separated into three damage categories: damage, major damage, and collapsed as shown in Figure 4.4.

Coordinates of surveyed damage to Iranian villages and towns following the Sarpol-e-Zahab earthquake were not available. Damage assessments were conducted by UNITAR [134] from pre- (July 24, 2017, 50 cm Pleiades-1A) and post-event (November 16, 2017, 30 cm WorldView–3) optical imagery of the several Kermanshah villages (see Figure 4.5). At the time of writing, the UNITAR data set has not been validated with field surveyed data. Therefore, the damage assessment by UNITAR only contains one damage level: possible damage.

Following the 2018 Anchorage earthquake, field surveyed and validated self-reported damages were complied by the Mat-Su Borough Department of Emergency Services (see Figure 4.6). This data set contains five damage levels: not affected, affected, minor damage, major damage, and destroyed [137].

Surveyed damage data was available in building polygon format for Amatrice and as point data for the other three case study areas. The point data were buffered to create polygons around the points to improve accuracy of damage regions to compare to coherence change pixels. In order for the damage polygons to be representative of the sizes of damaged buildings, building footprints of damaged structures were measured in Google Earth to determine suitable buffer sizes. After testing, a 12.5 m buffer radius was used for damage points in Mexico City, a 8 m buffer radius was used for damage coordinates in the Kermanshah villages, and a 12.5 m buffer was used for damage points in the Anchorage area. After buffering, point geometries became polygon geometries and were used to calculate coherence change statistics.

Zonal statistics of coherence change were calculated to find coherence change values that corresponded to surveyed damage polygons and were calculated using the *rasterstats* Python package with module *zonalstats* [147]. This module can calculate zonal statistics based on either pixel center points within given polygons or based on any part of pixels touching or within given polygons. Given the damage polygons were almost always smaller than the resolution of the coherence change pixels, the center point of the coherence change pixels rarely fall within the polygon bounds. Therefore, an average coherence change value was calculated for each polygon based on the number of coherence pixels the polygon intersected.

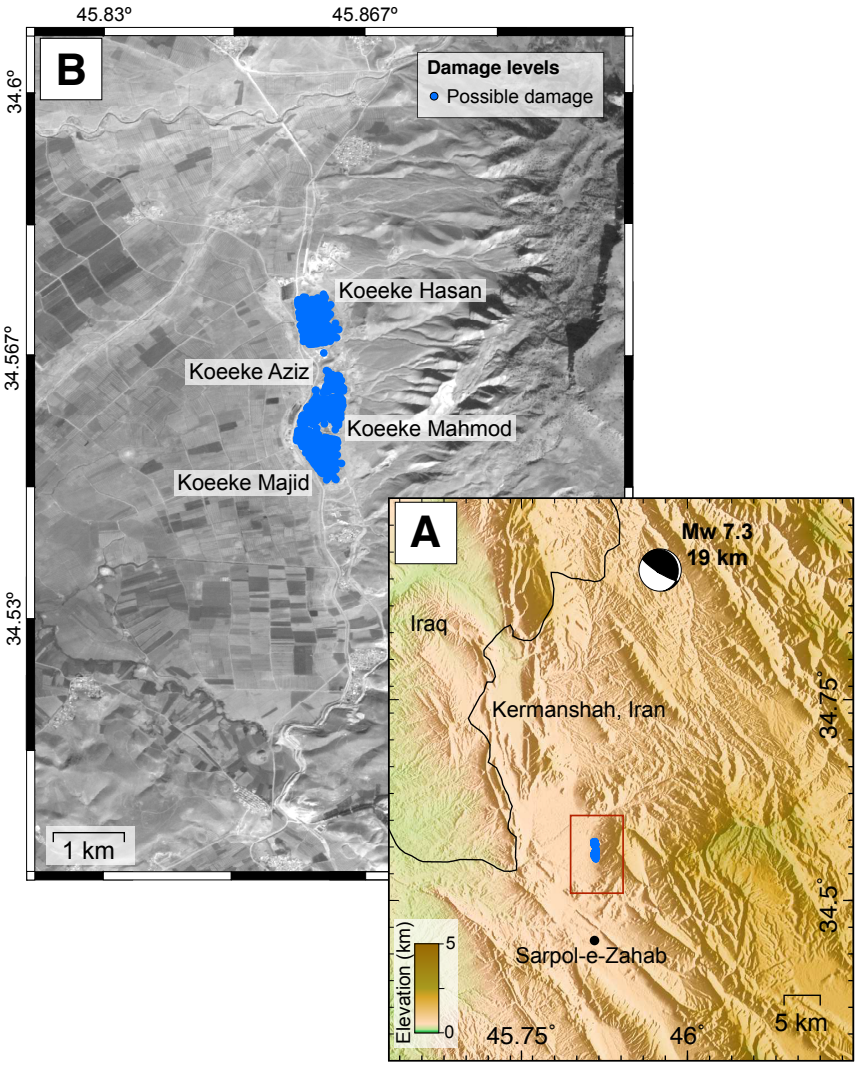


Figure 4.5: Map of building damage in Kermanshah villages, Iran following the 2017 Sarpol-e-Zahab earthquake. (A) Regional map of the Iran–Iraq border, with moment tensor solution plotted at the epicentral location [129]. (B) Surveyed damage in Koeeke Hasan, Koeeke Aziz, Koeeke Mahmod, and Koeeke Majid conducted by the United Nations Institute for Training and Research from analysis of pre-event Pleiades-1A imagery and post-event WorldView–3 imagery [134].

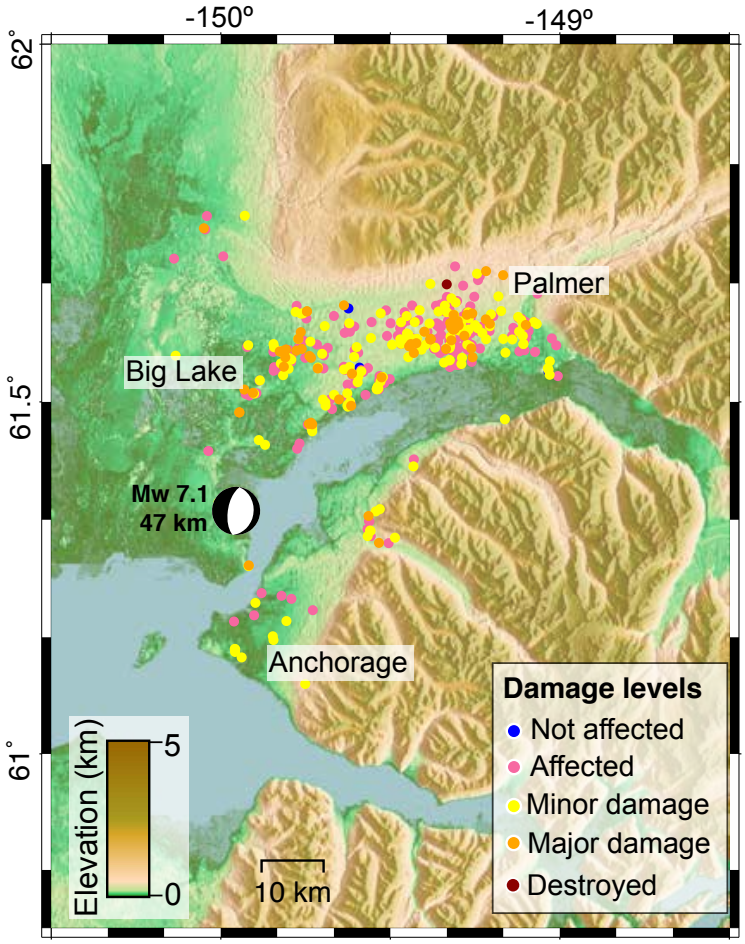


Figure 4.6: Map of surveyed building damage to Anchorage, Alaska and surrounding area following the 2018 Anchorage earthquake. Moment tensor solution plotted at the epicentral location [135]. Plotted damage data are field surveyed and validated self-reported damage, complied by the Mat-Su Borough Department of Emergency Services [137].

## 4.5 Results and Discussion

Two pre- and one post-event C-band SLCs were used to create pre- and co-seismic interferograms (see example in Figure 4.7) and coherence maps for each of the four earthquakes. Figure 4.8 shows the pre-seismic and co-seismic coherence maps, and normalized coherence change maps for Amatrice, Mexico City, the Kermanshah villages, and the Anchorage area.

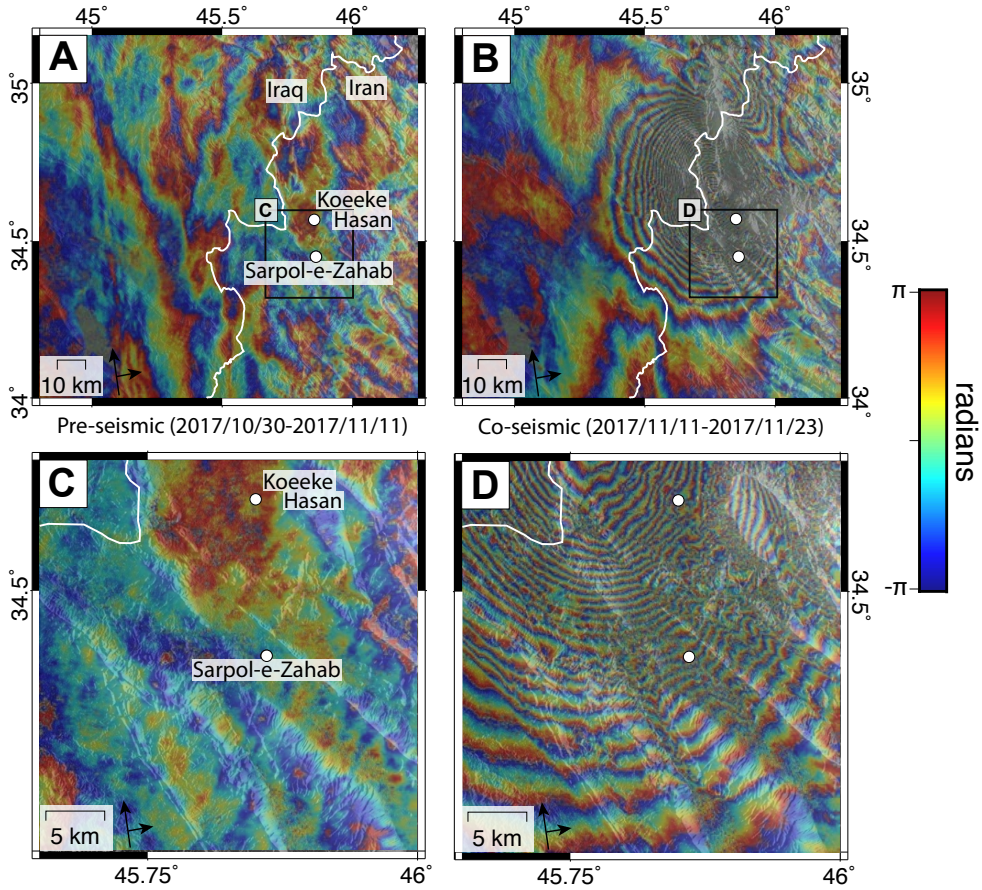


Figure 4.7: Pre-seismic (A, C) and co-seismic (B, D) ascending interferograms for the 2017 Sarpol-e-Zahab earthquake. (C) and (D) show zoomed portions of (A) and (B), respectively, as shown by the black outlined boxes. Line of sight (LOS) directions are indicated by the black arrows in the bottom left corners. Interferometric fringes correspond to the amount of ground displacement in the direction towards or away from the C-band (5.6 cm) Sentinel-1 satellite in the LOS direction.

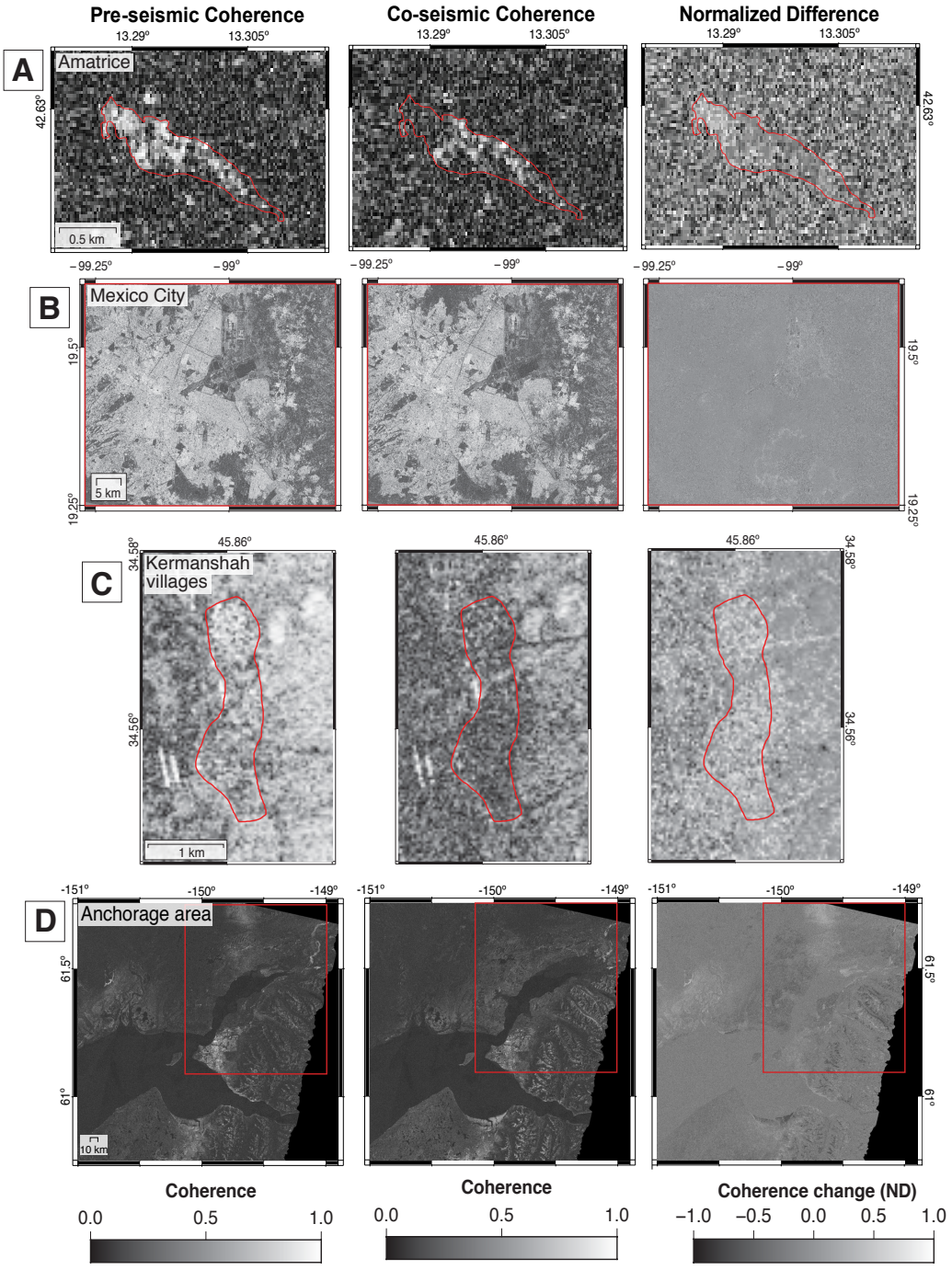


Figure 4.8: Pre-seismic coherence (left), co-seismic coherence (middle), and normalized difference (ND) coherence (right) images for the Amatrice (A, Amatrice), Puebla–Morelos (B, Mexico City), Sarpol-e-Zahab (C, Kermanshah villages), and Anchorage (D, Anchorage and surroundings) earthquakes. Red polygons outline the areas of interest used in this study. Coherence maps were created using a 3×3 coherence estimation window with a triangular weighing function.

Zonal statistics of each building polygon of each data set were computed to find the mean, standard deviation, maximum and minimum mean coherence change values (see Table 4.2). The normalized density distribution of mean coherence change values for each damage level for each earthquake are shown in Figure 4.9. Figure 4.10 shows normalized density distributions of mean coherence change of high damage levels. Figure 4.11 shows the mean coherence change distributions of moderate and majorly damaged buildings.

Table 4.2: Statistics of mean coherence change for each level of structural damage for each case study. Damage levels were from field and satellite surveys following each earthquake. The values below are averages and should be read as average mean coherence change, standard deviation of average mean coherence change, maximum average mean coherence change and so on. The polygon count columns refer to the number of building polygons or buffered points for each damage level in each surveyed data set.

| **Damage level** | **mean** | **std** | **max** | **min** | **polygon count** |
|---|---|---|---|---|---|
| *Amatrice Earthquake* | | | | | |
| Moderate damage | 0.3538 | 0.1889 | 0.7380 | -0.2748 | 137 |
| Heavy damage | 0.3918 | 0.2002 | 0.8667 | -0.5281 | 69 |
| Collapsed | 0.3739 | 0.1829 | 0.8667 | -0.1259 | 98 |
| High damage (heavy damage + collapsed) | 0.3813 | 0.1898 | 0.8667 | -0.5281 | 167 |

| **Damage level** | **mean** | **std** | **max** | **min** | **polygon count** |
|---|---|---|---|---|---|
| *Puebla-Morelos Earthquake* | | | | | |
| Damage | 0.0274 | 0.1148 | 0.4283 | -0.3272 | 147 |
| Major damage | 0.0719 | 0.1199 | 0.2892 | -0.0388 | 10 |
| Collapsed | 0.0558 | 0.1162 | 0.5252 | -0.2390 | 157 |
| High damage (major damage + collapsed) | 0.0568 | 0.1161 | 0.5252 | -0.2390 | 167 |

| **Damage level** | **mean** | **std** | **max** | **min** | **polygon count** |
|---|---|---|---|---|---|
| *Sarpol-e-Zahab Earthquake* | | | | | |
| Possible damage | 0.3234 | 0.1945 | 0.9126 | -0.3755 | 1102 |

| **Damage level** | **mean** | **std** | **max** | **min** | **polygon count** |
|---|---|---|---|---|---|
| *Anchorage Earthquake* | | | | | |
| Not affected | -0.0559 | 0.1334 | 0.0656 | -0.2097 | 4 |
| Affected | -0.0226 | 0.2322 | 0.5528 | -0.6266 | 206 |
| Minor damage | -0.0011 | 0.2323 | 0.6023 | -0.7367 | 159 |
| Major damage | 0.0696 | 0.2620 | 0.7030 | -0.4842 | 61 |
| Destroyed | 0.1755 | | 0.1755 | 0.1755 | 1 |
| High damage (major damage + destroyed) | 0.0713 | 0.2602 | 0.7030 | -0.4842 | 62 |

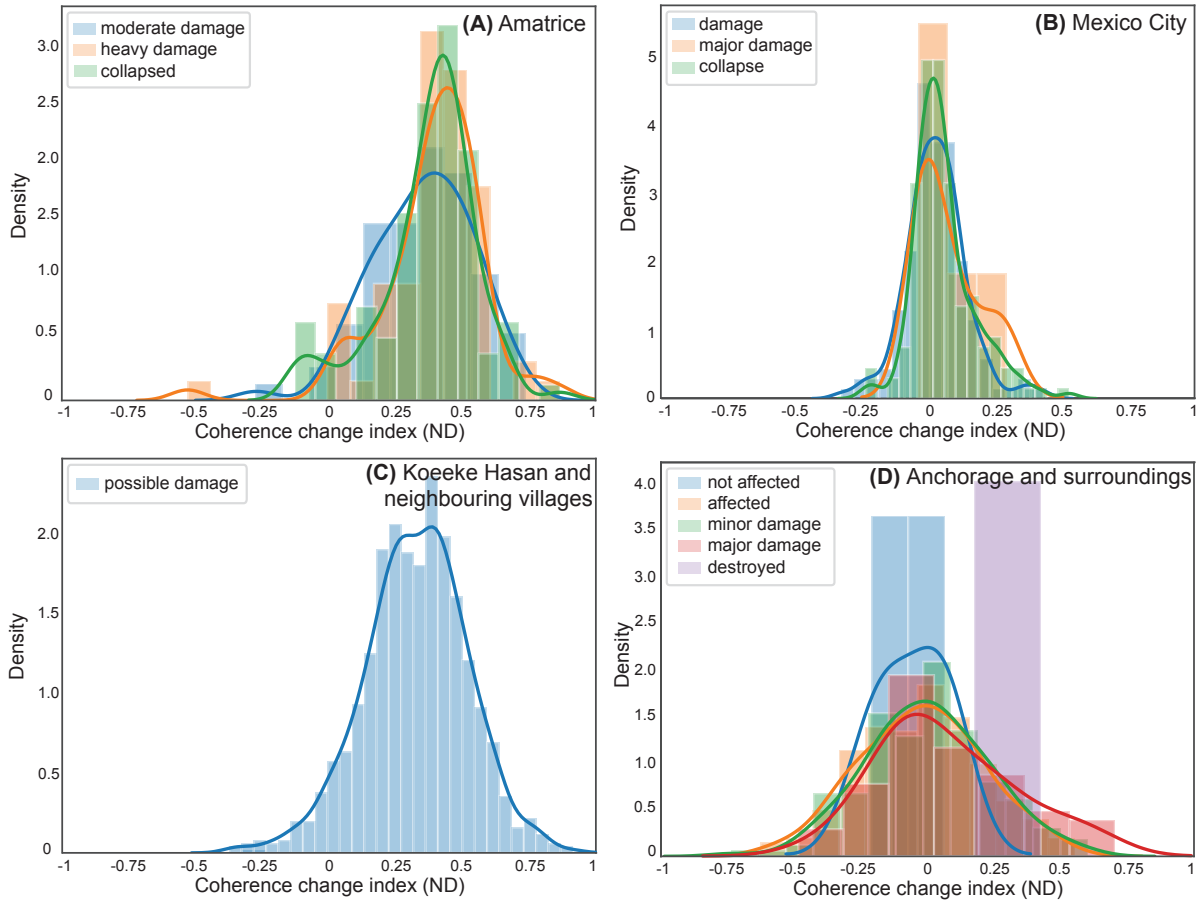


Figure 4.9: Normalized density distribution of mean coherence change (calculated using a normalized difference, ND) for damaged buildings in (A) Amatrice, (B) Mexico City, (C) Kermanshah villages, and (D) the Anchorage area. Distributions are fit with a kernel density estimate, where bin heights reflect probability densities.

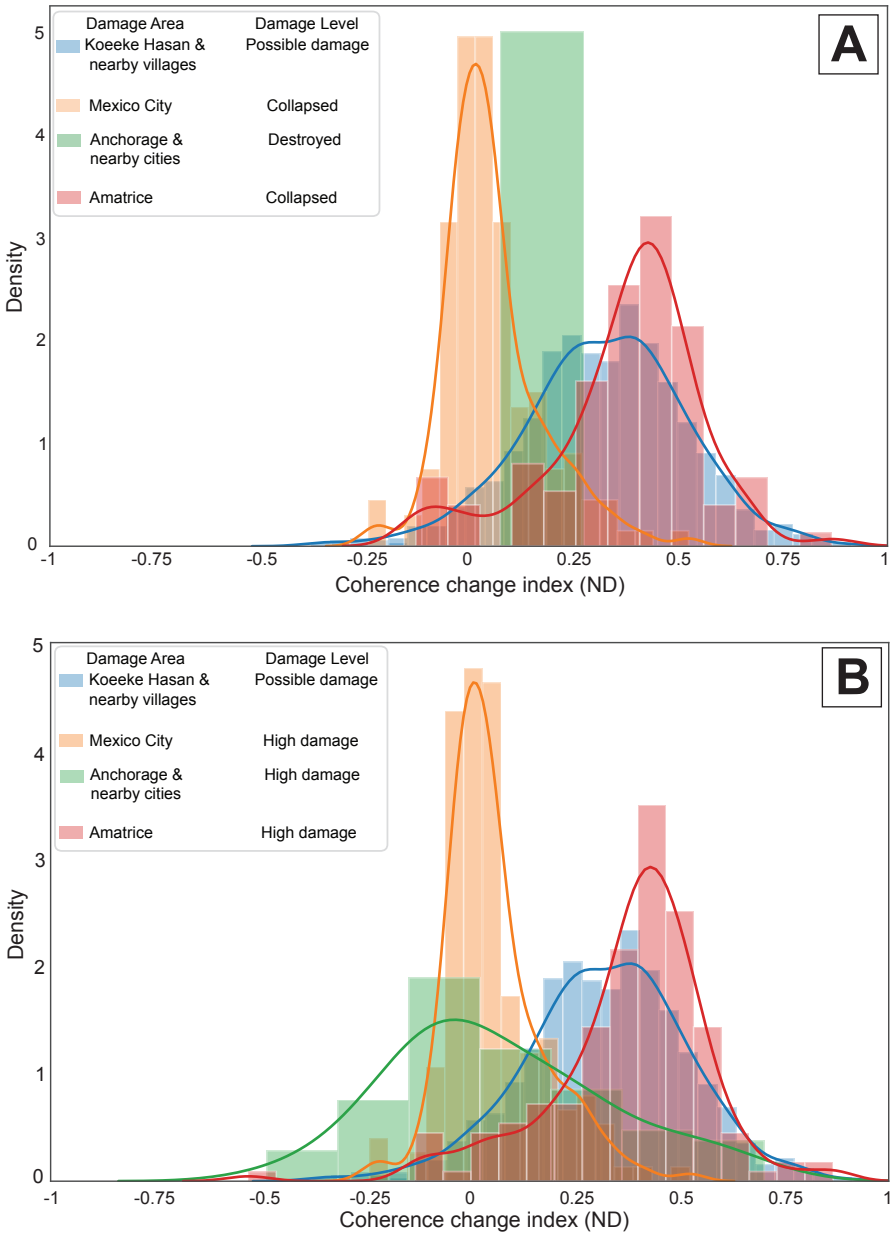


Figure 4.10: Normalized distribution of mean coherence change (calculated using a normalized difference, ND) for highly damaged buildings from the Amatrice, Puebla–Morelos, Sarpol-e-Zahab, and Anchorage earthquakes. Distributions are fit with a kernel density estimate, where bin heights reflect probability densities. (A) shows the distribution of the highest available damage levels (see Table 4.2) surveyed from the four earthquakes. (B) shows the distribution for the top two highest available damage levels surveyed from each earthquake (see 'High damage' category, Table 4.2).

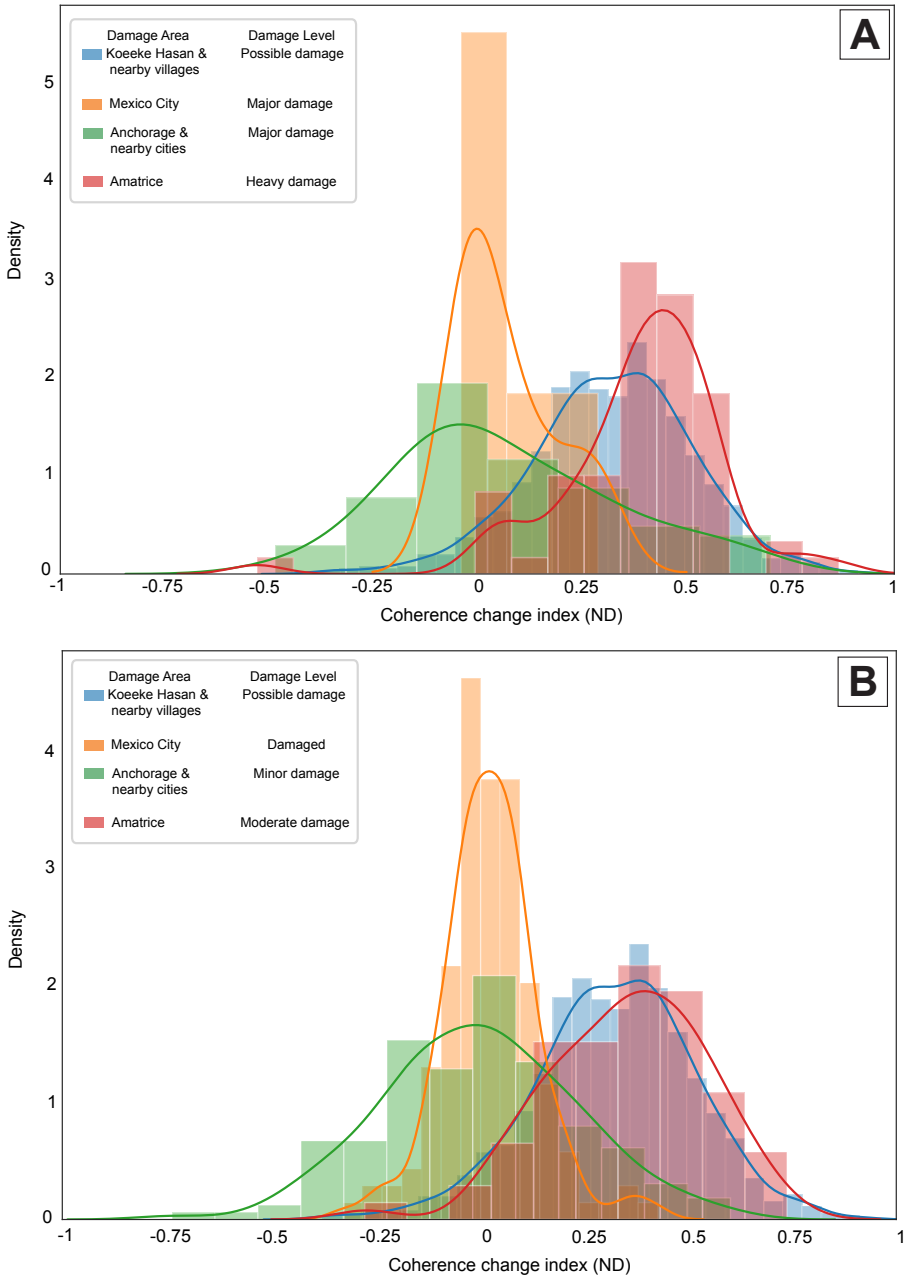


Figure 4.11: Normalized distribution of mean coherence change (calculated using a normalized difference, ND) for majorly (A) and moderately (B) damaged buildings from the Amatrice, Puebla–Morelos, Sarpol-e-Zahab, and Anchorage earthquakes (see Table 4.2). Bin heights reflect probability densities and are fit with a kernel density estimate.

### 4.5.1 Damage Density and Pixel Mixing

The differences in spatial resolution between the coherence pixels and the size of buildings on the ground resulted in pixel mixing. Each pixel within a coherence map contained signal contributions from several ground targets within the resolution cell. Building polygons did not fall perfectly in the center of a coherence pixel and often were within or touching small groups of pixels. When there were several pixels near each other that contain damaged buildings, the contribution of damaged buildings to the total signal increased, resulting in a stronger coherence change signal from damaged buildings. Therefore, regions of greater damage density had higher mean coherence change values than regions of lower damage density. For example, the concentrated damage in the western region of Amatrice appears bright in the co-seismic coherence change map in Figure 4.8A. From Figures 4.3 and 4.5 the damage density in Amatrice and selected Kermanshah villages from the Amatrice and Sarpol-e-Zahab earthquakes were the greatest. Structural damage caused by the Puebla–Morelos and Anchorage earthquakes in Mexico City and the Anchorage area was less concentrated in comparison (see Figures 4.4 and 4.6).

These areas of highest damage density had overall higher average mean coherence change values in damaged areas (Table 4.2). Structural damage in Amatrice and Sarpol-e-Zahab (12km south of the Kermanshah villages considered in this study) has been previously studied using coherence change analysis. A study using Sentinel-1 and ALOS-2 imagery found mean normalized coherence difference of $\sim$0.33 for collapsed structures in Amatrice [112], which is within the range of our calculated coherence change values of 0.3729 $\pm$0.1829. This study jointly used intensity and coherence correlations with optical imagery and polarimetry to calculate the weighted normalized differential coherence. A comparative study of Amatrice and Sarpol-e-Zahab used VV polarized Sentinel-1 data and used a minimum threshold of normalized difference coherence change of 0.2 to separate collapsed structures from intact buildings, which is somewhat consistent with our findings [111]. However, Sarpol-e-Zahab has a greater proportion of newer, taller (3 - 6 stories) buildings than the Kermanshah villages, which influenced the coherence change signal and damage pattern of Sarpol-e-Zahab [133]. Although the ARIA group published a damage proxy map of damage to Mexico City following the 2016 Puelba–Morelos earthquake, the coherence change values were not available for comparison. Lastly, our study found a mean coherence change value of 0.1755 was calculated for the single collapsed building in the Anchorage area, which is significantly higher than the calculated values for lower damage levels from the Anchorage earthquake.

As shown in Figure 4.9, there is little separability between mean coherence change of

surveyed damage levels of each earthquake. This is also due to pixel mixing of different damage categories where, if there are buildings of two different damage levels near each other, the subset of pixels used to calculate the mean coherence change value of each of those damage polygons would include mostly the same coherence change pixels. This was especially the case for damage in Amatrice, where heavily damaged buildings often occurred very close to each other, resulting in similar calculated statistics of mean coherence change in Table 4.2. Additionally, if there are stable buildings surrounding a damaged building, there will be pixel mixing with the surrounding undamaged building, resulting in a large coherence change contribution of $\sim$0 from stable buildings. This is why all mean coherence change distributions for most damage levels in the Anchorage area and all damage levels in Mexico City are centered close to zero in Table 4.2 and Figure 4.9.

### 4.5.2 Environmental Influence

Although only coherence change pixels touching surveyed damage polygons were used in this study, vegetation and urban coverage played important roles given the significant influence of pixel mixing caused by the difference in resolution of the coherence maps and surveyed data. To quantitatively assess and compare potential environmental influences on coherence change, supervised land cover classifications were performed for each of the four case studies (see Figure A.3 and Table A.3).

The coherence signal from vegetation is consistently decorrelated because it is affected by things like wind, where even over a short time period, the form and shape of vegetation can change, causing phase shifts between signals. The effects of volumetric and environmental temporal decorrelation had the greatest influence on coherence mapping in damaged areas of Amatrice and the Anchorage area. These two areas had the greatest amount of vegetation cover at 71.9% and 38.1%, respectively. Coherence signals for Mexico City and the Kermanshah villages were less influenced by vegetation, given their lower vegetation coverage at 30.9% and 5.1%, respectively (Table A.3). The long tails of the distribution of mean coherence change for Amatrice in Figure 4.10 may be due to pixel mixing with vegetation surrounding small buildings and around the perimeter of the town (see Figure A.3). Vegetation proximal to damaged buildings in the Anchorage area may also explain the wide distribution curves in Figure 4.10B.

Further, the Anchorage earthquake occurred in late November (2018), when snow had already begun to fall in Alaska ($\sim$ 17.1% snow coverage in the region, Figure A.3). Coherence can also be affected by changes in form and shape of snow which can vary over a short time

periods due to wind, additional snow fall, and melting of snow. During the pre-seismic image acquisition dates (see Table 4.1), a total of ∼4.6 cm of snow fell in the Anchorage area, while a total of ∼35.1 cm snow fell between co-seismic acquisition dates (station US1AKAB0055, Alaska [148]). Thus, temporal decorrelation from snow is another contributing factor to the utility and wide distribution of mean coherence change in the Anchorage area in Figure 4.10B.

Figure 4.10 shows a narrow distribution of mean coherence change for damage in Mexico City due to low vegetation in the city and high coverage of urban area (57.2% built area coverage, Table A.3). The coherence change signal for damage in Mexico City was dominated by stable, coherent buildings due to pixel mixing, resulting in a strong peak in mean coherence change around zero.

### 4.5.3 Limitations

This method of coherence change detection for damage mapping was subject to several limitations. The greatest limitation to the radar data was the image acquisition dates based on satellite revisit times. Although temporal baselines were kept short, 6-day interferograms were only available for the Sarpol-e-Zahab earthquake. The other three study areas had 12 day temporal resolutions, meaning there was a slightly lower contribution of temporal decorrelation to the coherence maps of the Sarpol-e-Zahab area. However, post-seismic images as close to the earthquake date as available were chosen to limit natural temporal decorrelation and volumetric decorrelation from vegetation growth. Ideally, radar data would be from just before and just after the earthquake to isolate the co-seismic decorrelation. However, there are currently no SAR satellites capable of this revisit time frequency (see Section 4.6). Lastly, the initial spatial resolution of the radar data was a limiting factor on the final, processed resolution of the coherence maps. The resolution of the coherence maps dictates the amount of pixel mixing and number of ground targets that contribute to the total coherence signal. Therefore, finer spatial resolution of the coherence maps would result in more accurate calculations of mean coherence change per surveyed building polygon.

The availability of surveyed building damage data was also a limiting factor in this study. The surveyed damage data was sourced from optical imagery, foot, and aerial image surveys. Additionally, the surveyed data for each case study quantified damage differently. Ideally, the methods of surveying damage for each case study would be identical and use the same damage classification schemes for more accurate comparisons. Further, the shapefile type of surveyed data were not consistent across all four case studies. For example, building polygon data for Amatrice was the most accurate representation of the amount of ground

coverage affected by damaged buildings. Surveyed damage for Mexico City, the Kermanshah villages and the Anchorage area were recorded as coordinate points. Buffering the point data introduced a source of error because it was an approximation of the sizes of the damaged buildings. The sizes of damaged building varied for each area but only one buffer size was applied to all point data for each case study. For increased accuracy, all surveyed damage data could have been field surveyed and recorded as building footprint polygons.

## 4.6 Future Implications

Satellite revisit times are shorter than they used to be and will continue to shorten with future launches. For example, the Canadian Space Agency's Radarsat Constellation Mission (RCM) launched a trio or C-band SAR satellites in 2019, which have a global revisit time of 4 days across all three satellites [149]. Further, ICEYE is a third party mission by a Finnish company that has launched four small SAR satellites with the goal of launching more satellites by 2021 to have a revisit time of 1 day across the constellation [150]. Another goal of ICEYE is to improve image resolution, unveiling in early 2020 that their constellation was capable of imaging at 25 cm $\times$ 50 cm (azimuth $\times$ range) resolution. Table 4.3 summarizes current and future SAR satellites used for environmental and hazard monitoring. With finer spatial resolution and increasing image frequency, coherence change mapping will become more widely accessible and could become a more widely used method of emergency response. Finer resolutions would allow damage levels of individual buildings to be more accurately assessed. Increased revisit times would result in more rapid and frequent coherence change calculations, increasing the potential for utility for emergency rescue following a damaging natural hazard event.

In this study, I used surveyed building damage data and coherence change analysis to calculate the value of mean coherence change for each surveyed damage polygon of four earthquake case studies. However, to best implement coherence change mapping in future emergency response, coherence change maps could be created and then masked to map the areas of greatest coherence change to delineate where the greatest structural damage likely is, after outlier removal. Therefore, our findings confirm that an approach like the ARIA group's, where the top 0.1% to 0.4% of the range of coherence change values were classified as the pixels that contained the greatest probable damage [88], is a good solution to implement this method without the use of damage threshold levels.

Table 4.3: Current and future SAR satellites [1].

| Satellite | Wavelength | Constellation | Launch | Revisit time (days) | Resolution |
|---|---|---|---|---|---|
| ALOS-2 (Japan) | L-Band | 1 | 2014 | 14 | 1 - 100 m |
| COSMO-SkyMed (CSK) (Italy) | X-Band | 4 | 2007 | 16 individually, ∼4 across constellation | 1 - 100 m |
| COSMO-SkyMed 2nd Gen. CSG 1 and 2 (to replace CSK) | X-Band | 2 | 2019-2021 | 16 individually, ∼8 across constellation | 0.8 - 20 m |
| NISAR (NASA + India) | L-Band S-Band | 1 with two sensors | 2022 | 12 | 3 - 10 m |
| RCM (Canada) | C-Band | 3 | 2019 | 12 individually, ∼4 across constellation | 1 - 100 m |
| ICEYE (Europe) | X-Band | 4 | 2018-2021 | 18 individually, goal of 24 hr across constellation by 2021 | 0.25 - 20 m |
| Sentinel-1 (Europe) | C-Band | 2 | 2014-2016 | 12 individually, 6 across constellation | 1 - 100 m |
| SAOCOM-1 (Argentina) | L-Band | 2 | 2018-2020 | 16 individually, 8 across constellation | 7 - 100 m |

Alternatively, NASA's UAVSAR is an Uninhabited Aerial Vehicle that carries an L-band SAR system, capable of repeat-pass interferometry, as well as a Ka-band and P-band sensor, for single pass interferometry and vegetative studies, respectively [151, 152]. This airborne platform has been operational since 2009 and is capable of producing unwrapped interferograms with 7 m resolution [152]. UAVSAR acquisitions have been used to study creep and earthquake ground deformation, among other natural hazard applications (eg. refs. [152, 153, 154]), where individual flight lines are deployed in requested areas. Although this platform is not flown globally regularly, like many SAR satellites, UAVSAR acquisitions could be another useful, high resolution tool in coherence change analysis to identify damaged buildings, capable of very short revisit times in some cases.

Another approach to implement this method would be to use building footprint data when available, often published by government agencies or open source databases like OpenStreetMap, to mask out all coherence change pixels that do not fall within the bounds of regional building data sets and compare the coherence change values of only these pixels. This would mask the influence of other decorrelated ground targets. However, at the spatial resolution used in this study, the influence of pixel mixing may still contribute to the coherence change signal. A vegetation mask could also be implemented by processing several pre-seismic pairs to identify regions of high coherence fluctuation or standard deviation, which would signify pixels dominated by vegetation. Urban areas in pre-seismic pairs would return stable, consistent signals and would be correlated. For example, a study of the 1995 Kobe earthquake used a pre-seismic coherence threshold of $\geq 0.6$ to identify pixels containing buildings before calculating the coherence change [89].

## 4.7 Conclusions

Overall, structural damage in areas with high damage density yielded higher mean coherence change values. However, based on the zonal statistics presented in Table 4.2, there is not a single, mean coherence change threshold that can be assigned universally across all four case study areas to separate levels of building damage. Although each of the four study areas suffered structural damage, the influences of pixel mixing, damage density, and additional sources of decorrelation played important roles in the utility of this method of damage mapping. When comparing areas of high damage, the influence of these factors on coherence change of built areas must be considered. This method of coherence mapping is most successful in regions with high damage density and little vegetation and snow cover. In these areas, this method of damage mapping would be most useful as an initial, wide coverage assessment to get a general estimate of highly damaged communities following a destructive earthquake. The oblique viewing geometry of SAR offers imaging capability of the sides of buildings and does not rely on roof damage as an indicator of earthquake damage (unlike hurricane damage). However, with the current spatial resolution of Sentinel-1 data, this method of mapping may be best suited to assess overall damage and damage density of city blocks rather than individual structures.

# Appendix A

# Supplementary Information

Table A.1: Parameters calculated from fault-perpendicular swath profiles along the (M)ain, (Wh)arekiri, (Wa)inui and (E)dgecombe strands, as well as (F)ar field displacements across all three coastal faults. Latitude and longitude refer to profile center-points, listed from N to S for each strand. $x$, $y$ and $z$ offsets refer to motion of the west side of the fault with respect to the east side.

| label | Latitude | Longitude | strike | $x$ offset ($m$) | $y$ offset ($m$) | $z$ offset ($m$) | net offset ($m$) | fault dip | rake |
|---|---|---|---|---|---|---|---|---|---|
| *Northern and central main strand (Clarence Valley)* | | | | | | | | | |
| M 1 | -42.11330° | 173.84468° | 122.8° | 3.76 ± 0.72 | -2.38 ± 0.49 | 6.08 ± 0.15 | 7.53 ± 0.89 | 89.7° SW ± 4.4° | 53.8° |
| M 2 | -42.11378° | 173.84571° | 302.8° | 2.17 ± 0.53 | -3.21 ± 0.40 | 5.91 ± 0.13 | 7.07 ± 0.68 | 75.6° NE ± 3.3° | -59.7° |
| M 3 | -42.11426° | 173.84673° | 122.8° | 2.92 ± 0.87 | -1.61 ± 0.70 | 6.27 ± 0.24 | 7.10 ± 1.14 | 87.9° SW ± 5.5° | 62.0° |
| M 4 | -42.11522° | 173.84878° | 302.8° | 2.18 ± 1.02 | -2.33 ± 0.96 | 6.19 ± 0.12 | 6.96 ± 1.40 | 82.8° NE ± 6.5° | -63.6° |
| M 5 | -42.11618° | 173.85082° | 302.8° | 2.11 ± 0.59 | -1.60 ± 0.88 | 6.67 ± 0.11 | 7.17 ± 1.07 | 88.2° NE ± 4.8° | -68.4° |
| M 6 | -42.11666° | 173.85185° | 302.8° | 2.71 ± 0.39 | -2.89 ± 0.35 | 6.74 ± 0.09 | 7.81 ± 0.53 | 81.9° NE ± 2.6° | -60.6° |
| M 7 | -42.11714° | 173.85287° | 302.8° | 2.71 ± 0.42 | -2.97 ± 0.44 | 6.89 ± 0.06 | 7.98 ± 0.61 | 81.5° NE ± 2.6° | -60.8° |
| M 8 | -42.11761° | 173.85391° | 301.6° | 3.15 ± 0.48 | -3.22 ± 0.49 | 7.10 ± 0.05 | 8.41 ± 0.69 | 81.2° NE ± 3.0° | -58.5° |
| M 9 | -42.12245° | 173.85925° | 139.3° | 3.57 ± 0.66 | -2.79 ± 0.59 | 6.35 ± 0.36 | 7.80 ± 0.95 | 82.0° SW ± 3.5° | 55.3° |
| M 10 | -42.12313° | 173.86005° | 139.3° | 2.97 ± 0.33 | -2.19 ± 0.53 | 7.50 ± 0.11 | 8.35 ± 0.63 | 83.7° SW ± 2.7° | 64.5° |
| M 11 | -42.12381° | 173.86085° | 139.3° | 3.71 ± 0.21 | -2.98 ± 0.34 | 7.93 ± 0.10 | 9.25 ± 0.41 | 83.8° SW ± 1.7° | 59.6° |
| M 12 | -42.12449° | 173.86165° | 145.2° | 3.85 ± 0.16 | -3.23 ± 0.22 | 8.19 ± 0.10 | 9.61 ± 0.29 | 80.9° SW ± 1.1° | 59.7° |
| M 13 | -42.12522° | 173.86235° | 145.2° | 4.29 ± 0.30 | -3.20 ± 0.42 | 8.10 ± 0.06 | 9.71 ± 0.52 | 78.2° SW ± 2.0° | 58.4° |
| M 14 | -42.12595° | 173.86305° | 145.2° | 3.89 ± 0.22 | -3.51 ± 0.20 | 8.25 ± 0.08 | 9.77 ± 0.30 | 81.8° SW ± 1.1° | 58.5° |
| M 15 | -42.12669° | 173.86375° | 145.2° | 4.13 ± 0.47 | -2.52 ± 0.48 | 8.15 ± 0.14 | 9.47 ± 0.69 | 76.6° SW ± 2.9° | 62.1° |
| M 16 | -42.12742° | 173.86445° | 145.3° | 4.13 ± 0.37 | -2.97 ± 0.55 | 7.87 ± 0.12 | 9.37 ± 0.67 | 77.8° SW ± 2.6° | 59.3° |
| M 17 | -42.12816° | 173.86515° | 145.3° | 4.21 ± 0.31 | -3.56 ± 0.31 | 7.71 ± 0.08 | 9.48 ± 0.44 | 79.4° SW ± 1.5° | 55.9° |
| M 18 | -42.12898° | 173.86563° | 157.9° | 3.90 ± 0.86 | -3.24 ± 1.10 | 7.44 ± 0.25 | 9.00 ± 1.42 | 72.1° SW ± 5.7° | 60.2° |
| M 19 | -42.13576° | 173.86850° | 181.7° | 3.53 ± 1.14 | -3.22 ± 0.44 | 9.12 ± 0.25 | 10.30 ± 1.25 | 68.3° W ± 1.2° | 72.4° |
| M 20 | -42.13666° | 173.86848° | 181.7° | 5.91 ± 1.23 | -4.31 ± 0.69 | 8.85 ± 0.39 | 11.48 ± 1.46 | 55.7° W ± 2.0° | 68.9° |
| M 21 | -42.14107° | 173.86751° | 195.8° | 3.31 ± 2.12 | -3.12 ± 1.37 | 8.10 ± 0.36 | 9.29 ± 2.55 | 63.5° W ± 3.9° | 77.0° |
| M 22 | -42.14370° | 173.86655° | 195.8° | 3.14 ± 0.95 | -3.54 ± 0.63 | 9.04 ± 0.06 | 10.20 ± 1.14 | 66.2° W ± 3.7° | 75.6° |
| M 23 | -42.14457° | 173.86623° | 195.8° | 2.94 ± 0.54 | -3.85 ± 0.72 | 9.16 ± 0.07 | 10.36 ± 0.91 | 67.1° W ± 3.2° | 73.7° |
| M 24 | -42.14891° | 173.86493° | 180.3° | 2.07 ± 0.62 | -3.01 ± 1.09 | 9.02 ± 0.20 | 9.73 ± 1.27 | 77.0° W ± 6.2° | 72.1° |
| M 25 | -42.14981° | 173.86494° | 179.9° | 3.22 ± 0.89 | -4.04 ± 0.73 | 9.52 ± 0.16 | 10.83 ± 1.16 | 71.3° W ± 4.2° | 68.1° |
| M 26 | -42.15070° | 173.86501° | 159.8° | 2.94 ± 0.89 | -3.08 ± 1.07 | 8.86 ± 0.09 | 9.83 ± 1.39 | 79.2° W ± 4.8° | 66.6° |
| M 27 | -42.15155° | 173.86544° | 159.8° | 3.22 ± 0.62 | -3.29 ± 0.68 | 8.93 ± 0.07 | 10.05 ± 0.92 | 78.1° W ± 3.7° | 65.3° |
| | | | **Average:** | 3.36 ± 0.84 | -3.03 ± 0.63 | 7.78 ± 1.10 | 9.03 ± 1.25 | 81.1° W ± 12.0° | 63.7° ± 6.4° |
| *Southern main strand (coast)* | | | | | | | | | |
| M 28 | -42.19047° | 173.87810° | 158.7° | 1.78 ± 0.70 | -3.19 ± 0.52 | 1.92 ± 0.39 | 4.12 ± 0.95 | 75.2° W ± 5.5° | 28.7° |
| M 29 | -42.19131° | 173.87855° | 158.7° | 2.66 ± 0.43 | -2.39 ± 0.61 | 1.87 ± 0.43 | 4.04 ± 0.86 | 49.3° W ± 7.5° | 37.8° |
| M 30 | -42.19215° | 173.87897° | 172.5° | 2.46 ± 0.55 | -3.68 ± 0.67 | 1.80 ± 0.37 | 4.78 ± 0.94 | 42.7° W ± 6.2° | 33.8° |
| M 31 | -42.19304° | 173.87914° | 172.5° | 3.80 ± 0.52 | -4.14 ± 0.84 | 2.75 ± 0.45 | 6.25 ± 1.08 | 40.5° W ± 6.0° | 42.7° |
| M 32 | -42.19393° | 173.87931° | 172.5° | 3.29 ± 0.65 | -3.11 ± 0.81 | 3.27 ± 0.31 | 5.58 ± 1.09 | 48.9° W ± 8.2° | 51.0° |
| M 33 | -42.19482° | 173.87950° | 165.2° | 3.23 ± 0.58 | -3.93 ± 0.59 | 4.23 ± 0.15 | 6.62 ± 0.84 | 63.4° W ± 3.9° | 45.6° |
| M 34 | -42.19562° | 173.88004° | 149.2° | 2.85 ± 0.55 | -3.96 ± 0.80 | 3.98 ± 0.27 | 6.30 ± 1.00 | 84.0° W ± 4.7° | 39.5° |
| | | | **Average:** | 2.87 ± 0.65 | -3.48 ± 0.62 | 2.83 ± 1.02 | 5.38 ± 1.07 | 57.7° W ± 16.8° | 39.9° ± 7.42° |
| *Main strand, combined* | | | | | | | | | |
| | | | **Average:** | 3.26 ± 0.82 | -3.12 ± 0.65 | 6.76 ± 2.29 | 8.82 ± 1.92 | 76.2° W ± 16.0° | 58.8° ± 11.8° |

| label | Latitude | Longitude | strike | $x$ offset $(m)$ | $y$ offset $(m)$ | $z$ offset $(m)$ | net offset $(m)$ | fault dip | rake |
|---|---|---|---|---|---|---|---|---|---|
| *Wharekiri strand* | | | | | | | | | |
| Wh 1 | -42.12520° | 173.84372° | 140.5° | 0.20 ± 0.20 | -0.69 ± 0.15 | -0.70 ± 0.18 | 1.00 ± 0.31 | 67.7° SW ± 5.2° | -48.8° |
| Wh 2 | -42.12692° | 173.84430° | 350.9° | 0.30 ± 0.28 | -1.13 ± 0.17 | -0.77 ± 0.14 | 1.40 ± 0.36 | 81.0° E ± 3.3° | 33.9° |
| Wh 3 | -42.12781° | 173.84450° | 350.9° | 0.41 ± 0.27 | -0.90 ± 0.17 | -0.50 ± 0.12 | 1.11 ± 0.34 | 62.4° E ± 3.7° | 30.9° |
| Wh 4 | -42.12869° | 173.84470° | 350.9° | 0.51 ± 0.31 | -0.99 ± 0.20 | -0.72 ± 0.19 | 1.32 ± 0.41 | 64.4° E ± 4.3° | 37.2° |
| Wh 5 | -42.12958° | 173.84494° | 344.2° | 0.73 ± 0.29 | -1.29 ± 0.37 | -0.92 ± 0.17 | 1.74 ± 0.50 | 68.9° E ± 4.3° | 34.4° |
| Wh 6 | -42.13395° | 173.84638° | 349.2° | 0.42 ± 0.26 | -0.83 ± 0.21 | -1.22 ± 0.12 | 1.53 ± 0.35 | 77.9° E ± 3.1° | 54.5° |
| Wh 7 | -42.13483° | 173.84662° | 349.2° | 0.52 ± 0.14 | -1.04 ± 0.08 | -1.34 ± 0.07 | 1.77 ± 0.18 | 76.7° E ± 1.3° | 50.8° |
| Wh 8 | -42.13651° | 173.84745° | 338.3° | 0.48 ± 0.09 | -0.97 ± 0.18 | -1.51 ± 0.10 | 1.86 ± 0.22 | 86.6° E ± 2.1° | 54.4° |
| Wh 9 | -42.13901° | 173.84883° | 338.3° | 0.81 ± 0.17 | -0.93 ± 0.08 | -1.71 ± 0.14 | 2.11 ± 0.24 | 76.4° E ± 1.5° | 56.5° |
| Wh 10 | -42.13983° | 173.84933° | 333.8° | 0.45 ± 0.12 | -0.71 ± 0.13 | -1.57 ± 0.10 | 1.79 ± 0.21 | 86.6° E ± 2.0° | 62.0° |
| Wh 11 | -42.14064° | 173.84987° | 333.8° | 0.29 ± 0.10 | -0.71 ± 0.15 | -1.47 ± 0.07 | 1.66 ± 0.19 | 87.8° W ± 2.2° | -62.5° |
| Wh 12 | -42.14225° | 173.85096° | 333.8° | 0.37 ± 0.17 | -0.68 ± 0.20 | -1.40 ± 0.10 | 1.60 ± 0.28 | 88.5° E ± 3.0° | 61.0° |
| Wh 13 | -42.14305° | 173.85151° | 333.8° | 0.34 ± 0.13 | -0.63 ± 0.34 | -1.31 ± 0.10 | 1.49 ± 0.38 | 89.0° E ± 4.7° | 61.4° |
| Wh 14 | -42.14391° | 173.85186° | 345.0° | 0.24 ± 0.18 | -0.39 ± 0.22 | -1.10 ± 0.14 | 1.19 ± 0.31 | 83.5° E ± 4.8° | 68.3° |
| Wh 15 | -42.14478° | 173.85218° | 345.0° | 0.49 ± 0.18 | -0.52 ± 0.21 | -1.19 ± 0.14 | 1.39 ± 0.32 | 73.9° E ± 4.5° | 62.8° |
| | | | **Average:** | 0.44 ± 0.17 | -0.83 ± 0.24 | -1.16 ± 0.36 | 1.53 ± 0.30 | 81.4° E ± 12.4° | 52.0° ± 12.3° |
| *Wainui strand* | | | | | | | | | |
| Wa 1 | -42.19841° | 173.87500° | 177.7° | -0.03 ± 0.94 | 0.59 ± 0.75 | -4.18 ± 0.29 | 4.22 ± 1.24 | 90.0° W ± 7.6° | -98.1° |
| Wa 2 | -42.19931° | 173.87506° | 177.7° | -1.30 ± 0.73 | 0.01 ± 0.60 | -4.23 ± 0.23 | 4.43 ± 0.97 | 72.9° W ± 4.6° | -90.8° |
| Wa 3 | -42.20021° | 173.87512° | 177.7° | -1.62 ± 0.70 | 0.52 ± 0.41 | -3.88 ± 0.45 | 4.24 ± 0.93 | 67.6° W ± 5.5° | -98.0° |
| | | | **Average:** | -0.98 ± 0.85 | 0.37 ± 0.32 | -4.09 ± 0.19 | 4.29 ± 0.11 | 76.8° W ± 11.7° | -95.6° ± 4.19° |
| *Edgecombe strand* | | | | | | | | | |
| E 1 | -42.18908° | 173.88165° | 171.9° | 3.26 ± 0.69 | -1.22 ± 0.47 | 0.52 ± 0.21 | 3.52 ± 0.86 | 9.7° W ± 8.9° | 61.7° |
| E 2 | -42.18997° | 173.88183° | 171.9° | 2.93 ± 0.64 | -1.57 ± 0.67 | 0.87 ± 0.22 | 3.44 ± 0.95 | 17.9° W ± 11.4° | 55.1° |
| | | | **Average:** | 3.09 ± 0.23 | -1.40 ± 0.24 | 0.69 ± 0.24 | 3.48 ± 0.06 | 13.8° W ± 5.8° | 58.4° ± 4.67° |

| label | Latitude | Longitude | strike | $x$ offset $(m)$ | $y$ offset $(m)$ | $z$ offset $(m)$ | net offset $(m)$ | fault dip | rake |
|---|---|---|---|---|---|---|---|---|---|
| *Coastal strands, Far-field* | | | | | | | | | |
| F 1 | -42.18847° | 173.87702° | 158.7° | 5.45 ± 0.47 | -4.79 ± 0.47 | 2.44 ± 0.22 | 7.65 ± 0.70 | 36.1° W ± 2.2° | 32.7° |
| F 2 | -42.18888° | 173.87724° | 158.7° | 6.20 ± 0.76 | -4.32 ± 0.56 | 2.50 ± 0.32 | 7.96 ± 1.00 | 30.7° W ± 3.3° | 38.0° |
| F 3 | -42.18930° | 173.87747° | 158.7° | 5.83 ± 0.81 | -5.17 ± 0.83 | 2.27 ± 0.27 | 8.12 ± 1.19 | 32.6° W ± 3.0° | 31.3° |
| F 4 | -42.19014° | 173.87792° | 158.7° | 5.33 ± 0.81 | -4.54 ± 0.94 | 1.53 ± 0.34 | 7.16 ± 1.29 | 24.8° W ± 3.8° | 30.7° |
| F 5 | -42.19056° | 173.87814° | 158.7° | 4.18 ± 0.77 | -3.21 ± 0.75 | 2.59 ± 0.24 | 5.87 ± 1.10 | 43.4° W ± 5.0° | 39.8° |
| F 6 | -42.19139° | 173.87859° | 158.7° | 3.55 ± 0.87 | -4.55 ± 0.76 | 1.87 ± 0.78 | 6.07 ± 1.39 | 48.4° W ± 7.8° | 24.3° |
| F 7 | -42.19531° | 173.87979° | 149.2° | 5.43 ± 4.09 | -3.98 ± 0.57 | 1.40 ± 0.48 | 6.88 ± 4.16 | 28.1° W ± 9.9° | 25.6° |
| F 8 | -42.19570° | 173.88010° | 149.2° | 4.59 ± 2.15 | -3.52 ± 0.67 | 1.03 ± 0.86 | 5.88 ± 2.41 | 25.7° W ± 8.8° | 23.9° |
| | | | **Average:** | 5.07 ± 0.89 | -4.26 ± 0.65 | 1.95 ± 0.58 | 6.95 ± 0.93 | 33.7° W ± 8.47° | 30.8° ± 6.02° |

Table A.2: Elastic forward model parameters to for the (M)ain strand, a lower (L)istric extension of the steeper upper Papatea main strand, the (J)ordan and (K)ekerengu faults, and the (S)ubduction interface. Depth ranges of slip are indicated next to the fault name.

| label | center easting | center northing | length ($km$) | net offset ($m$) | strike | fault dip | rake |
|---|---|---|---|---|---|---|---|
| *Papatea surface rupture (0-10km)* | | | | | | | |
| 1 (M 1–M 8) | 734737.13 | 5334018.23 | 3.002 | 7.5 | 305.0° | 84.3° E | -60.9° |
| 2 (M 9–M 17) | 736412.87 | 5332603.10 | 1.469 | 9.2 | 142.0° | 80.5° W | 59.3° |
| 3 (M 18) | 736977.00 | 5331651.02 | 0.767 | 9.0 | 160.0° | 72.1° W | 60.2° |
| 4 (M 19–M 20) | 737083.91 | 5331071.88 | 0.442 | 10.9 | 185.0° | 62.0° W | 70.7° |
| 5 (M 21–M 23) | 736896.09 | 5330341.80 | 1.055 | 10.0 | 196.0° | 65.6° W | 75.4° |
| 6 (M 24–M 25) | 736733.55 | 5329683.35 | 0.311 | 10.3 | 180.0° | 74.2° W | 70.1° |
| 7 (M 26–M 27) | 736845.96 | 5329201.63 | 0.679 | 9.9 | 163.0° | 78.6° W | 66.0° |
| 8 (M 27–M 28) | 737287.73 | 5327108.51 | 3.500 | 7.1 | 170.0° | 76.7° W | 47.0° |
| 9 (M 29–M 34) | 737946.70 | 5323955.00 | 2.900 | 5.6 | 168.0° | 54.8° W | 41.7° |

| label | center easting | center northing | length ($km$) | net offset ($m$) | strike | fault dip | rake |
|---|---|---|---|---|---|---|---|
| *Listric Papatea structure (10-20km)* | | | | | | | |
| L 1 | 744099.26 | 5320647.72 | 3.002 | 7.5 | 125.0° | 30.0° W | 60.9° |
| L 2 | 748742.94 | 5342236.41 | 1.469 | 9.2 | 142.0° | 30.0° W | 59.3° |
| L 3 | 750217.83 | 5336470.29 | 0.767 | 9.0 | 160.0° | 30.0° W | 60.2° |
| L 4 | 749041.65 | 5330025.71 | 0.442 | 10.9 | 185.0° | 30.0° W | 70.7° |
| L 5 | 749185.15 | 5326817.97 | 1.055 | 10.0 | 196.0° | 30.0° W | 75.4° |
| L 6 | 751233.55 | 5329683.35 | 0.311 | 10.3 | 180.0° | 30.0° W | 70.1° |
| L 7 | 751481.40 | 5333676.13 | 0.679 | 9.9 | 163.0° | 30.0° W | 66.0° |
| L 8 | 752017.11 | 5329705.70 | 3.500 | 7.1 | 170.0° | 30.0° W | 47.0° |
| L 9 | 747988.64 | 5326089.48 | 2.900 | 5.6 | 168.0° | 30.0° W | 41.7° |

| label | center easting | center northing | length ($km$) | net offset ($m$) | strike | fault dip | rake |
|---|---|---|---|---|---|---|---|
| *Jordan and Kekerengu ruptures (0-20km)* | | | | | | | |
| J | 730799.32 | 5333087.05 | 6.327 | 6.0 | 223.0° | 60.0° W | -165.0° |
| K | 736998.75 | 5339467.22 | 11.427 | 9.0 | 224.0° | 55.0° W | 140.0° |

| label | center easting | center northing | length ($km$) | net offset ($m$) | strike | fault dip | rake |
|---|---|---|---|---|---|---|---|
| *Subduction interface (15-38km)* | | | | | | | |
| S | 282165.51 | 5308061.26 | 121.152 | 2.0 | 225.0° | 25.0° W | 125.0° |

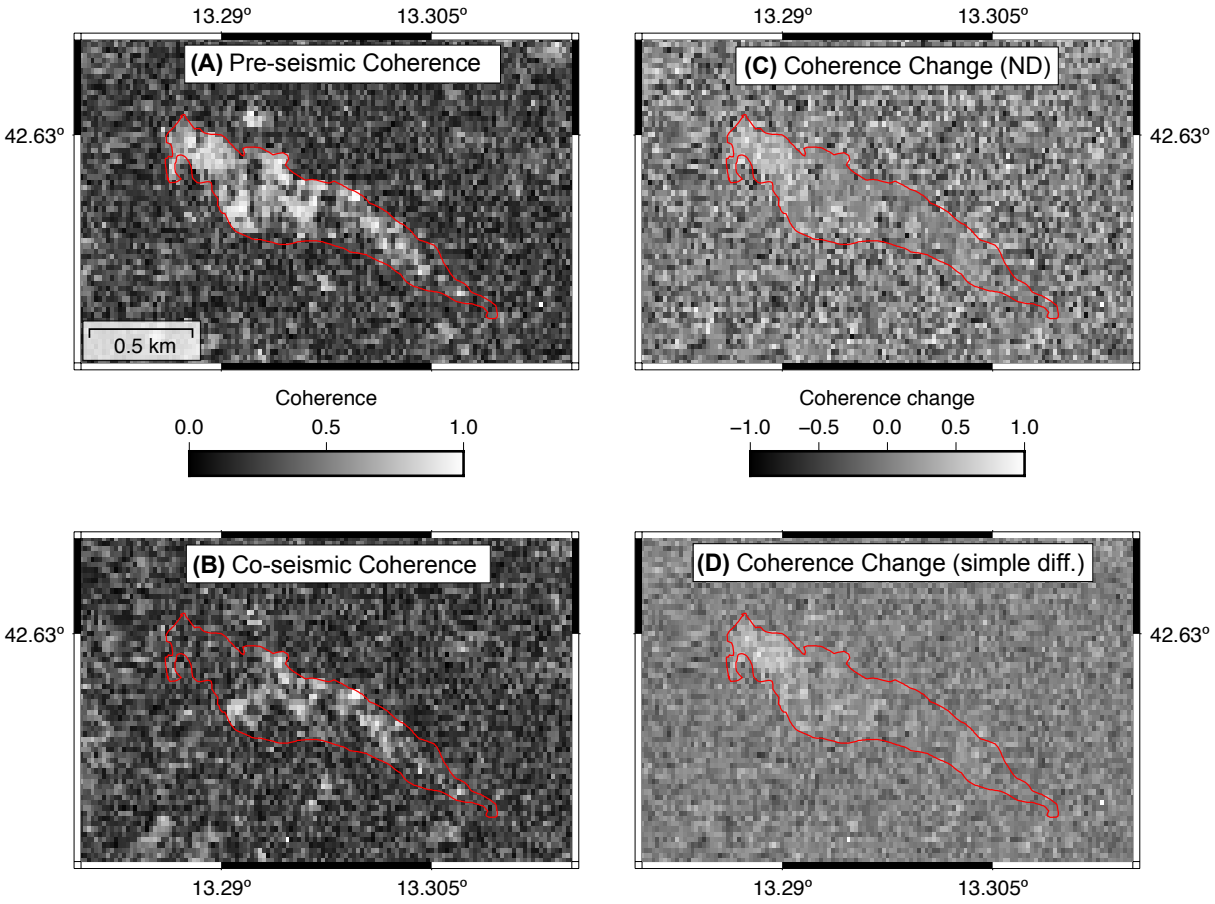


Figure A.1: Coherence and coherence change images for Amatrice, Central Italy following the first event of the 2016 Central Italy Earthquake Sequence. (A) and (B) are the pre- and co-seismic coherence images. (C) is the co-seismic coherence change calculated from a normalized difference (see Equation 3 and (D) is the co-seismic coherence change calculated using a simple difference. The red polygon delineates Amatrice, Italy. Coherence images were processed using a $3 \times 3$ pixel window.

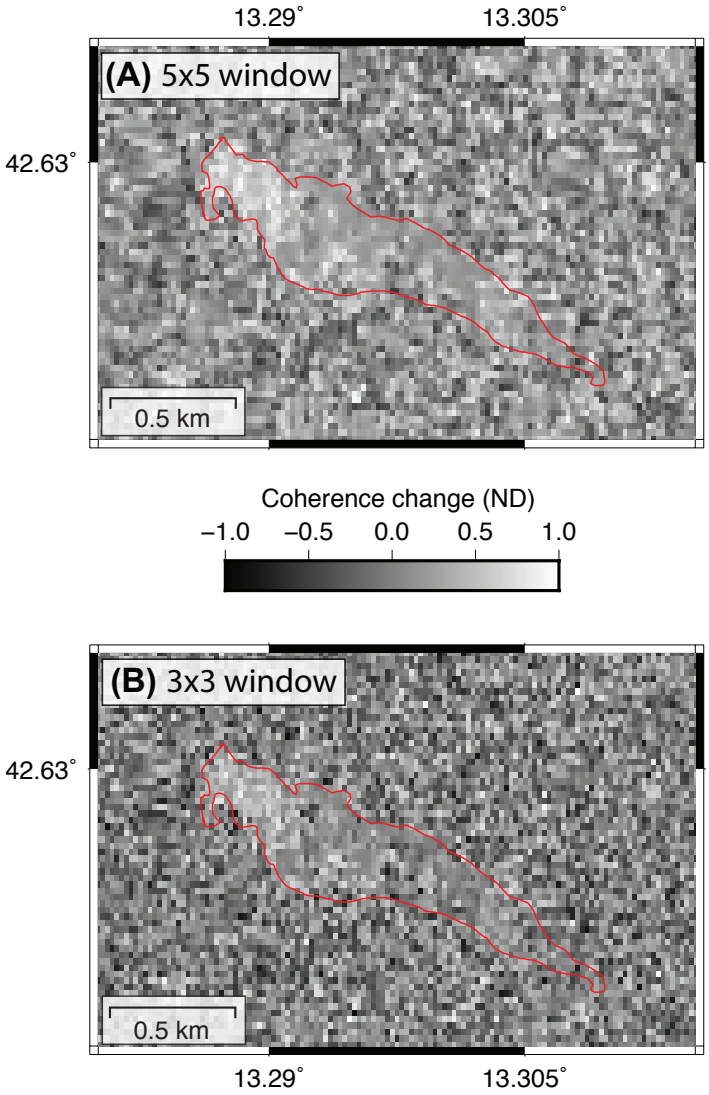


Figure A.2: Normalized difference co-seismic coherence change images for Amatrice using (A) $5 \times 5$ and (B) $3 \times 3$ pixel windows. The red polygon delineates Amatrice, Italy.

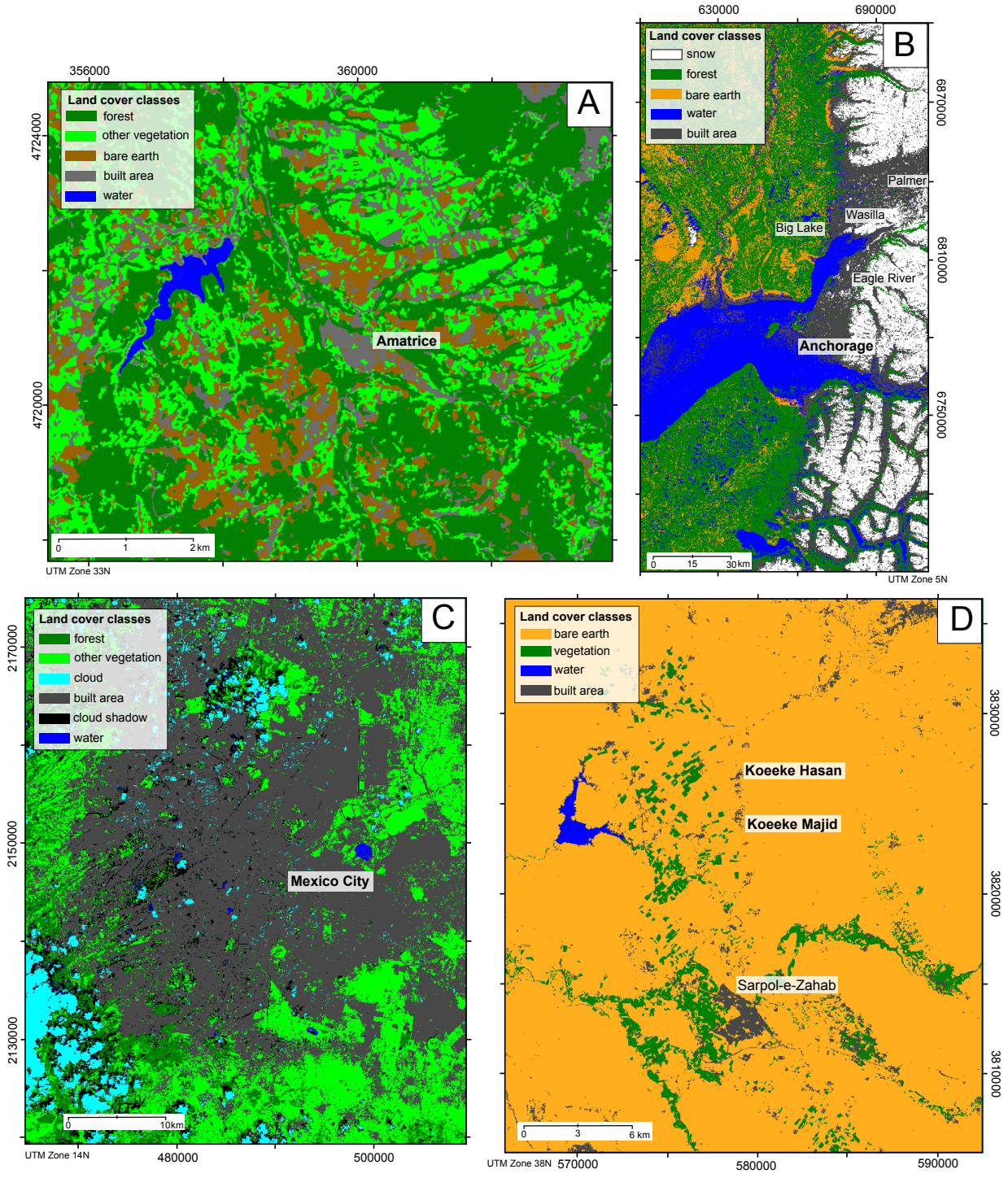


Figure A.3: Supervised land cover classifications for (A) Central Italy (98.5% overall accuracy), (B) Anchorage and surrounding cities (89.1% overall accuracy), (C) Mexico City (95.7% overall accuracy), (D) Kermanshah Province, Iran (96.7% overall accuracy). Classifications were done using 10 m Sentinel-2 imagery using a maximum likelihood classification and a $3 \times 3$ pixel kernel and $7 \times 7$ pixel aggregation [141].

Table A.3: Coverage of land cover classes (see Figure A.3) from < 15% cloud cover, 10 m Sentinel-2 imagery [141].

| **Class** | **% cover** |
|---|---|
| *Central Italy (acquired 2016-08-14)* | |
| Water | 1 |
| Vegetation | 71.9 |
| Bare earth | 14.8 |
| Built area | 12.3 |

| **Class** | **% cover** |
|---|---|
| *Mexico City (acquired 2017-10-14)* | |
| Vegetation | 30.9 |
| Built area | 57.2 |
| Cloud | 5 |
| Water | 0.3 |
| Shadow | 6.5 |

| **Class** | **% cover** |
|---|---|
| *Kermanshah Province, Iran (acquired 2017-10-16)* | |
| Water | 0.5 |
| Bare earth | 91.2 |
| Vegetation | 5.1 |
| Built area | 3.3 |

| **Class** | **% cover** |
|---|---|
| *Anchorage area (acquired 2018-11-04)* | |
| Snow | 17.1 |
| Bare earth | 11.3 |
| Built area | 17.8 |
| Water | 15.6 |
| Vegetation | 38.1 |

# Bibliography

[1] UNAVCO, "Synthetic Aperture Radar (SAR) Satellites." https://www.unavco.org/instrumentation/geophysical/imaging/sar-satellites/sar-satellites.html, 2019. Accessed: 2020-04-04.

[2] E. C. Barrett and L. F. Curtis, *Introduction to Environmental Remote Sensing*. Psychology Press, 1999.

[3] J. B. Campbell and R. H. Wynne, *Introduction to Remote Sensing*. Guilford Press, 2011.

[4] J. R. Jensen, *Remote sensing of the environment: An earth resource perspective 2/e*. Pearson Education India, 2009.

[5] E. Johnson, R. Meyer, R. Hopkins, and W. Mock, "The measurement of light scattered by the upper atmosphere from a search-light beam," *Journal of the Optical Society of America*, vol. 29, no. 12, pp. 512–517, 1939.

[6] E. Synge, "XCI. A method of investigating the higher atmosphere," *The London, Edinburgh, and Dublin Philosophical Magazine and Journal of Science*, vol. 9, no. 60, pp. 1014–1020, 1930.

[7] F. Ackermann, "Airborne laser scanning: present status and future expectations," *ISPRS Journal of Photogrammetry and Remote Sensing*, vol. 54, no. 2-3, pp. 64–67, 1999.

[8] T. Markus, T. Neumann, A. Martino, W. Abdalati, K. Brunt, B. Csatho, S. Farrell, H. Fricker, A. Gardner, D. Harding, and M. Jasinski, "The Ice, Cloud, and land Elevation Satellite-2 (ICESat-2): science requirements, concept, and implementation," *Remote Sensing of Environment*, vol. 190, pp. 260–273, 2017.

[9] R. Abdelfattah and J.-M. Nicolas, "Interferometric SAR coherence magnitude estimation using second kind statistics," *IEEE Transactions on Geoscience and Remote Sensing*, vol. 44, no. 7, pp. 1942–1953, 2006.

[10] M. A. Lefsky, W. B. Cohen, G. G. Parker, and D. J. Harding, "Lidar remote sensing for ecosystem studies: Lidar, an emerging remote sensing technology that directly measures the three-dimensional distribution of plant canopies, can accurately estimate vegetation structural attributes and should be of particular interest to forest, landscape, and global ecologists," *BioScience*, vol. 52, no. 1, pp. 19–30, 2002.

[11] D. Gatziolis and H.-E. Andersen, "A guide to LIDAR data acquisition and processing for the forests of the Pacific Northwest.," *Gen. Tech. Rep. PNW-GTR-768. Portland, OR: US Department of Agriculture, Forest Service, Pacific Northwest Research Station. 32 p*, vol. 768, 2008.

[12] W. E. Carter, R. L. Shrestha, and K. C. Slatton, "Geodetic laser scanning," *Physics Today*, vol. 60, no. 12, p. 41, 2007.

[13] E. Nissen, T. Maruyama, J. R. Arrowsmith, J. R. Elliott, A. K. Krishnan, M. E. Oskin, and S. Saripalli, "Coseismic fault zone deformation revealed with differential lidar: Examples from Japanese Mw 7 intraplate earthquakes," *Earth and Planetary Science Letters*, vol. 405, pp. 244–256, 2014.

[14] M. E. Oskin, J. R. Arrowsmith, A. H. Corona, A. J. Elliott, J. M. Fletcher, E. J. Fielding, P. O. Gold, J. J. G. Garcia, K. W. Hudnut, J. Liu-Zeng, and O. Teran, "Near-field deformation from the El Mayor–Cucapah earthquake revealed by differential LIDAR," *Science*, vol. 335, no. 6069, pp. 702–705, 2012.

[15] M. Jaboyedoff, T. Oppikofer, A. Abellán, M.-H. Derron, A. Loye, R. Metzger, and A. Pedrazzini, "Use of LIDAR in landslide investigations: a review," *Natural hazards*, vol. 61, no. 1, pp. 5–28, 2012.

[16] G. Teza, A. Galgaro, N. Zaltron, and R. Genevois, "Terrestrial laser scanner to detect landslide displacement fields: a new approach," *International Journal of Remote Sensing*, vol. 28, no. 16, pp. 3425–3446, 2007.

[17] K. Clark, E. Nissen, J. Howarth, I. Hamling, J. Mountjoy, W. Ries, K. Jones, S. Goldstien, U. Cochran, P. Villamor, and S. Hreinsdóttir, "Highly variable coastal deformation in the 2016 Mw7. 8 Kaikōura earthquake reflects rupture complexity along a trans-

pressional plate boundary," *Earth and Planetary Science Letters*, vol. 474, pp. 334–344, 2017.

[18] E. Nissen, A. K. Krishnan, J. R. Arrowsmith, and S. Saripalli, "Three-dimensional surface displacements and rotations from differencing pre- and post-earthquake LiDAR point clouds," *Geophysical Research Letters*, vol. 39, no. 16, 2012.

[19] C. Scott, J. Champenois, Y. Klinger, E. Nissen, T. Maruyama, T. Chiba, and R. Arrowsmith, "The 2016 M7 Kumamoto, Japan, earthquake slip field derived from a joint inversion of differential lidar topography, optical correlation, and InSAR surface displacements," *Geophysical Research Letters*, vol. 46, no. 12, pp. 6341–6351, 2019.

[20] S. Leprince, E. Berthier, F. Ayoub, C. Delacourt, and J.-P. Avouac, "Monitoring earth surface dynamics with optical imagery," *Eos, Transactions American Geophysical Union*, vol. 89, no. 1, pp. 1–2, 2008.

[21] M. Matsuoka and S. Kodama, "Coseismic displacement measurement of the 2010 El Mayor, Mexico earthquake by subpixel correlation from optical satellite images," in *2011 IEEE International Geoscience and Remote Sensing Symposium*, pp. 4010–4013, IEEE, 2011.

[22] S. Bouaziz, A. Tagliasacchi, and M. Pauly, "Sparse iterative closest point," in *Proceedings of the Eleventh Eurographics/ACMSIGGRAPH Symposium on Geometry Processing*, pp. 113–123, Eurographics Association, 2013.

[23] S. Rusinkiewicz and M. Levoy, "Efficient Variants of the ICP Algorithm," in *3dim*, vol. 1, pp. 145–152, 2001.

[24] D. L. Hill, P. G. Batchelor, M. Holden, and D. J. Hawkes, "Medical image registration," *Physics in medicine & biology*, vol. 46, no. 3, p. R1, 2001.

[25] Y. Chen and G. Meioni, "Object Modeling by Registration of Multiple Range Images," in *Proceedings International Conference Robotics and Automation*, pp. 2724–2729, 1991.

[26] T. Oppikofer, M. Jaboyedoff, L. Blikra, and R. Metzger, "Characterization and monitoring of the Åknes rockslide using terrestrial laser scanning," *Natural Hazards and Earth System Sciences*, vol. 9, no. 3, p. 1003, 2009.

[27] L. Moya, F. Yamazaki, W. Liu, and M. Yamada, "Detection of collapsed buildings from lidar data due to the 2016 Kumamoto earthquake in Japan," *Natural Hazards and Earth System Sciences*, vol. 18, no. 1, p. 65, 2018.

[28] F. Yamazaki and W. Liu, "Remote sensing technologies for post-earthquake damage assessment: A case study on the 2016 Kumamoto earthquake," in *Keynote Lecture, 6th Asia Conference on Earthquake Engineering*, p. 8p, 2016.

[29] M. Li, L. Cheng, J. Gong, Y. Liu, Z. Chen, F. Li, G. Chen, D. Chen, and X. Song, "Post-earthquake assessment of building damage degree using LiDAR data and imagery," *Science in China Series E: Technological Sciences*, vol. 51, no. 2, pp. 133–143, 2008.

[30] L. J. Lajoie, E. Nissen, K. L. Johnson, J. R. Arrowsmith, C. L. Glennie, A. Hinojosa-Corona, and M. E. Oskin, "Extent of Low-Angle Normal Slip in the 2010 El Mayor-Cucapah (Mexico) Earthquake From Differential Lidar," *Journal of Geophysical Research: Solid Earth*, vol. 124, no. 1, pp. 943–956, 2019.

[31] C. P. Scott, J. R. Arrowsmith, E. Nissen, L. Lajoie, T. Maruyama, and T. Chiba, "The M7 2016 Kumamoto, Japan, earthquake: 3-D deformation along the fault and within the damage zone constrained from differential Lidar topography," *Journal of Geophysical Research: Solid Earth*, vol. 123, no. 7, pp. 6138–6155, 2018.

[32] G. Born, J. Dunne, and D. Lame, "Seasat mission overview," *Science*, vol. 204, no. 4400, pp. 1405–1406, 1979.

[33] R. Bamler and P. Hartl, "Synthetic aperture radar interferometry," *Inverse problems*, vol. 14, no. 4, p. R1, 1998.

[34] P. A. Rosen, S. Hensley, I. R. Joughin, F. K. Li, S. N. Madsen, E. Rodriguez, and R. M. Goldstein, "Synthetic aperture radar interferometry," *Proceedings of the IEEE*, vol. 88, no. 3, pp. 333–382, 2000.

[35] A. Moreira, P. Prats-Iraola, M. Younis, G. Krieger, I. Hajnsek, and K. P. Papathanassiou, "A tutorial on synthetic aperture radar," *IEEE Geoscience and Remote Sensing Magazine*, vol. 1, no. 1, pp. 6–43, 2013.

[36] C. Elachi, T. Bicknell, R. L. Jordan, and C. Wu, "Spaceborne synthetic-aperture imaging radars: Applications, techniques, and technology," *Proceedings of the IEEE*, vol. 70, no. 10, pp. 1174–1209, 1982.

[37] S. Nasonova, R. K. Scharien, C. Haas, and S. E. Howell, "Linking regional winter sea ice thickness and surface roughness to spring melt pond fraction on landfast arctic sea ice," *Remote Sensing*, vol. 10, no. 1, p. 37, 2018.

[38] A. Donnellan, J. Parker, C. Milliner, T. G. Farr, M. Glasscoe, Y. Lou, Y. Zheng, and B. Hawkins, "UAVSAR and optical analysis of the thomas fire scar and montecito debris flows: Case study of methods for disaster response using remote sensing products," *Earth and Space Science*, vol. 5, no. 7, pp. 339–347, 2018.

[39] D. Massonnet and K. L. Feigl, "Radar interferometry and its application to changes in the Earth's surface," *Reviews of Geophysics*, vol. 36, no. 4, pp. 441–500, 1998.

[40] R. F. Hanssen, *Radar interferometry: data interpretation and error analysis*, vol. 2. Springer Science & Business Media, 2001.

[41] R. Torres, P. Snoeij, D. Geudtner, D. Bibby, M. Davidson, E. Attema, P. Potin, B. Rommen, N. Floury, M. Brown, and I. Traver, "GMES Sentinel-1 mission," *Remote Sensing of Environment*, vol. 120, pp. 9–24, 2012.

[42] F. De Zan and A. M. Guarnieri, "TOPSAR: Terrain observation by progressive scans," *IEEE Transactions on Geoscience and Remote Sensing*, vol. 44, no. 9, pp. 2352–2360, 2006.

[43] A. Ferretti, A. Monti-Guarnieri, C. Prati, and F. Rocca, "Part C InSAR processing: a mathematical approach," *InSAR Principles: Guidelines for SAR Interferometry Procs. and Interpretation, K. Fletcher, Ed., ESA Publications: Noordwijk, Netherlands*, pp. 3–13, 2007.

[44] P. Merot, A. Crave, C. Gascuel-Odoux, and S. Louhala, "Effect of saturated areas on backscattering coefficient of the ERS 1 synthetic aperture radar: First results," *Water Resources Research*, vol. 30, no. 2, pp. 175–179, 1994.

[45] S. R. Cloude and E. Pottier, "A review of target decomposition theorems in radar polarimetry," *IEEE transactions on geoscience and remote sensing*, vol. 34, no. 2, pp. 498–518, 1996.

[46] E. Rignot, K. Echelmeyer, and W. Krabill, "Penetration depth of interferometric synthetic-aperture radar signals in snow and ice," *Geophysical Research Letters*, vol. 28, no. 18, pp. 3501–3504, 2001.

[47] E. Rignot and R. Chellappa, "Segmentation of polarimetric synthetic aperture radar data," *IEEE Transactions on Image Processing*, vol. 1, no. 3, pp. 281–300, 1992.

[48] J. Kirkhorn, "Introduction to IQ-demodulation of RF-data," *IFBT, NTNU*, vol. 15, 1999.

[49] M. Kuisma, "Software Defined Radio: I/Q Data explained." http://whiteboard.ping.se/SDR/IQ, 2017. Accessed: 2019-12-01.

[50] M. Furuya, "SAR interferometry," *Encyclopedia of Solid Earth Geophysics*, pp. 1041–1049, 2011.

[51] T. Young, *A syllabus of a course of lectures on natural and experimental philosophy.* From the Press of the Royal Institution, 1802.

[52] T. Young, *A course of lectures on natural philosophy and the mechanical arts: in two volumes*, vol. 2. Johnson, 1807.

[53] "Interferometric Synthetic Aperture Radar. Geoscience Australia." https://www.ga.gov.au/scientific-topics/positioning-navigation/geodesy/geodetic-techniques/interferometric-synthetic-aperture-radar. Accessed: 2019-12-01.

[54] L. Meng, J.-P. Ampuero, J. Stock, Z. Duputel, Y. Luo, and V. Tsai, "Earthquake in a maze: Compressional rupture branching during the 2012 Mw 8.6 Sumatra earthquake," *Science*, vol. 337, no. 6095, pp. 724–726, 2012.

[55] J. M. Fletcher, M. E. Oskin, and O. J. Teran, "The role of a keystone fault in triggering the complex El Mayor–Cucapah earthquake rupture," *Nature Geoscience*, vol. 9, no. 4, p. 303, 2016.

[56] E. Nissen, J. Elliott, R. Sloan, T. Craig, G. Funning, A. Hutko, B. Parsons, and T. Wright, "Limitations of rupture forecasting exposed by instantaneously triggered earthquake doublet," *Nature Geoscience*, vol. 9, no. 4, p. 330, 2016.

[57] I. J. Hamling, S. Hreinsdóttir, K. Clark, J. Elliott, C. Liang, E. Fielding, N. Litchfield, P. Villamor, L. Wallace, T. J. Wright, *et al.*, "Complex multifault rupture during the 2016 Mw 7.8 Kaikōura earthquake, New Zealand," *Science*, vol. 356, no. 6334, p. eaam7194, 2017.

[58] S. Lamb, R. Arnold, and J. D. Moore, "Locking on a megathrust as a cause of distributed faulting and fault-jumping earthquakes," *Nature Geoscience*, vol. 11, no. 11, p. 871, 2018.

[59] J. Hollingsworth, L. Ye, and J.-P. Avouac, "Dynamically triggered slip on a splay fault in the Mw 7.8, 2016 Kaikoura (New Zealand) earthquake," *Geophysical Research Letters*, vol. 44, no. 8, pp. 3517–3525, 2017.

[60] H. Zhang, K. D. Koper, K. Pankow, and Z. Ge, "Imaging the 2016 Mw 7.8 Kaikoura, New Zealand, earthquake with teleseismic P waves: A cascading rupture across multiple faults," *Geophysical Research Letters*, vol. 44, no. 10, pp. 4790–4798, 2017.

[61] N. J. Litchfield, P. Villamor, R. J. V. Dissen, A. Nicol, P. M. Barnes, D. J. A. Barrell, J. R. Pettinga, R. M. Langridge, T. A. Little, R. W. Mountjoy, Joshu J, J. Rowland, C. Fenton, M. Stirling, J. Kearse, K. Berryman, U. Cochran, K. Clark, M. Hemphill-Haley, N. Khajavi, K. Jones, G. Archibald, P. Upton, C. Asher, A. Benson, S. Cox, C. Gasston, D. Hale, B. Hall, A. Hatem, D. Heron, J. Howarth, T. Kane, G. Lamarche, S. Lawson, B. Lukovic, S. McColl, C. Madugo, J. Manousakis, D. Noble, K. Pedley, K. Sauer, T. Stahl, D. Strong, D. Townsend, V. Toy, J. Williams, S. Woelz, and R. Zinke, "Surface rupture of multiple crustal faults in the 2016 M w 7.8 Kaikōura, New Zealand, earthquake," *Bulletin of the Seismological Society of America*, vol. 108, no. 3B, pp. 1496–1520, 2018.

[62] R. M. Langridge, J. Rowland, P. Villamor, J. Mountjoy, D. B. Townsend, E. Nissen, C. Madugo, W. F. Ries, C. Gasston, A. Canva, and A. Hatem, "Coseismic Rupture and Preliminary Slip Estimates for the Papatea Fault and Its Role in the 2016 Mw 7.8 Kaikōura, New Zealand, Earthquake Coseismic Rupture and Preliminary Slip Estimates for the Papatea Fault," *Bulletin of the Seismological Society of America*, vol. 108, no. 3B, pp. 1596–1622, 2018.

[63] F. Tan, Z. Ge, H. Kao, and E. Nissen, "Validation of the 3-D phase-weighted relative back projection technique and its application to the 2016 M w 7.8 Kaikōura earthquake," *Geophysical Journal International*, vol. 217, no. 1, pp. 375–388, 2019.

[64] D. L. Wells and K. J. Coppersmith, "New empirical relationships among magnitude, rupture length, rupture width, rupture area, and surface displacement," *Bulletin of the seismological Society of America*, vol. 84, no. 4, pp. 974–1002, 1994.

[65] A. Kaiser, N. Balfour, B. Fry, C. Holden, N. Litchfield, M. Gerstenberger, E. D'anastasio, N. Horspool, G. McVerry, J. Ristau, and S. Bannister, "The 2016 Kaikōura, New Zealand, earthquake: preliminary seismological report," *Seismological Research Letters*, vol. 88, no. 3, pp. 727–739, 2017.

[66] D. Wang, Y. Chen, Q. Wang, and J. Mori, "Complex rupture of the 13 November 2016 Mw 7.8 Kaikoura, New Zealand earthquake: Comparison of high-frequency and low-frequency observations," *Tectonophysics*, vol. 733, pp. 100–107, 2018.

[67] N. Litchfield, R. Van Dissen, R. Sutherland, P. Barnes, S. Cox, R. Norris, R. Beavan, R. Langridge, P. Villamor, K. Berryman, and M. Stirling, "A model of active faulting in New Zealand," *New Zealand Journal of Geology and Geophysics*, vol. 57, no. 1, pp. 32–56, 2014.

[68] L. M. Wallace, J. Beavan, R. McCaffrey, K. Berryman, and P. Denys, "Balancing the plate motion budget in the South Island, New Zealand using GPS, geological and seismological data," *Geophysical Journal International*, vol. 168, no. 1, pp. 332–352, 2007.

[69] J. Beavan, L. M. Wallace, N. Palmer, P. Denys, S. Ellis, N. Fournier, S. Hreinsdóttir, C. Pearson, and M. Denham, "New Zealand GPS velocity field: 1995–2013," *New Zealand Journal of Geology and Geophysics*, vol. 59, no. 1, pp. 5–14, 2016.

[70] D. P. Mason and T. A. Little, "Refined slip distribution and moment magnitude of the 1848 Marlborough earthquake, Awatere Fault, New Zealand," *New Zealand Journal of Geology and Geophysics*, vol. 49, no. 3, pp. 375–382, 2006.

[71] Y. Bai, T. Lay, K. F. Cheung, and L. Ye, "Two regions of seafloor deformation generated the tsunami for the 13 November 2016, Kaikoura, New Zealand earthquake," *Geophysical Research Letters*, vol. 44, no. 13, pp. 6597–6606, 2017.

[72] W. Xu, G. Feng, L. Meng, A. Zhang, J. P. Ampuero, R. Bürgmann, and L. Fang, "Transpressional rupture cascade of the 2016 Mw 7.8 Kaikoura earthquake, New Zealand," *Journal of Geophysical Research: Solid Earth*, vol. 123, no. 3, pp. 2396–2409, 2018.

[73] R. Zinke, J. Hollingsworth, J. F. Dolan, and R. Van Dissen, "Three-Dimensional Surface Deformation in the 2016 MW 7.8 Kaikōura, New Zealand, Earthquake From Optical Image Correlation: Implications for Strain Localization and Long-Term Evolution

of the Pacific-Australian Plate Boundary," *Geochemistry, Geophysics, Geosystems*, vol. 20, no. 3, pp. 1609–1628, 2019.

[74] C. Holden, Y. Kaneko, E. D'Anastasio, R. Benites, B. Fry, and I. Hamling, "The 2016 Kaikōura earthquake revealed by kinematic source inversion and seismic wavefield simulations: Slow rupture propagation on a geometrically complex crustal fault network," *Geophysical Research Letters*, vol. 44, no. 22, pp. 11–320, 2017.

[75] Z. Duputel and L. Rivera, "Long-period analysis of the 2016 Kaikoura earthquake," *Physics of the Earth and Planetary Interiors*, vol. 265, pp. 62–66, 2017.

[76] T. Wang, S. Wei, X. Shi, Q. Qiu, L. Li, D. Peng, R. J. Weldon, and S. Barbot, "The 2016 Kaikōura earthquake: Simultaneous rupture of the subduction interface and overlying faults," *Earth and Planetary Science Letters*, vol. 482, pp. 44–51, 2018.

[77] R. Langridge, W. Ries, N. Litchfield, P. Villamor, R. Van Dissen, D. Barrell, M. Rattenbury, D. Heron, S. Haubrock, D. Townsend, and J. Lee, "The New Zealand active faults database," *New Zealand Journal of Geology and Geophysics*, vol. 59, no. 1, pp. 86–96, 2016.

[78] Y. Klinger, K. Okubo, A. Vallage, J. Champenois, A. Delorme, E. Rougier, Z. Lei, E. E. Knight, A. Munjiza, C. Satriano, and S. Baize, "Earthquake damage patterns resolve complex rupture processes," *Geophysical Research Letters*, vol. 45, no. 19, pp. 10–279, 2018.

[79] T. Ulrich, A.-A. Gabriel, J.-P. Ampuero, and W. Xu, "Dynamic viability of the 2016 Mw 7.8 Kaikōura earthquake cascade on weak crustal faults," *Nature communications*, vol. 10, no. 1, p. 1213, 2019.

[80] Y.-Y. Wen, K.-F. Ma, and B. Fry, "Multiple-Fault, Slow Rupture of the 2016 Mw 7.8 Kaikōura, New Zealand, Earthquake: Complementary Insights from Teleseismic and Geodetic DataMultiple-Fault, Slow Rupture of the 2016 Kaikōura Earthquake," *Bulletin of the Seismological Society of America*, vol. 108, no. 3B, pp. 1774–1783, 2018.

[81] Y. Morishita, T. Kobayashi, S. Fujiwara, and H. Yarai, "Complex Crustal Deformation of the 2016 Kaikoura, New Zealand, Earthquake Revealed by ALOS-2Complex Crustal Deformation of the 2016 Kaikoura, New Zealand, Earthquake Revealed by ALOS-2," *Bulletin of the Seismological Society of America*, vol. 107, no. 6, pp. 2676–2686, 2017.

[82] D. Mackenzie and A. Elliott, "Untangling tectonic slip from the potentially misleading effects of landform geometry," *Geosphere*, vol. 13, no. 4, pp. 1310–1328, 2017.

[83] Y. Okada, "Surface deformation due to shear and tensile faults in a half-space," *Bulletin of the seismological society of America*, vol. 75, no. 4, pp. 1135–1154, 1985.

[84] H. Noda and N. Lapusta, "Stable creeping fault segments can become destructive as a result of dynamic weakening," *Nature*, vol. 493, no. 7433, p. 518, 2013.

[85] R. Y. Chuang and K. M. Johnson, "Reconciling geologic and geodetic model fault slip-rate discrepancies in Southern California: Consideration of nonsteady mantle flow and lower crustal fault creep," *Geology*, vol. 39, no. 7, pp. 627–630, 2011.

[86] S. Plank, "Rapid Damage Assessment by Means of Multi-Temporal SAR — A Comprehensive Review and Outlook to Sentinel-1," *Remote Sensing*, vol. 6, no. 6, pp. 4870–4906, 2014.

[87] E. J. Fielding, M. Talebian, P. A. Rosen, H. Nazari, J. A. Jackson, M. Ghorashi, and R. Walker, "Surface ruptures and building damage of the 2003 Bam, Iran, earthquake mapped by satellite synthetic aperture radar interferometric correlation," *Journal of Geophysical Research: Solid Earth*, vol. 110, no. B3, 2005.

[88] S.-H. Yun, K. Hudnut, S. Owen, F. Webb, M. Simons, P. Sacco, E. Gurrola, G. Manipon, C. Liang, E. Fielding, and P. Milillo, "Rapid Damage Mapping for the 2015 M w 7.8 Gorkha Earthquake Using Synthetic Aperture Radar Data from COSMO–SkyMed and ALOS-2 Satellites," *Seismological Research Letters*, vol. 86, no. 6, pp. 1549–1556, 2015.

[89] Y. Ito, M. Hosokawa, H. Lee, and J. G. Liu, "Extraction of damaged regions using SAR data and neural networks," *International Archives of Photogrammetry and Remote Sensing*, vol. 33, no. B1; PART 1, pp. 156–163, 2000.

[90] C. Yonezawa, N. Tomiyama, and S. Takeuchi, "Urban damage detection using decorrelation of SAR interferometric data," in *IEEE International Geoscience and Remote Sensing Symposium*, vol. 4, pp. 2051–2053, IEEE, 2002.

[91] S. Stramondo, C. Bignami, M. Chini, N. Pierdicca, and A. Tertulliani, "Satellite radar and optical remote sensing for earthquake damage detection: results from different case studies," *International Journal of Remote Sensing*, vol. 27, no. 20, pp. 4433–4447, 2006.

[92] H. A. Zebker and J. Villasenor, "Decorrelation in interferometric radar echoes," *IEEE Transactions on Geoscience and Remote Sensing*, vol. 30, no. 5, pp. 950–959, 1992.

[93] M. Seymour and I. Cumming, "Maximum likelihood estimation for SAR interferometry," in *Proceedings of IGARSS'94-1994 IEEE International Geoscience and Remote Sensing Symposium*, vol. 4, pp. 2272–2275, IEEE, 1994.

[94] C. López-Martínez and E. Pottier, "Coherence estimation in synthetic aperture radar data based on speckle noise modeling," *Applied optics*, vol. 46, no. 4, pp. 544–558, 2007.

[95] J. Hoffmann, "Mapping damage during the Bam (Iran) earthquake using interferometric coherence," *International Journal of Remote Sensing*, vol. 28, no. 6, pp. 1199–1216, 2007.

[96] S. Xiong, J.-P. Muller, and G. Li, "The application of ALOS/PALSAR InSAR to measure subsurface penetration depths in deserts," *Remote Sensing*, vol. 9, no. 6, p. 638, 2017.

[97] Z. Lu, "InSAR imaging of volcanic deformation over cloud-prone areas–Aleutian Islands," *Photogrammetric Engineering & Remote Sensing*, vol. 73, no. 3, pp. 245–257, 2007.

[98] H. Lee and J. G. Liu, "Analysis of topographic decorrelation in SAR interferometry using ratio coherence imagery," *IEEE Transactions on Geoscience and Remote Sensing*, vol. 39, no. 2, pp. 223–232, 2001.

[99] G. J. Funning, B. Parsons, T. J. Wright, J. A. Jackson, and E. J. Fielding, "Surface displacements and source parameters of the 2003 Bam (Iran) earthquake from Envisat advanced synthetic aperture radar imagery," *Journal of Geophysical Research: Solid Earth*, vol. 110, no. B9, 2005.

[100] N. Tamkuan and M. Nagai, "Fusion of multi-temporal interferometric coherence and optical image data for the 2016 Kumamoto earthquake damage assessment," *ISPRS International Journal of Geo-Information*, vol. 6, no. 7, p. 188, 2017.

[101] S. Stramondo, M. Moro, C. Tolomei, F. Cinti, and F. Doumaz, "InSAR surface displacement field and fault modelling for the 2003 Bam earthquake (southeastern Iran)," *Journal of Geodynamics*, vol. 40, pp. 347–353, 2005.

[102] "Copernicus Emergency Management Service." http://emergency.copernicus.eu/mapping/ems/emergency-management-service. Accessed: 2019-11-24.

[103] "United Nations Institute for Training and Research (UNITAR) Operational Satellite Applications Programme (UNOSAT)." http://www.unitar.org/unosat/. Accessed: 2019-11-20.

[104] "The International Charter of Space and Major Disasters." http://www.disasterscharter.org/. Accessed: 2019-12-02.

[105] E. Christophe, A. S. Chia, T. Yin, and L. K. Kwoh, "2009 earthquakes in Sumatra: The use of L-band interferometry in a SAR-hostile environment," in *2010 IEEE International Geoscience and Remote Sensing Symposium*, pp. 1202–1205, IEEE, 2010.

[106] F. Dell'Acqua and P. Gamba, "Remote sensing and earthquake damage assessment: Experiences, limits, and perspectives," *Proceedings of the IEEE*, vol. 100, no. 10, pp. 2876–2890, 2012.

[107] S.-H. Yun, H. Zebker, P. Segall, A. Hooper, and M. Poland, "Interferogram formation in the presence of complex and large deformation," *Geophysical Research Letters*, vol. 34, no. 12, 2007.

[108] R. Natsuaki, H. Nagai, N. Tomii, and T. Tadono, "Sensitivity and Limitation in Damage Detection for Individual Buildings Using InSAR Coherence—A Case Study in 2016 Kumamoto Earthquakes," *Remote Sensing*, vol. 10, no. 2, p. 245, 2018.

[109] M. Matsuoka and F. Yamazaki, "Use of interferometric satellite SAR for earthquake damage detection," *Sat*, vol. 2, p. z1, 2000.

[110] M. Watanabe, R. B. Thapa, T. Ohsumi, H. Fujiwara, C. Yonezawa, N. Tomii, and S. Suzuki, "Detection of damaged urban areas using interferometric SAR coherence change with PALSAR-2," *Earth, Planets and Space*, vol. 68, no. 1, pp. 1–12, 2016.

[111] A. Akhmadiya and Q. Zeng, "Use of Sentinel-1 Data for Earthquake Damage Assessment in Cases of Amatrice and Sarpol-E Zahab," in *IGARSS 2018-2018 IEEE International Geoscience and Remote Sensing Symposium*, pp. 4877–4880, IEEE, 2018.

[112] S. Karimzadeh and M. Mastuoka, "Building damage assessment using multisensor dual-polarized synthetic aperture radar data for the 2016 M 6.2 Amatrice Earthquake, Italy," *Remote Sensing*, vol. 9, no. 4, p. 330, 2017.

[113] P. Washaya and T. Balz, "SAR coherence change detection of urban areas affected by disasters using sentinel-1 imagery," *ISPRS-International Archives of the Photogrammetry, Remote Sensing and Spatial Information Sciences*, pp. 1857–1861, 2018.

[114] L. Dong and J. Shan, "A comprehensive review of earthquake-induced building damage detection with remote sensing techniques," *ISPRS Journal of Photogrammetry and Remote Sensing*, vol. 84, pp. 85–99, 2013.

[115] "Earthquake of magnitude Mw 6.0 of 24-08-2016." http://cnt.rm.ingv.it/event/7073641, 2016. Accessed: 2019-11-30.

[116] E. Tinti, L. Scognamiglio, A. Michelini, and M. Cocco, "Slip heterogeneity and directivity of the ML 6.0, 2016, Amatrice earthquake estimated with rapid finite-fault inversion," *Geophysical Research Letters*, vol. 43, no. 20, pp. 10–745, 2016.

[117] G. Lavecchia, R. Castaldo, R. De Nardis, V. De Novellis, F. Ferrarini, S. Pepe, F. Brozzetti, G. Solaro, D. Cirillo, M. Bonano, and P. Boncio, "Ground deformation and source geometry of the 24 August 2016 Amatrice earthquake (Central Italy) investigated through analytical and numerical modeling of DInSAR measurements and structural–geological data," *Geophysical Research Letters*, vol. 43, no. 24, pp. 12–389, 2016.

[118] J. Stewart, G. Lanzo, S. Aversa, F. Bozzoni, F. Chiabrando, N. Grasso, V. Di Pietra, S. Dashti, L. Di Sarno, M. Durante, S. Foti, K. Franke, B. Reimschiissel, F. Galadini, E. Falcucci, S. Gori, R. Kayen, G. Mylonakis, E. Katsiveli, A. Pagliaroli, S. Giallini, G. Scasserra, F. Santucci de Magistris, M. Castiglia, S. Sica, A. Simonelli, A. Penna, M. Mucciacciaro, F. Silvestri, A. D'Onofrio, A. Chiaradonna, F. De Silva, P. Tommasi, and P. Zimmaro, "Engineering Reconnaissance Following the 2016 M6. 0 Central Italy Earthquake: Version 1," *Geotechnical Extreme Events Reconnaissance Association Report No. GEER-050A*, 2016.

[119] P. Galli, F. Galadini, and D. Pantosti, "Twenty years of paleoseismology in Italy," *Earth Science Reviews*, vol. 88, no. 1-2, pp. 89–117, 2008.

[120] S. Pucci, P. M. De Martini, R. Nappi, D. Pantosti, R. Civico, T. Ricci, M. Moro, F. Cinti, C. A. Brunori, D. Di Naccio, V. Sapia, R. De Ritis, S. Gori, E. Falcucci, C. Marco, S. Pinzi, F. Villani, G. Gaudiosi, P. Burrato, and M. Lancia, "The 24 August 2016 Amatrice Earthquake: Coseismic Effects. Technical Report," 2016.

[121] J. Stewart, G. Lanzo, E. Ausilio, R. Cairo, F. Bozzoni, M. C. Capatti, F. Pasqua, F. Dezi, L. Di Sarno, M. Durante, A. Simonelli, S. Foti, F. Chiabrando, P. Dabove, V. Di Pietra, P. Maschio, F. Passeri, A. Sgobio, L. Teppati Losè, and P. Zimmaro, "Engineering Reconnaissance Following the October 2016 Central Italy Earthquakes: Version 2," *Geotechnical Extreme Events Reconnaissance Association Report No. GEER-050D*, 2017.

[122] F. Galvis, E. Miranda, P. Heresi, H. Dávalos, and J. R. Silos, "Preliminary statistics of collapsed buildings in Mexico City in the September 19, 2017 Puebla-Morelos earthquake," *Technical report published by the John A. Blume Earthquake Engrg. Ctr., Department of Civil and Environmental Engineering, Stanford University, California*, 2017.

[123] R. Meli and E. Miranda, "The effect of the September 1985 Earthquake on the constructed facilities of Mexico City. Part I: Structural Aspects," *Published by the Engineering Institute of the National University of Mexico (UNAM), Mexico City, Mexico*, 1985.

[124] USGS, "M 7.1 - 1km E of Ayutla, Mexico." https://earthquake.usgs.gov/earthquakes/eventpage/us2000ar20/executiveexecutive/. Accessed: 2019-11-02.

[125] M. Segou and T. Parsons, "Testing Earthquake Links in Mexico From 1978 to the 2017 M = 8.1 Chiapas and M = 7.1 Puebla Shocks," *Geophysical Research Letters*, vol. 45, no. 2, pp. 708–714, 2018.

[126] V. J. Sahakian, D. Melgar, L. Quintanar, L. Ramírez-Guzmán, X. Pérez-Campos, and A. Baltay, "Ground Motions from the 7 and 19 September 2017 Tehuantepec and Puebla-Morelos, Mexico, Earthquakes," *Bulletin of the Seismological Society of America*, vol. 108, pp. 3300–3312, 2018.

[127] J. Mayoral, T. Hutchinson, and K. Franke, "Geotechnical engineering reconnaissance of the 19 September 2017 Mw 7.1 Puebla-Mexico City earthquake: Version 1.0," *Geotechnical Extreme Events Reconnaissance Association Report No. GEER-055A*, 2017.

[128] E. Nissen, A. Ghods, E. Karasözen, J. R. Elliott, W. D. Barnhart, E. A. Bergman, G. P. Hayes, M. Jamal-Reyhani, M. Nemati, F. Tan, and W. Abdulnaby, "The 12 November 2017 M w 7.3 Ezgeleh-Sarpolzahab (Iran) Earthquake and Active Tectonics

of the Lurestan Arc," *Journal of Geophysical Research: Solid Earth*, vol. 124, no. 2, pp. 2124–2152, 2019.

[129] USGS, "M 7.3 - 29km S of Halabjah, Iraq." https://earthquake.usgs.gov/earthquakes/eventpage/us2000bmcg/executive. Accessed: 2019-11-01.

[130] P. Vernant, F. Nilforoushan, D. Hatzfeld, M. Abbassi, C. Vigny, F. Masson, H. Nankali, J. Martinod, A. Ashtiani, R. Bayer, and F. Tavakoli, "Present-day crustal deformation and plate kinematics in the Middle East constrained by GPS measurements in Iran and northern Oman," *Geophysical Journal International*, vol. 157, no. 1, pp. 381–398, 2004.

[131] M. Miyamjima, A. Fallahi, T. Ikemoto, M. Samaei, S. Karimzadeh, H. Setiawan, F. Talebi, and J. Karashi, "Site investigation of the Sarpole-Zahab earthquake, Mw 7.3 in SW Iran of November 12, 2017," *JSCE J. Disaster FactSheets*, 2018.

[132] H. B. Gunce and B. T. San, "Measuring Earthquake-Induced Deformation in the South of Halabjah (Sarpol-e-Zahab) Using Sentinel-1 Data on November 12, 2017," in *Multidisciplinary Digital Publishing Institute Proceedings*, vol. 2, p. 346, 2018.

[133] S. Karimzadeh, M. Matsuoka, M. Miyajima, B. Adriano, A. Fallahi, and J. Karashi, "Sequential SAR coherence method for the monitoring of buildings in Sarpole-Zahab, Iran," *Remote Sensing*, vol. 10, no. 8, p. 1255, 2018.

[134] "Damage Assessment of Koeeke Hasan town and Surroundings, Kermanshah, Iran (UNITAR-UNOSAT)." https://www.unitar.org/maps/map/2736. Accessed: 2019-10-14.

[135] USGS, "M 7.1 - 14km NNW of Anchorage, Alaska." https://earthquake.usgs.gov/earthquakes/eventpage/ak20419010/executive. Accessed: 2019-12-03.

[136] M. E. West, A. Bender, M. Gardine, L. Gardine, K. Gately, P. Haeussler, W. Hassan, F. Meyer, C. Richards, N. Ruppert, and C. Tape, "The 30 November 2018 M w 7.1 Anchorage earthquake," *Seismological Research Letters*, 2019.

[137] K. Franke, R. Koehler, C. Beyzaei, A. Cabas, I. Pierce, A. Stuedlein, , and Z. Yang, "Geotechnical engineering reconnaissance of the 30 November 2018 Mw 7.0 Anchorage,

Alaska Earthquake: Version 1," *Geotechnical Extreme Events Reconnaissance Association Report No. GEER-GEER-059*, 2019.

[138] S. Takeuchi, Y. Suga, C. Yonezawa, and A. Chen, "Detection of urban disaster using InSAR. A case study for the 1999 Great Taiwan Earthquake," in *IGARSS 2000. IEEE 2000 International Geoscience and Remote Sensing Symposium. Taking the Pulse of the Planet: The Role of Remote Sensing in Managing the Environment. Proceedings (Cat. No. 00CH37120)*, vol. 1, pp. 339–341, IEEE, 2000.

[139] Open Topography, "Shuttle Radar Topography Mission (SRTM GL1) Global 30m." http://opentopo.sdsc.edu/raster?opentopoID=OTSRTM.082015.4326.1. Accessed: 2019-12-03.

[140] Japan Aerospace Exploration Agency Earth Observation Research Center, "ALOS World Digital Surface Model "ALOS World 3D-30m (AW3D30)"." https://www.eorc.jaxa.jp/ALOS/en/aw3d30/data/index.htm/. Accessed: 2019-12-03.

[141] European Space Agency, "Copernicus Open Access Hub." https://scihub.copernicus.eu/dhus//home. Accessed: 2019-12-03.

[142] GAMMA Remote Sensing, Gümligen, Switzerland, "GAMMA Software." https://www.gamma-rs.ch/no_cache/software.html. Accessed: 2019-06-12.

[143] G. Santarsiero, L. Chiauzzi, and A. Masi, "Analisi del danneggiamento di edifici situati nella zona Sud del comune di Amatrice: confronto pre e post sisma del 24/08/2016 (V2)," *Photographic report published by ReLUIS, Consorzio Interuniversitario*, 2016. http://www.reluis.it.

[144] A. Masi, L. Chiauzzi, G. Santarsiero, M. Liuzzi, and V. Tramutoli, "Seismic damage recognition based on field survey and remote sensing: general remarks and examples from the 2016 Central Italy earthquake," *Natural Hazards*, vol. 86, no. 1, pp. 193–195, 2017.

[145] G. Fiorentino, A. Forte, E. Pagano, F. Sabetta, C. Baggio, D. Lavorato, C. Nuti, and S. Santini, "Damage patterns in the town of Amatrice after August 24th 2016 Central Italy earthquakes," *Bulletin of Earthquake Engineering*, vol. 16, no. 3, pp. 1399–1423, 2018.

[146] "Mapeo Colaborativo 19s (Datos Necesitan Verificar), Google Maps." https://www.google.com/maps/d/u/0/viewer?mid=1_V97lbdgLFHpx-CtqhLWlJAnYY&ll=19.378689896581427%2C99.15070127080776&z=15}, 2017. Accessed: 2019-10-30.

[147] M. Perry, "python-rasterstats." https://github.com/perrygeo/python-rasterstats, 2013. Accessed: 2019-10-23.

[148] "NOAA Station Data Inventory, Access History." https://www.ncdc.noaa.gov/cdo-web/datasets/GHCND/stations/GHCND:US1AKAB0055/detail, 2018. Accessed: 2020-03-20.

[149] ESA, "RADARSAT satellites: Technical comparison." https://asc-csa.gc.ca/eng/satellites/radarsat/technical-features/radarsat-comparison.asp, 2019. Accessed: 2020-05-04.

[150] ESA, "ICEYE." https://earth.esa.int/web/guest/missions/3rd-party-missions/current-missions/iceye, 2019. Accessed: 2020-05-05.

[151] P. A. Rosen, S. Hensley, K. Wheeler, G. Sadowy, T. Miller, S. Shaffer, R. Muellerschoen, C. Jones, H. Zebker, and S. Madsen, "UAVSAR: A new NASA airborne SAR system for science and technology research," in *2006 IEEE Conference on Radar*, pp. 8–pp, IEEE, 2006.

[152] A. Donnellan, J. Green, A. Ansar, R. Muellerschoen, J. Parker, A. Tanner, Y. Lou, M. Heflin, R. Arrowsmith, J. Rundle, *et al.*, "Geodetic Imaging of Fault Systems from Airborne Platforms: UAVSAR and Structure from Motion," in *IGARSS 2018-2018 IEEE International Geoscience and Remote Sensing Symposium*, pp. 7878–7881, IEEE, 2018.

[153] A. Donnellan, J. Parker, S. Hensley, M. Pierce, J. Wang, and J. Rundle, "UAVSAR observations of triggered slip on the Imperial, Superstition Hills, and East Elmore Ranch Faults associated with the 2010 M 7.2 El Mayor-Cucapah earthquake," *Geochemistry, Geophysics, Geosystems*, vol. 15, no. 3, pp. 815–829, 2014.

[154] B. G. Delbridge, R. Bürgmann, E. Fielding, S. Hensley, and W. H. Schulz, "Three-dimensional surface deformation derived from airborne interferometric UAVSAR: Application to the Slumgullion Landslide," *Journal of geophysical research: solid earth*, vol. 121, no. 5, pp. 3951–3977, 2016.